KAUNAS UNIVERSITY OF TECHNOLOGY

RITA PLAIPAITĖ-NALIVAIKO

FORMATION AND MODIFICATION OF NANOSTRUCTURED COMPOSITE MATERIALS WITH ELECTRON AND PHOTON BEAMS

Doctoral Dissertation
Physical Sciences, Physics (02P)

2015, Kaunas

Scientific Supervisor:

Prof. Dr. Diana ADLIENĖ
(Kaunas University of Technology, Physical Sciences, Physics – 02P)

Language Editor:
Edita Plukienė
UAB "Oltena"

KAUNO TECHNOLOGIJOS UNIVERSITETAS

RITA PLAIPAITĖ-NALIVAIKO

NANOSTRUKTŪRIZUOTŲ KOMPOZICINIŲ MEDŽIAGŲ FORMAVIMAS IR MODIFIKAVIMAS ELEKTRONŲ IR FOTONŲ SPINDULIUOTE

Daktaro disertacija
Fiziniai mokslai, fizika (02P)

2015, Kaunas

Mokslinė vadovė:
Prof. dr. Diana ADLIENĖ
(Kauno technologijos universitetas, Fiziniai mokslai, Fizika – 02P)

Kalbos redaktorė:
Edita Plukienė
UAB "Oltena"

CONTENTS

LIST OF FIGURES

LIST OF TABLES

LIST OF ABBREVIATIONS AND SYMBOLS

a-C:H	Hydrogenated amorphous carbon coating
AFM	Atomic force microscopy
Ag	Silver
Au	Gold
C	Carbon
Co	Cobalt
Cu	Copper
CUBO	Cuboctahedral structure
CVD	Chemical vapor deposition
DC	Direct current mode
DECA	Docahedral structure
DLC	Diamond like carbon
EB	Electron beam
EDX	Energy dispersive X-ray spectroscopy
fcc	Face centered cubic structure
Fe	Iron
FTIR	Fourier transform infrared spectrometry
GLC	Graphite like carbon
H	Hydrogen
hcp	Hexagonal close packed structure
ICO	Icosahedral structure
Ni	Nickel
NPs	Nanoparticles
OM	Optical microscope
PAMAM	Poly(amidoamine)
PC	Pulse current mode
PCS	Photon correlation spectroscopy
Pd	Palladium
PECVD	Plasma enhanced chemical vapor deposition
PLC	Polymer like carbon
PMMA	Poly(methyl methacrylate)
Pt	Platinum
PVP	Polyvinylpyrrolidone
RF	Radio frequency
RS	Raman spectroscopy
R_q	Root-mean-square (rms) average roughness
SEM	Scanning electron microscope
SPR	Surface plasmon resonance
TEM	Transmission electron microscope
UV-VIS-IR	Ultraviolet-visible-infrared spectrometry
VDI	Association of German engineers
W	Tungsten
γ	Gamma radiation

INTRODUCTION

The relevance of the Doctoral Dissertation

Nanostructured materials are materials with a microstructure, the characteristic length scale of which is approximately a few (typically 1–10) nanometers. Nanostructured materials consisting of nanometer-sized crystallites with different crystallographic orientations and/or chemical compositions are far away from thermodynamic equilibrium. Nanostructured materials include atomic clusters, layered (lamellar) films, filamentary structures, and bulk nanostructured materials. Nanostructured materials focus on the synthesis, characterization, and properties relevant to nanostructured materials applications that require bulk and mainly inorganic materials. The properties of nanostructured materials deviate from those of single crystals (or coarse-grained polycrystals) and/or glasses with the same average chemical composition. This deviation results from the reduced size and/or dimensionality of the nanometer-sized crystallites as well as from the numerous interfaces between adjacent crystallites. In some cases, the physics of such nanoscale materials can be very different form the macroscale properties of the same substance, offering often superior properties that warrant much interest in these materials.

In particular carbon coatings attract attention of scientist since it is possible varying deposition conditions and technological parameters to produce different coating structures having unique chemical and physical properties ranging from those of diamond like carbon to graphite like carbon (Robertson, 2002). Special interest is paid to polymer like carbon coatings due to their flexibility to modification. Polymer like coatings might be used as dielectric optical or protective coatings for micro electromechanical (MEM) devices functioning in chemically or radiation harsh environment. Different methods might be applied to create hard carbon structures: varying initial gas mixture content, admixing additives, changing fabrication conditions or technological parameters. Modification and hardening of carbon structures is also possible applying high energy electrons and photons, since such types of irradiation causes structural changes in irradiated structures that in turn are directly linked to the coating's surface morphology changes and influence physical and chemical properties of carbon coatings (Casiraghi et al., 2007; Ferrary and Robertson, 2004). Carbon coatings reveal by unique properties consequently may occur in crystalline and/or amorphous phase, which can be characterized by structures similar to the polymer nanocomposite.

The overwhelming attention towards nanostructured materials containing nanoparticles (NPs) is increasing day-to-day due to their exceptional size-related properties as compared to bulk materials (Jovanovic et al., 2012; Pomogailo et al., 2005). Whatever they are made of, the structure, composition and properties of nanoparticles (Berret et al., 2006; Dallas et al., 2011) are highly important since NPs are applied in electronics, optics, catalysis, biotechnology and medicine (Prabhu et

al., 2012; Chen and Schluesener, 2008). Nano-size metal (Li et al., 2010) particles play a special role among all nanoparticles and are the most examined in nanotechnology. The successful application of nanoparticles depends upon both the synthesis and the surface modification of these particles (Pomogailo et al., 2005; Tee et al., 2007). Surface modification can improve the intrinsic characteristics of nanoparticles and allow the fabrication of nanocomposites and other structures also inexistent in nature (Jovanovic et al., 2012).

Polymer nanocomposites are progressive functional materials (Alsawafta et al., 2011; Tao et al., 2008) composed of nanoparticles dispersed inside of polymer matrix and covered by polymer, thus forming a skeleton structure. Polymer composites are appealing expectants for ionizing radiation armor applications and can be made transparent. In order to capitalize on the superior properties of polymer composites in transparent armor applications, novel techniques and fabrication/modification methods are needed. Modification of polymers with high energy radiation (X-rays, gamma rays, electron beam) leads to the formation of new bonds, free radicals, oxidized products, grafts, scission of main chains and cross-linking (Chmielewski et al., 2007; Liu et al., 2009; Pal Chalal et al., 2012). Radiation induced processes have many advantages over other conventional methods. The importance of the research of radiation hardness of polymers is growing up due to the miniaturization of polymeric constructive elements and broader application of polymeric films characterized by modified surface. Functionality and exploitation characteristics of the devices are dependent on the quality and stability of polymeric materials.

Specific interest is paid to synthesis of heavy metal and alloy nanoparticles exhibiting exceptional structural, magnetic and mechanical properties (Tsyntsaru et al., 2012; Walton, 2002): nanocomposites containing these particles are widely used for fabrication of different hard coatings (Gonzalez-Garcia et al., 2010; Klima, 2011). Also the interest to polymeric Pb free nanocomposites with incorporated heavy metal or metal alloy nanoparticles that might be used for the construction of radiation protection devices is growing up. An alternative simple, fast and cost effective synthesis method of nanoparticles is the sonoelectrochemical deposition (Delphine et al., 2003). The ultrasound affected molecules in electrolyte bath sustain a chemical reaction (Birkin et al., 2005) and due to acoustic cavitation (Gedanken, 2004) participate in formation, growth and collapse of bubbles in the liquid. The main advantage of pulsed ultrasound assisted electrolysis method is that the electrochemically deposited nanoparticle's shape and dimensions can be adjusted by changing the electrolyte composition and pH value, by changing electrolysis temperature, by varying current density and ultrasonic power, by synchronizing the current pulse duration and the operation and relaxation time of ultrasonic pulse (Tsyntsaru et al., 2012, 2013; Saez and Mason, 2009). Continuous ultrasound assisted electrosynthesis is another way to produce nanoparticles and to form nanostructures/nanoclusters. In this way it is possible to get the desired size of

nanoparticles or nanoclusters. The crystallinity of produced nanoparticles depends on technological (experimental) conditions (Karaagac et al., 2013; Subramanian et al., 2002).

The aim of the Doctoral Dissertation

Investigation of electron and photon beam induced formation and modification mechanisms of different nanostructured nanocomposites and assessment of radiation impact on mechanical and optical properties of fabricated composites.

Tasks of the Doctoral Dissertation

1. To explore mechanisms of nanostructure formation in polymer like a-C:H coatings irradiated by high energy photons and electrons, to assess structural changes and to investigate mechanical and optical properties of modified coatings;
2. To investigate the formation processes of Ag nanostructures in different polymeric matrices and applying two-step synthesis approach: photochemical synthesis (UV radiation) and radiolysis (energetic photon radiation) to form an Ag/polymer composites and to examine their optical and mechanical properties;
3. To analyze the electrochemical formation mechanism of W-Co nanoparticles applying sonoelectrochemical method for the formation of metal alloy nanoparticles.

Statements carried out for defence

1. Interaction of high energy photons and electrons with polymer like a-C:H carbon coatings is responsible for hydrogen release from coatings and restructuration of polymeric chains depending on technological conditions and deposition parameters of carbon coatings. Due to irradiation the polymeric structures with embedded sp^2 hybridization graphite clusters are formed.
2. Application of two step Ag nanoparticles synthesis method (photochemical synthesis, employing UV radiation and radiolysis induced by high energy photons and electrons radiation) depending on the applied exposure parameters stable Ag/PVP composite structures with silver particles embedded within the polymer matrix are formed.
3. Application of low dose rate photon irradiation allows the formation of Ag nanoparticles directly in PMMA matrix; however, Ag nanoparticles tend to agglomerate to larger structures.
4. The new W-Co nanoparticles synthesis method applying electrochemical deposition process when aqueous electrolyte influenced by continuous ultrasound was proposed and adapted.

Scientific novelty and practical value

- Modification possibility of polymer like a-C:H carbons' employing high energy photons and electrons is shown and radiation induced formation of strongly cross-linked three-dimensional network with embedded small graphitic clusters is discussed. It is shown that the properties of irradiated carbons depend on technological conditions and deposition parameters. Varying the fluency of photons and electrons, synthesis parameters and irradiation dose it is possible to get coatings that might be used as dielectric optical or protective coatings.
- Synthesis possibility of Ag nanocomposites employing two-step synthesis: UV photochemical synthesis and radiolysis induced by high energy photons and electrons is shown. It is found that high energy photons and electrons enhances production and growth of Ag nanoparticles within polymer matrix and contributes to modification of mechanical and especially optical properties.
- Formation possibility of Ag nanocomposites direct from silver salts admixed to polymer solution using low dose rate photon irradiation is explored. Radiation induces Ag nanoparticles growth and formation of the composite, however the prolong exposure time leads to agglomeration of Ag nanoparticles into larger clusters with induced disorder in the polymeric structure.
- A new method of W-Co nanoparticles synthesis is proposed which is related to formation of W-Me alloy nanoparticles under continuous ultrasound. W-Co nanoparticles incorporated in polymers form the polymeric nanocomposites that might be used for the construction of radiation protection devices due to their high radiation absorption ability.

The object and methodology

To implement the tasks of the work following theoretical and experimental research was performed.

Polymer like a-C:H carbon coatings were synthesized using plasma enhanced vapor deposition (PECVD) method, varying ion beam energy and substrate temperature. Experimental coatings were exposed to gamma irradiation in teletherapy unit with ^{60}Co (1.25 MeV) source or irradiated with high energy electrons in medical linear accelerators Clinac DMX (12 MeV) and Clinac2100C (6 MeV). The radiochemical mechanisms of nanostructure formation in carbon

coatings irradiated by high energy photons and electrons were analyzed. The structural changes were assessed and physical properties of modified coatings were investigated. The assessment of the bonding structure of carbon coatings has been carried out using Fourier-transform infrared spectroscopy (FTIR, Nicolet 5700) and Raman spectroscopy (RS, Ivon Jobin with Nd:YAG laser ($\lambda = 532.3$ nm)); optical properties (absorbance, reflectance, refractive index) have been obtained using ultraviolet-visible spectrometer (USB4000-UV-VIS) and ellipsometer "Gaertner 117" (with He-Ne laser: $\lambda=632.8$ nm); surface morphology has been characterized by atomic force microscope (AFM, NT-206).

Ag derivatives were synthesized applying photochemical synthesis method (UV irradiation), which was followed by film irradiation with high energy photons or electrons, that lead to the formation of Ag/polymer composites. The morphology of the Ag/polymer nanocomposites and bulk composition have been investigated using optical microscope (OM, Optika B-600 MET), scanning electron microscope (SEM, JSM-5610 LV) with attached energy dispersive X-ray analysis (EDX, JED-2201) and atomic force microscope (AFM, NT-206). Bonding structure of experimental Ag/PMMA nanocomposite films has been assessed using Fourier Transform infrared spectrometry (FTIR, Bruker Vertex 70). Optical properties have been obtained using ultraviolet-visible spectroscopy (UV/VIS/NIR, AvaSpec-2048).

Tungsten-cobalt alloy nanoparticles (W-Co NPs) have been synthesized from aqueous electrolyte by sonoelectrochemical method applying pulsed potential mode of current supply and continuous ultrasound irradiation. The morphology of W-Co NPs and their chemical composition have been investigated with a scanning electron microscope (SEM, FEI Quanta 200 FEG) with attached energy dispersive spectroscope (EDS, Bruker XFlash® 4030). Some specific data was extracted from transmission electron microscope (TEM, JEOL JEM 1210) images. The size of synthesized W-Co NPs has been assessed by photon correlation spectroscopy (PCS, Delsa).

Author's contribution

Most of the experimental work was carried out in Kaunas University of Technology: Faculty of Mathematics and Natural Sciences Department of Physics, Faculty of Chemical Technology, and Institute of Materials Science. Experimental coatings were also analyzed exploring analytical equipment of Lithuanian Energy Institute. Belarusian State Technological University, Center of Physical and Chemical Investigations (Minsk, Belorussia) offered possibility to perform analysis of surface morphology and coating structure using SEM and TEM. Irradiation of coatings with electrons and photons was performed at Lithuanian Health Care University.

The author of Doctoral Dissertation has personally performed irradiation of experimental carbon coatings with high energy electrons and photons. She performed (to large extent) characterization of coatings before and after irradiation,

analyzed coatings properties and discussed radiochemical mechanisms responsible for restructuration of coatings due to their irradiation. The author has collaborated closely with a team preparing experimental coatings from Ag containing solutions and personally performed their irradiation, which led to formation of Ag/polymer nanocomposites and their radiation induced modification. The author has also worked close together with a team of chemists synthesizing W-Co alloy nanoparticles contributing with the idea of application of continuous ultrasound for particles formation and investigation of the particles properties and radiation absorbing properties of compounds that were produced using synthesized particles.

Approbation of the research results

The main results of this work were presented in 11 international and 1 national conferences. The research results published in 13 scientific publications: 8 articles were published in the journals belonging to scientific international databases (3 – Indexed in the Thomson Reuters Web of Knowledge database with Impact Factor and 5 without Impact Factor), 4 articles were published in international conference proceedings and 1 article was published in the periodicals of Lithuania.

Structure of the Doctoral Dissertation

The dissertation consists of introduction, literature review, instruments and methods section, results and discussions chapter, conclusions, the list of references (166 entries), and the list of scientific publications on the topic of Doctoral Dissertation.

The total size of dissertation is 143 pages, containing 91 figure and 13 tables.

1. LITERATURE REVIEW

Nanostructured materials contain nanoparticles and other nanoderivatives synthesized directly, embedded into or produced within a host material due to its modification. Polymeric nanocomposites are part of nanostructured materials. An overview of advances in nanoparticles production, their embedding into polymers and radiation induced modification of polymeric composites is provided in this chapter. Also modification of properties of amorphous/polymer like carbon structures due to irradiation is analyzed, since these materials may have a similar structure as polymeric composites.

1.1. Classification of nanostructures

Nanoparticles (NPs) are of great scientific interest as they are essentially a bridge between bulk materials and atomic or molecular structures. NPs exhibit a number of unique and considerably changed physical, chemical and biological properties compared to their macro scaled counterparts: due to their high surface-to-volume ratio.

Nanoparticles are classified by the size and by the number, N, of atoms they consist of. Fig. 1.1 illustrates the main stages of individual atoms transformation into a bulk metal (Pomogailo et al., 2005).

Metal atom	Cluster	Nanoparticle	Colloid	Bulk metal
0.1 nm	1-10 nm	10-100 nm	>102 nm	>>103 nm
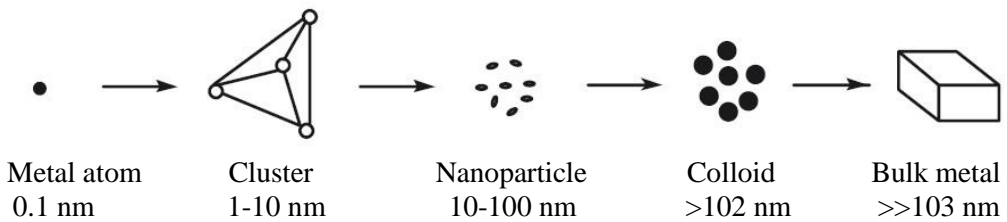
Fig. 1.1 Atom transformations to the bulk material (Pomogailo et al., 2005)

Also classification of nanoobjects according to the number of atoms, N, in the assembly is possible:

- molecular clusters ($N \leq 10$);
- clusters of a solid body ($10^2 \leq N \leq 10^3$);
- microcrystals ($10^3 \leq N \leq 10^4$);
- particles of dense substances ($N > 10^5$).

The structure is one of the most fundamental properties of a cluster and plays an important role to understand all aspects of its chemical and physical behavior. Much experimental and theoretical effort has been devoted to the determination of the cluster structures depending on the size (i.e., the number of atoms in the cluster) N. The structure of nanomaterials can be three- (commonly cross-linked by spatial molecules of various lengths), two- (e.g. self-organized ligand-stabilized particles on the solution surface, often with participation of linking blocks) or one-dimensional

(quantum dots, quantum wires and even quantum cables) as it is shown in the Table 1.1 (Pomogailo et al., 2005).

Table 1.1 Typical nanomaterials (Pomogailo et al., 2005)

	Size (approximate)	Materials
1D nanocrystals and clusters (quantum dots)	1–10 nm in diameter	Metals, semiconductors, magnetic materials, Langmuir–Blodgett films
Other nanoparticles	1–10 nm in diameter	Ceramic oxides
Nanowires	1–10 nm in diameter	Metals, semiconductors, oxides, sulfides, nitrides
Nanotubes	1–10 nm in diameter	Carbon, layered metal, chalcogenides
2D arrays (of nanoparticles)	A few nm^2 to 1 μm^2	Metals, semiconductors, magnetic materials, polymer films
Surfaces and thin films	1–100 nm thick	Various materials
3D structures (superlattices)	A few nm in all three dimensions	Metals, semiconductors, magnetic materials, consolidated material, nanostructured materials
NPs in polymers	1–100 nm	Metal–polymer nanocomposite

Nanoclusters offer attractive possibilities for innovative technological applications in the fields of the controlled growth of nanostructures, from catalysis to miniaturization of electronic devices (Pomogailo et al., 2005).

1.2. Formation of nanostructured materials containing metal / metal oxide / alloy particles

1.2.1. Production of metal nanostructures and their properties

Attention towards nanostructures materials is steadily increasing due to an extensive range of its application in different fields of science (Berret et al., 2006; Dallas et al., 2011; Prabhu et al., 2012). Metal nanoparticles having size of 1-100 nm play an important role in development of new nanomaterials and composites. The reason of the enforcement for nanoparticles in various applications is their fascinating properties (Li et al., 2010; Vodnik et al., 2010). Whatever they are made of, the structure, composition and properties of nanoparticles (Jovanovič et al., 2012; Prabhu et al., 2012; Tee et al., 2007; Vodnik et al., 2010) are highly important since NPs are applied in electronics, optics, catalysis, biotechnology and medicine (Alsawafta et al., 2011; Knauert et al., 2007; Tyurin et al., 2010). The successful application of nanoparticles depends upon both the synthesis and the surface modification of these particles (Chen et al., 2008; Pomogailo et al., 2005). Nanoparticles aggregate easily because of their high surface energy and are quickly oxidized as well (Tyurin et al., 2010).

There are two complementary methods to produce nanostructures: the top-down approach – where one starts with bulk material and machines it down to the nanoscale and the bottom-up approach, starting at the molecular level and building up the material through the small cluster level to a nanoparticle or an assembly of

nanoparticles (Fig. 1.2) (Peng et al., 2009; Tao et al., 2008). Top-down approaches are good for producing structures with long-range order and for making macroscopic connections, while bottom-up approaches are best suited for assembly and establishing short-range order at nanoscale dimensions. The integration of top-down and bottom-up techniques are expected to eventually provide the best combination of tools for nanofabrication (Zahmakiran et al., 2011).
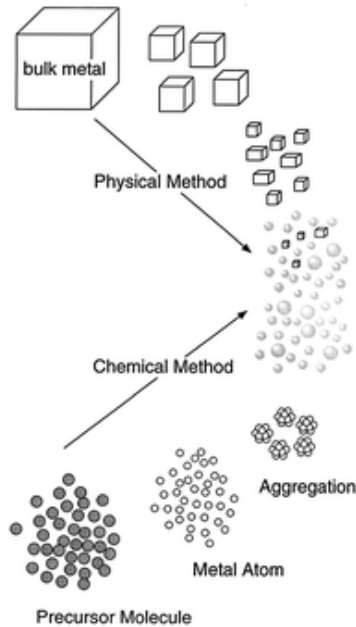
Fig. 1.2 NPs production approaches. Adapted from (Zahmakiran et al., 2011)

Top-down approach. The method sometimes called dispersion or top-down method and these are physical processes. They are based on first-order phase transformations in the absence of chemical reactions during which block metal is atomized to nanoparticles. In the top down methods, the features are written directly onto a substrate, for example, by electron beams, and then by applying appropriate etching and deposition processes, the nanoscopic features are engraved.

Bottom-up approach presents numerous groups of methods (radiation synthesis methods (Liu et al., 2009; Pal Chalal et al., 2012), chemical reduction (Khan et al., 2011; Wang et al., 2005), photoreduction (Krstic et al., 2014; Vodnik et al., 2009), thermal decomposition (Jeevanandam et al., 2010), reduction in micro emulsions (Zielinska-Jurek et al., 2012) and other) that employ chemical approaches to the assembly of nanoparticles from either mononuclear metal ions or nucleus of a lower tendency to nucleation. In the bottom-up approach, nanocomponents are made from precursors in the liquid, solid, or gas phase employing either chemical or physical deposition processes that are integrated into building blocks within the final material structure (Šileikaitė et al., 2009). The difficulty of the nanomaterials
22

synthesis lies in the control of their shape, aggregation or precipitation and stabilization against aging effect (Amendola et al., 2010). To eliminate agglomeration of such particles at storage and transportation, a great variety of stabilizers, including donator ligands, surfactants, and polymers are used (Abu Bakar et al., 2010; Çapan et al., 2009; Chmielewski et al., 2007; Hutter et al., 2001; Slistan-Grijalva et al., 2008). Zielinska et al. (2009) has investigated the influence of different parameters such as, type of silver precursor, reducing agent and protecting agent on stability and optical properties of silver nanoparticles (Amendola et al., 2010; Rao et al., 2011; Tao et al., 2008; Tee et al., 2007; Tyurin et al., 2010; Zahmakiran et al., 2011; Zielinska et al., 2009). Silver nanoparticles prepared using different reducing agents had different morphologies and sizes.

NPs could be synthesized in different form and shapes according to synthesis method and parameters. It was shown (Fig. 1.3) that forming noble-metal particles clusters adopt one of three morphologies: icosahedral (ICO), decahedral (DECA) or close-packed (fcc truncated octahedra) (Häkkinen et al., 2004; Uppenbrink et al., 1992).
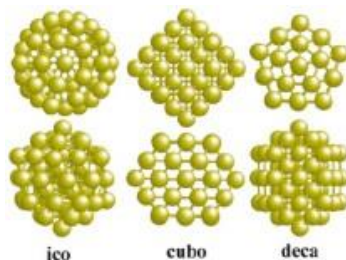
Fig. 1.3 Structures of Ag (on the top) and Au (on the bottom) clusters represented on different structures: closed atomic shell icosahedral (ICO), decahedral (DECA), and cuboctahedral (CUBO). Adapted from (Häkkinen et al., 2004)

Changing the synthesis routes, particles with different shape (spheres and rods (Saraidov et al., 2009), triangulars, cubes, prisms, bipyramids, octahedrons (Tao et al., 2008), nanorods, nanoshells, nanostars (Garsia – Leis et al., 2013) as well as structured array films) and size (from few nanometers to hundreds) in different media (water, alcohols, and polymers) can be formed (Petryayeva et al., 2011). The physical, mechanical, electronic, magnetic, optical and chemical properties of nanoparticles are not necessarily the same as of the bulk material and can all differ (Pomogailo et al., 2005). It is especially evident when analyzing metal nanoparticles.

The formation of nanoparticles proceeds in stages. The main are: nucleation and growth of clusters; rupture of material chains and formation of a new phase (Pomogailo et al., 2005). Despite the difficulty by identifying of stages, the formation of a new phase is a well-explored physical domain. Chain nucleation (stage of formation of active M_1 particles), growth of the new phase particles and generation of transformation products (P, P^*) can be treated from the viewpoint of

kinetics as a chain process (monomolecular or bimolecular) (Hill et al., 2004; Pomogailo et al., 2005):

$$M \xrightarrow{k_0} M_1 + M_j$$

$$M + M_j = M_1 + P^* \tag{1.1}$$

and chain extension (cluster (which consist of j atoms M_j) growth)

$$M_j + M \xrightarrow{k_j} M_{j+1} \ (1 < j < \infty) \tag{1.2}$$
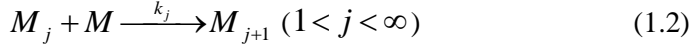
The reactions of dissociation of clusters, take place along with chain nucleation and growth

$$M_j \xrightarrow{k_j^-} M_{j-n} + M_n \ (n \geq 1) \tag{1.3}$$
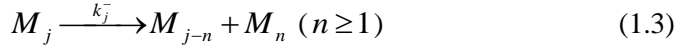
interaction between chain carriers (including coagulation)

$$M_j + M_n \xrightarrow{k_{j,n}} M_{j+n} \ (j,n > 1) \tag{1.4}$$
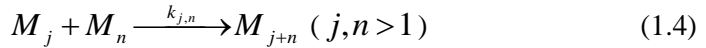
and destruction of the chains as a result of interaction of the growing cluster and stabilizer molecule (or matrix S_*)

$$M_j + S^* \xrightarrow{k_x} M_j S^* \tag{1.5}$$

To describe phase formation, it is necessary to discuss elementary reactions and to solve a lot of differential equations. Quantitative characteristics of reactions during nucleation and growth of metal-containing nanoparticles practically are unknown so far. The basic feature of nanoparticle formation in the kinetic respect is the high rate of metal-containing phase nucleation against to its low growth rate. It serves as a criterion for determining topological means of synthesizing nanoparticles (Pomogailo et al., 2005).

Exceptional optical properties of metal nanoparticles are the consequence of the electromagnetic field interaction with particles which lead to induced collective oscillations of the conduction band electrons within metal particles, known as surface plasmons (Kango et al., 2013; Petryayeva et al., 2011; Prosyčevas et al., 2010; Rao et al., 2011; Šileikaitė et al., 2009). This process is indicated as plasmon excitation and results in appearance of absorption peak (Fig. 1.4).
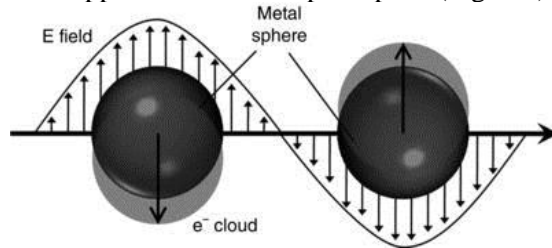
Fig. 1.4 Schematic of plasmon oscillation, showing the displacement of the conduction electron charge cloud relative to the nuclei (Peng et al., 2009)

The width, position, and intensity of the plasmon interaction displayed by nanoparticles (Fig. 1.5) depend on: dielectric functions of the metal and the host

24

material; particle size and shape; interface between the particle and the host; distribution of particles within the host (Uppenbrink et al., 1992). The extinction of light by metal nanoparticles occurs by both scattering and absorption mechanisms, but absorption is by far the dominant factor for nanoparticles of small size (< 20 nm). Increasing the size of the particles, or increasing the dielectric constant of the medium, causes a redshift in the plasmon absorption (Hutter et al., 2004; Petryayeva et al., 2011; Willets et al., 2007).
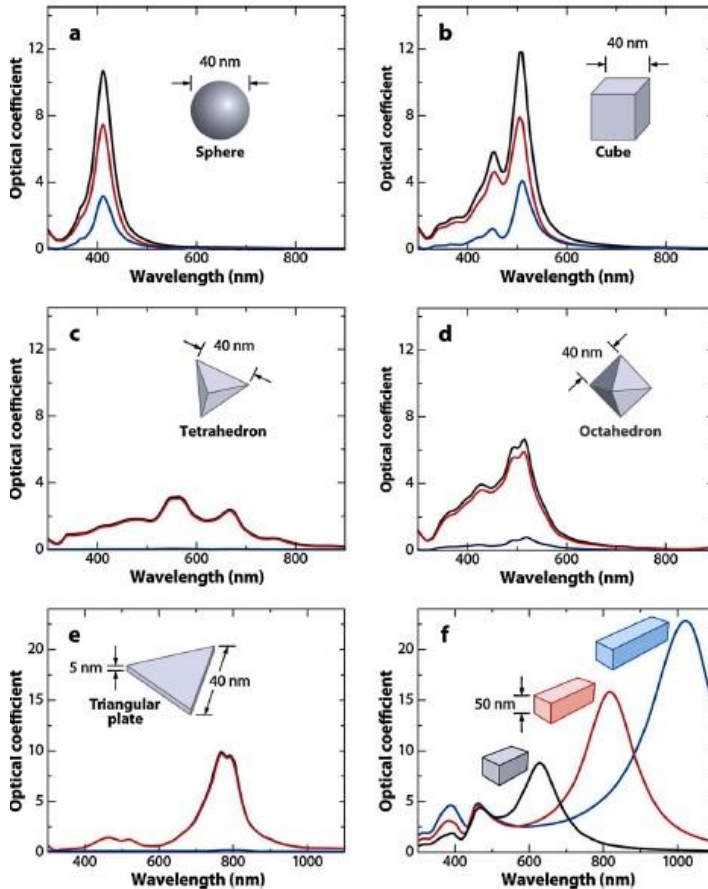
Fig. 1.5 Extinction (black), absorption (red), and scattering (blue) spectra calculated for Ag nanoparticles of different shapes: (a) a sphere displaying a single dipole resonance peak and (b) a cube, (c) a tetrahedron, (d) an octahedron, and (e) a triangular plate. (f) Extinction spectra of rectangular bars with aspect ratios of 2 (black), 3 (red), and 4 (blue). Note that the nonspherical particles typically exhibit multiple, red-shifted resonance peaks. Adapted from (Petryayeva et al., 2011)

For metal nanoparticles, the shift in peak position is minimal for small particles, as well as for larger particles, the redshift of the plasmon resonance

position is more significant (Petryayeva et al., 2011). If the particles are distorted in shape, then the plasmon band splits into different modes corresponding to the different aspects of the electron oscillations. Thus, nonspherical NPs tend to exhibit multiple, redshifted peaks in comparison to spherical particles, as illustrated by Fig. 1.5. Ag exhibits the high efficiency of plasmon excitation (Petryayeva et al., 2011) and interacts with light more efficiently than a particle of the same dimension composed of any known organic or inorganic chromophore (Fan et al., 2014; Manai et al., 2015). The main motivation for using organic coatings around nanoparticles is to tailor their surface chemical properties to particular applications and to protect them from chemically aggressive environments.

1.2.2. Thermodynamics in the synthesis of nanoparticles

According to LaMer (LaMer and Dinegar, 1950) model nucleation is endothermic process. Break of bonds in the initial compound, removal of a solvate shell is energy consuming. At the same time, the processes of NPs growth and agglomeration accompanied by a decrease in enthalpy of the system owing to the bond energy of a lattice are exothermic. Formation of a blocked solid is always energetically beneficial as compared to nanoparticle formation with a typically extensive surface, unsaturated bonds, and no occupied coordination sites (Pomogailo et al., 2014).

In a typical chemical synthesis of metal nanoparticles a compound metal-precursor reduces with formation of zero-valent metal atoms, building blocks of metal nanoparticles (Hwang et al., 2012). During fast reduction concentration of atoms spontaneous homogenous nucleation begins, which is characterized by high-energy barrier (Fig. 1.6). Due to short time of the nucleation, the obtained particles have narrow size distribution. At high supersaturating, an additional mechanism of a decrease in dispersion of particles is possible. The essence of the conception of "explosive nucleation" is in inducing of an individual nucleation process and excluding of additional nucleation from the further growth process. This method as a method of synthetic strategy is often called "separation of nucleation and growth" (Hwang et al., 2012; Lu et al., 2014).
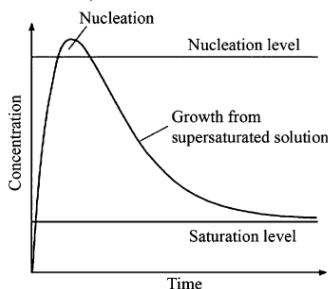
Fig. 1.6 Diagram of the change of precursor concentration under nanoparticle growth (Pomogailo et al., 2014)

To analyze the effect of charge on the coarsening behavior of nanoparticles, it is assumed that each particle is singly charged, electrically-conducting, and spherical with isotropic interface free energy, dispersed in a matrix phase with a dielectric constant of 1. According to this assumption, ions are regarded as the primary rudiments of charged nanoparticles. It is further assumed that the charged nanoparticles do not coagulate with each other and that the atomic transfer between particles is diffusion-controlled. The Gibbs free energy of a spherical conducting particle with radius r and charge e (corresponding to the unit charge of an electron) is expressed as (Hwang et al., 2012):

$$\Delta G = 4\pi r^2 \sigma + k \frac{e^2}{2r}; \tag{1.6}$$

where σ is the interface free energy of the particle and k is defined by $1/(4\pi\varepsilon)$, where ε is the vacuum permittivity (Hwang et al., 2012). ke^2 is $2.3068 \cdot 10^{-28}$ N·m^2. It should be noted that with decreasing r, the interface free energy term decreases but the electrostatic energy term increases.

The modified Gibbs-Thomson equation is derived as:

$$\Delta\mu = \mu_r - \mu_0 = RT \ln \frac{C_r}{C_0} = V_m \left(\frac{2\sigma}{r} - k \frac{q^2}{8\pi r^4} \right); \tag{1.7}$$

where C_o is the solute concentration in the matrix without capillary effect, V_m – molar volume, μ_0 and μ_r are the bulk and surface chemical potentials, r – the particle radius.

According to the theory of diffusion-controlled coarsening (Pomogailo et al., 2014), the growth rate of a particle radius, r, is given by:

$$\frac{dr}{dt} = \frac{D_f V_g C_0}{rRT} [\mu_r * - \mu_r]; \tag{1.8}$$

where R is the gas constant, T the absolute temperature, and D_f is the diffusion coefficient of the solute. μ_r* is the chemical potential of a particle of critical size, which neither grows nor shrinks at the given instant.

Since the phenomenon of digestive ripening runs counter to the decrease of interfacial free energy, a different type of free energy must be involved. The driving force for digestive ripening must compete against the reduction of the interface free energy. There are two such free energies. One is strain energy and the other is electrostatic energy. Since solid particles dispersed in liquid do not have any appreciable strain energy, the electrostatic energy is a possible candidate. In fact, Hwang et al. (2012) states, that if nanoparticles are electrically charged, they have an electrostatic energy inversely proportional to the radius of the particles. Since electrostatic energy increases with decreasing particle size, charged particles cannot shrink away completely. Therefore, the presence of charge can drastically change the Ostwald ripening behavior. The chemical potential change arising from the presence of charge can be treated by modifying the Gibbs-Thomson equation in consideration of the electrostatic energy.
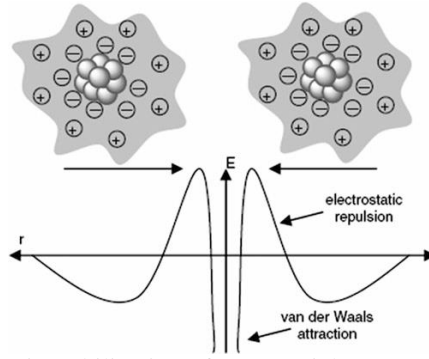
Fig. 1.7 Electrostatic stabilization of nanoparticles (Pomogailo et al., 2014)

The coarsening behavior can be analyzed quantitatively by solving Eq. (1.8) under the constraint of mass conservation for a total number of particles N_p, and is expressed as:

$$\sum_n^{N_p} 4\pi r_n^2 \frac{dr_n}{dt} = 0;$$ (1.9)

Substituting Eq. (1.8) into Eq. (1.9) yields:

$$\sum_n^{N_p} r_n D_f V_m (C^* - C_0 - (C_{r,n} - C_0)) = 0;$$ (1.10)

where C^* is the equilibrium concentration of solute. From Eqs. (1.8), (1.9) and (1.10), the following equation can be derived:

$$\frac{dr_n}{dt} = \frac{D_f V_m^2 C_0}{RTr_n} \left(\sum_n^{N_p} \left(\frac{r_n}{\sum_n^{N_p} r_n} \left(\frac{2\sigma}{r_n} - k\frac{q^2}{8\pi r_n^4} \right) \right) - \left(\frac{2\sigma}{r_n} - k\frac{q^2}{8\pi r_n^4} \right) \right);$$ (1.11)

If the growth rate of each particle is determined by Eq. (1.11), the new radius after dt is given by:

$$r_n(t+dt) = r_n(t) + \left(\frac{dr_n}{dt} \right)dt;$$ (1.12)

Once the initial size distribution of particles is given, the time-dependent size distribution can be obtained by solving equations (1.11) and (1.12) by iteration.

According to the numerical analysis performed by molecular dynamic method, dimers and trimers have higher electron affinity than the initial precursor. It is assumed that reduction will go predominantly by transition of electron from a reducing agent to these dimer and trimer intermediates on the way to clusters and seeds.

At that, association of complexes to a cluster or a respective removal of a ligand from the cluster can significantly accelerate growth of metal nanocrystal.

28

Such acceleration is usually regarded as autocatalytic process which is found in many systems (Fig. 1.8)
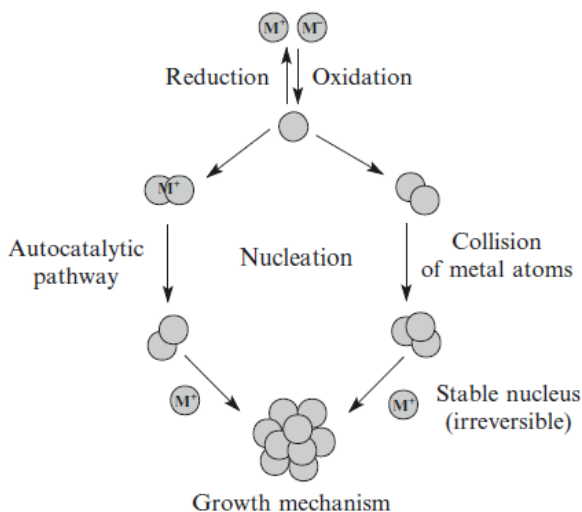
Fig. 1.8 Mechanism of nucleation and growth of nanoparticles (Pomogailo et al., 2014)

As many research teams have shown, Ag clusters demonstrate various optical spectra depending on a number of Ag atoms contained in a cluster.

Atoms of Ag_0 produced during reduction undergo subsequently some transformations with cluster formation (Pomogailo et al., 2014).

$$Ag_2^+ \rightarrow Ag_3^{2+} \rightarrow Ag_4^{2+} \rightarrow Ag_8^{2+} \text{ or}$$

$$Ag^+ + \mathrm{Re}d \leftrightarrow Ag_1 + \mathrm{Re}d^+;$$

$$Ag_1 + Ag^+ \leftrightarrow Ag_2^+;$$

$$Ag_2^+ + \mathrm{Re}d \leftrightarrow Ag_2 + \mathrm{Re}d^+$$

....

$$Ag_n + Ag_m = Ag_{m+n}$$
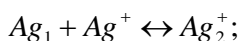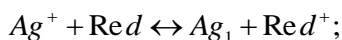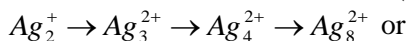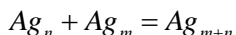
Red is the reduction agent

Particles of Ag_1 and clusters consisting of a small number of atoms are unstable (redox-potential of atomic silver $E^o Ag_1/Ag^+ = -1.8V$ instead of $E^o Ag/Ag^+ = +0.799V$ for metal silver). As metal clusters grow, their stability increases. For example, Ag_8^{2+} cluster is quite stable, it lifetime is measured by 10 min. Optical band corresponding to it in the absorption spectrum differs from the bands typical for Ag (360 nm) and Ag_2^+ (310 nm) dimers and disappears as Ag_8^{2+} cluster transforms in silver sol (Fig. 1.9)
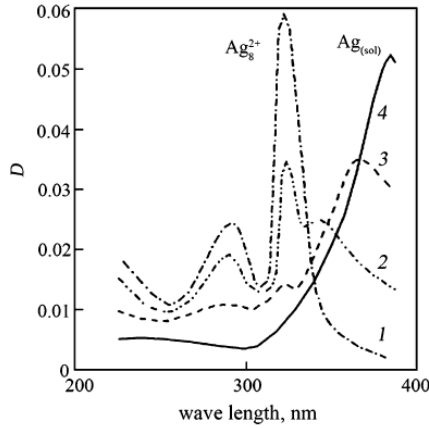
Fig. 1.9 Absorption spectra of the silver salt solution after an electron beam exposure (Ag_8^{2+} cluster transformations in a silver sol). Irradiation duration: 6 s (1), 1 min (2), 5 min (3), 15 min (4) (Pomogailo et al., 2014)

As long as a seed forms, it begins to grow due to adding of atoms. Theoretical consideration of the "diffusion growth" model has shown that growth rate of particles is inverse to their radius, because a number of atoms diffusing to the surface of a particle increases in proportion to its squared radius, and the particle volume increases as cube of its radius. Taking this into account, it is shown that for the ensemble of spherical particles a change in radius distribution σ^2 decreases during the growth (Lu et al., 2014).

If a colloidal particle grows in supersaturated solution, the solute may diffuse from the bulk liquid phase containing a uniform concentration of solute C_b to the particle surface through a diffusion layer with some concentration gradient where C_r is the solubility of the particle. In this condition the growth rate is described by (Hwang et al., 2012):

$$\frac{dr}{dt} = \frac{\frac{D}{r}\left(1+\frac{r}{\delta}\right)V_m\left(C_0 - C_r\right)}{1+\frac{D}{kr}\left(1+\frac{r}{\delta}\right)};\qquad(1.13)$$

where D is the diffusion coefficient of the solute, r is the particle radius, δ is the diffusion radius around a particle and k is the rate constant of the interface reaction of a solute at the particle interface.

If D is much larger than kr ($D \gg kr$), the interface reaction process becomes a rate determining step and Eq is reduced to:

$$\frac{dr}{dt} = kV_m\left(C_0 - C_r\right);\qquad(1.14)$$

In this case of the interface-controlled growth, the growth rate does not depend on the particle size. If D is much smaller than kr ($D << kr$), however, the diffusion process of a solute becomes a rate-determining step and thus:

$$\frac{dr}{dt} = \frac{DV_m}{r}(C_0 - C_r);$$ (1.15)

In this case, of the diffusion-controlled growth, the growth rate is inversely proportional to the radius of each particle. This means that large particles grow more slowly than small ones, which is in contrast with the interface-controlled growth, where the growth rate was the same regardless of the size. Therefore, the diffusion-controlled growth has a stronger tendency to approach the monodisperse distribution than the interface-controlled growth.

The variation of the radius distribution σ^2 during growth changes with time as follows:

$$\frac{d\sigma^2}{dt} = 2V_m D(C_0 - C_r)\left[1 - \bar{r}\overline{\left(\frac{1}{r}\right)}\right];$$ (1.16)

$\bar{r}$ and $\overline{(1/r)}$ are the mean values of r and $1/r$, respectively. C_0 and C_r are concentrations in solution and on the particle surface, respectively.

Standard methods of control over direction of reactions and equilibriums in colloid chemistry are electrostatic and steric stabilization of the particle surface just after nucleation stage (Fig. 1.10).
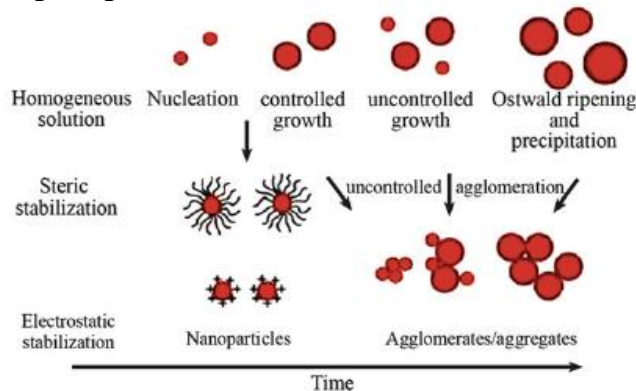
Fig. 1.10 Growth and stabilization of nanoparticles (Pomogailo et al., 2014)

1.2.3. Formation of metal/polymer composites

It should be noticed, that produced particles are not stable and tend to aggregate. To reduce these problems metal NPs are incorporated into polymer matrix forming nanocomposites (Alsawafta et al., 2011; Berret et al., 2006; Dallas et al., 2011; Kango et al., 2013; Knauert et al., 2007; Pomogailo et al., 2005; Prabhu et al., 2012; Puišo et al., 2013; Satyananda et al., 2008; Tyurin et al., 2010; Vodnik et

al., 2013). Nanoparticle-polymer composites are progressive functional materials (Chen et al., 2008; Hill et al., 2004; Vodnik et al., 2013) composed of nanoparticles dispersed inside of polymer matrix and covered by polymer, thus forming a skeleton structure. Addition of nanoparticles or other materials to the polymer matrix enables the modification of polymer properties (improved optical, thermal, mechanical, electrical, magnetic and other properties (Berret et al., 2006; Dallas et al., 2011; Uppenbrink et al., 1992) or sometimes implies addition of new properties to the polymers. With reference to Peng and Yang (2009) and Tao et al. (2008) investigations, the properties of polymer composites depend on type of incorporated nanoparticles, their size and shape, their concentration and interaction with polymer matrix. The main motivation for using organic coatings around nanoparticles is to tailor their surface chemical properties to particular applications and to protect them from chemically aggressive environments.

Nanocomposite materials are defined as one-dimensional, two-dimensional, three-dimensional and amorphous materials, made of distinctly dissimilar components and mixed at the nanometer scale. Five categories cover the majority of composites synthesized with recent techniques being modifications or combinations (Pomogailo et al., 2005):

1. An organic polymer embedded in an inorganic matrix without covalent bonding between the components.
2. An organic polymer embedded in an inorganic matrix with sites of covalent bonding between the components.
3. Co-formed interpenetrating networks of inorganic and organic polymers without covalent bonds between phases.
4. Co-formed interpenetrating networks of inorganic and organic polymers with covalent bonds between phases.
5. Non-shrinking simultaneous polymerization of inorganic and organic polymers.

Nanocomposites can be produced by various methods such as sol gel processing (Saraidov et al., 2009), in-situ polymerization (Vodnik et al., 2009; Vodnik et al., 2010), particle in-situ formation (Singho et al., 2014), blending (Krstic et al., 2014), radiation synthesis (Chmielewski et al., 2007; Jovanovic et al., 2012; Jurasekova et al., 2011; Liu et al., 2009): by generating nanoparticles in a specially prepared polymer matrix, less often by polymerization or polycondensation of corresponding precursors and not much by creation of the materials in a single stage with simultaneous shaping of both nanoparticles and the polymer shell. In fact, these two completely different processes have the same kinetics including nucleation, growth and termination of material chains. In nanocomposites, covalent bonds, ionic bonds, Vander Waals forces, hydrogen bonding could exist between the polymer matrix and filler components (Tee et al., 2007; Vodnik et al., 2013).

Irradiation is one of the important methods for the synthesis of metal clusters under ambient conditions and has important advantages as compared to the chemical

reduction method (Jovanovic et al., 2012; Jurasekova et al., 2011; Zhao et al., 2013). Radiolysis does not require the addition of reducing agents, reducing species are uniformly distributed in the solution; the overall process can be performed at room temperature. Singho et al. (2014) has shown that the successful synthesis of Ag/PMMA nanocomposites depends on reducing PMMA polymerization in the surface of silver nanoparticles. A PMMA forms an active site, which initiates reduced polymerization and gives rise to nanodispersion of Ag/PMMA nanocomposites. PMMA acts a protective agent that restricts the mobility of silver ions during the reaction, and the agglomeration is mostly controlled.

The majority of metal cluster synthesis produced by the irradiation technique have been performed by using γ irradiation in the presence of surfactants or polymers acting as stabilizer of the colloidal suspension (Jovanovic et al., 2012; Petryayeva et al., 2011; Prosycevas et al., 2010; Willets et al., 2007). According to Zhao et al. (2013) the Ag nanoparticles with different morphologies can be produced via γ irradiation process. Increasing the γ ray dose to 36 kGy the one-dimensional Ag nanowires can be produced (Fig. 1.11). The growth process did not stop until all Ag^+ ions are reduced completely. The length and number of one- dimensional structures increased with the elongation of irradiation time.
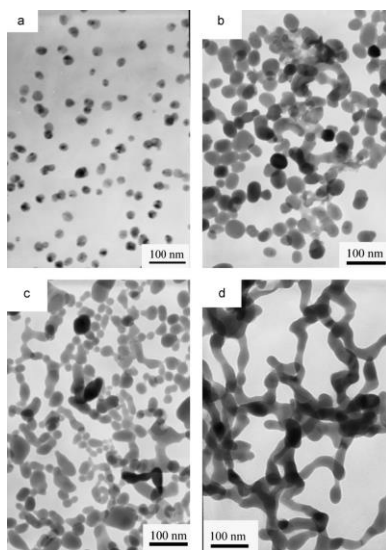
Fig. 1.11 TEM images of the coatings irradiated in the presence of PVP with doses of 12, 16, 24 and 36 kGy, respectively (Zhao et al., 2013)

Prosyčevas et al. (2010) have shown that UV irradiation of Ag and PAMAM solutions lead to photosynthesis of neutral Ag atoms within PAMAM matrix (Fig. 1.12 and Fig. 1.13). Additional irradiation of the mixture to high energy γ photons (^{60}Co source) was responsible for clustering of silver atoms and formation of silver nanoparticles captured in PAMAM network producing Ag-PAMAM composite. The

polymer chains assumed to crosslink upon irradiation and give rise to a three-dimensional network inhibits the aggregation and growth of nanoparticles. It has been shown that γ irradiation had induced changes in optical properties (redshift of the absorbance spectrum after irradiation) of Ag/PAMAM composites. Surface morphology was also changed due to irradiation, but there was almost no influence on the surface roughness parameters of the composite samples observed. (Prosycevas et al., 2007).
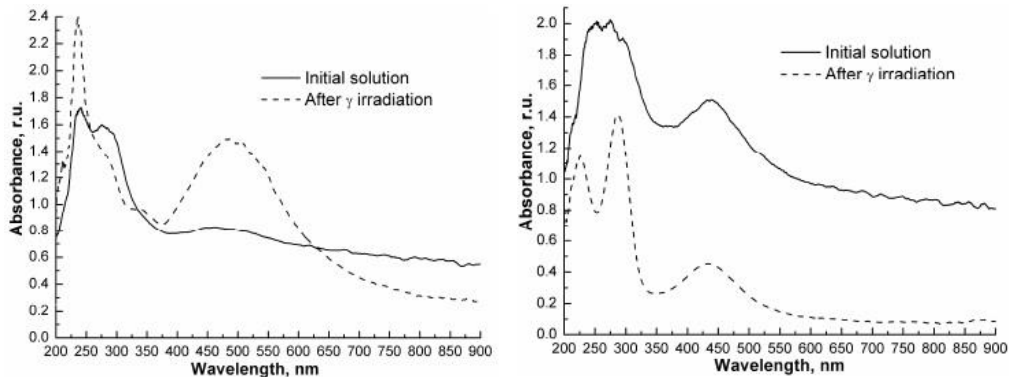
Fig. 1.12 UV-VIS Absorbance spectra of Ag/PAMAM nanocomposites before and after γ irradiation (Prosyčevas et al., 2010)

In contrary, Eisa et al. (2011) has found that increasing dose of γ-rays up to 100 kGy the SPR blueshifts from 422 nm to 412 nm indicating formation of smaller particles (the average size of particles is 30 nm, which decreased to 17 nm with increasing irradiation dose). It is to point out that at higher irradiation doses (up to 100 kGy), γ-rays induce chain scissions in the polymer matrix that causes the polymer chains relax, due to the released stresses. Therefore Ag nanoparticles start to move and are tending to aggregate and agglomerate in larger structures, which in turn reduce the absorption band intensity.

Recently, some papers (Calinescu et al., 2014; Chmielewski et al., 2007; Ibrahim et al., 2009; Jurasekova et al., 2011; Molokovsky et al., 2005; Podsvirov et al., 2010; Prosyčevas et al., 2006; Schardein et al., 2011) have been published on the synthesis of metal clusters including silver nanoparticles (Ag NPs). Such synthesis based on electron irradiation of solutions containing metal ions and polymers (i.e. PVA, PEG, etc.) as stabilizers (Kango et al., 2013; Puiso et al., 2008; Rao et al., 2011). For example, Calinescu et al. (2014) explored the synthesis of Ag NPs using EB irradiation. Two different dose rates of 2 kGy/min and 7-8 kGy/s respectively were applied. According to the results of the performed UV-VIS investigation it was found, that at low dose rates the formation of Ag nanoparticles is prevailing as well as in the case of high dose rate irradiation formation of Ag nanoclusters is prioritary.

Polymers are considered a good host for inorganic nanoparticles. Since the main idea of this part of the overview is to show the applicability of high energy

34

photons and electrons for the formation of nanostructured materials/nanocomposites, behavior of polymers under radiation exposure shall not be overseen.
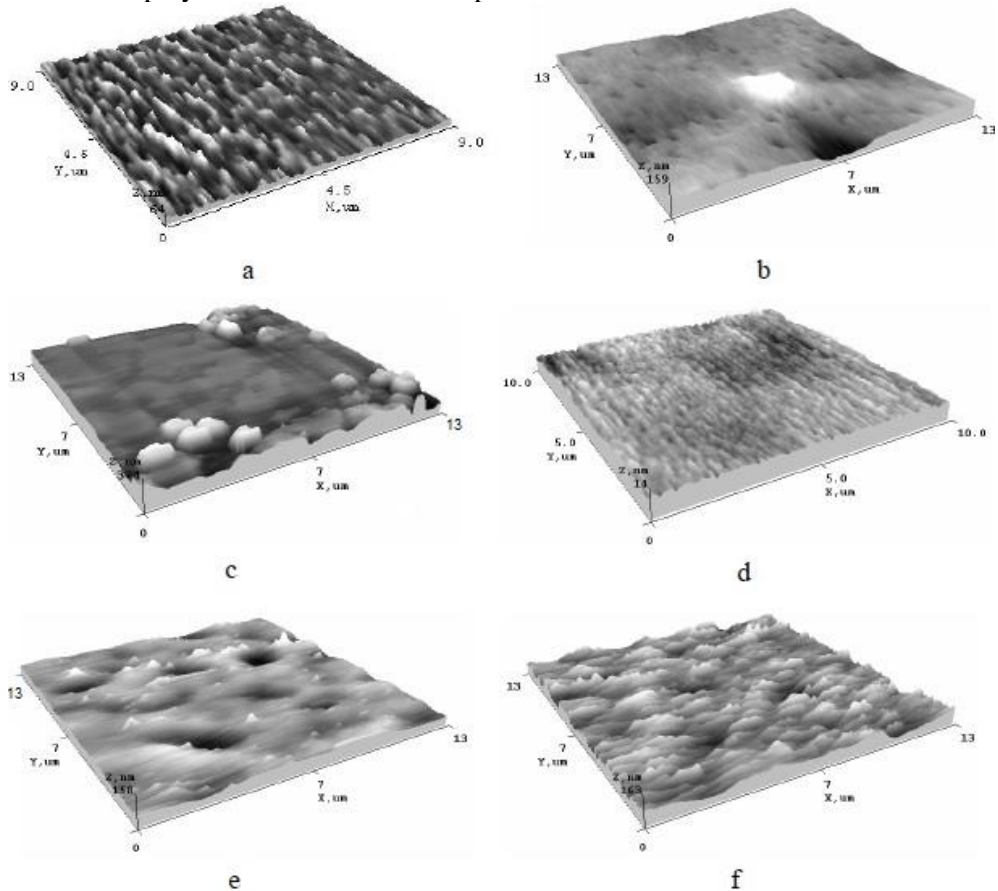
Fig. 1.13 AFM images of polymers and nanocomposites: a – 2.5 % PMMA; b – 2.5 % PMMA{(Ag0)PAMAM}0.1 before γ irradiation; c – 2.5 % PMMA{(Ag0)PAMAM}0.1 after γ irradiation; d – 2.5 % PC; e – 2.5%PC{(Ag0)PAMAM}0.05 before γ irradiation; f – 2.5%PC{(Ag0)PAMAM}0.05 after γ irradiation (Prosyčevas et al., 2010)

Summary. Possible modification of polymers due to their irradiation, if managed, may contribute to the formation of metal-polymer composites characterized by specific structures with distinguished features. Most of the methods applied for the production of metal-polymer nanocomposites are in the development stage. There are still some unsolved problems concerning the stability and aggregation of nanoparticles, control of crystal growth, and morphology, size and particle distribution within polymer matrix. Also some difficulties occur in the management of the synthesis processes as in the case of the radiolysis technique. Surface modification can improve the intrinsic characteristics of nanoparticles and

allow the fabrication of nanocomposites and other nanostructured systems also inexistent in nature (Vodnik et al., 2013; Uppenbrink et al., 1992). This might be achieved combining radiation effects in materials induced by UV exposure, electron, ion, and gamma and X-ray irradiation. However, there is a lack of information about combining the two complementary radiation methods for synthesis of nanomaterials. Application of two consequently following radiation synthesis methods would be of advantage creating nanostructured materials with new appealing properties.

1.2.4. Formation of W-Co nanoparticles

The origin of sonochemical method is the phenomenon of acoustic cavitation. Acoustical energy is mechanical energy - molecules do not absorb it. Ultrasound is transmitted through a medium via pressure waves by inducing vibrational motion of the molecules that alternately compress and stretch the molecular structure of the medium due to a time-varying pressure. Therefore, the distances among the molecules vary as the molecules oscillate around their mean position. If the intensity of ultrasound is increasing, a point is reached at which the intramolecular forces are not able to hold the molecular structure intact (Pacheco et al., 2014). Consequently, it breaks down and a cavity is formed. This cavity is called cavitation bubble as this process is called cavitation and the point where it starts cavitation threshold (Pacheco et al., 2014). A bubble responds to the sound field by expanding and contracting, i.e. it is excited by a time-varying pressure. Two forms of cavitation are known: stable and transient. Stable cavitation means that the bubbles oscillate around their equilibrium position over several refraction/compression cycles. While transient cavitation, the bubbles grow over one (sometimes two or three) acoustic cycles to double their initial size and finally collapse violently. The size, life time and fate of a cavitation bubble depend on frequency, acoustic pressure, solvent, bubble gas, temperature. Continuous ultrasound is responsible for formation of cavitation in the deposit due to explosive collapsing of hydrogen bubbles. Cavitation results in detachment of particles from electrode and their dispersion in the solution.

As it was mentioned above there are a lot of various methods of producing metal nanoparticles including radiation methods (Yen et al., 1999), thermal decomposition (Kim et al., 2006), vapor deposition (Ponce et al., 2005), reduction in micro emulsions (Haram et al., 1996) and chemical reduction methods (Athawale et al., 2005). However most of these methods are relatively expensive and time-consuming. An alternative simple, fast and cost effective method is the sonoelectrochemical deposition. Electrodeposition is a process of electrochemical deposition of solid materials on an electrode surface using electrolysis via electrons transfer from work electrode for metallic ions reduction in solution (Garcia et al., 2013). In practice it is difficult to synthesize tungsten nanoparticles and for this purpose induced co-deposition is used to enhance the reaction rate in electrochemical processes and produce metal nanoparticles with high productivity in spite of its simple operations. Such method used to supersonically agitate the

aggregates nucleated through electrolysis timely off the cathode and to disperse them into electrolyte. Due to the chemical reaction and the effect of electrical current for electrolysis, the main reactions occur in the electrolyte and at the cathode and anode as follows, respectively (Garcia et al., 2013):

$$M_{(aq)}^{n+} + ne^- \to M_{(s)};$$ (1.18)

$$2H_{(aq)}^+ + 2e^- \to H_{2(g)};$$ (1.19)

Due to electrons transfer from work electrode for metallic ions in solution, there is a relation between the current and the overpotential for the electrodeposition, given by Eq. (1.20) (Garcia et al., 2013):

$$i = -FkC \exp\left(\frac{\alpha F \eta}{RT}\right);$$ (1.20)

where F - Faraday's constant, k - constant, C - concentration of metal ions in solution, α corresponds to a coefficient of symmetry (near 0.5), η corresponds to overpotential, R - the ideal gas constant; T - the absolute temperature, in Kelvin.

There is an exponential dependence between the current and applied overpotential. It is clearly seen, that with increasing of overpotential, the ionic current that electrolyte can supply is limited by the other processes as such material transport or electrical conductivity (Garcia et al., 2013). Through Coulomb's law the relation of thickness with the charge density can be obtained by Eq.:

$$d = \frac{Mq}{nF\rho};$$ (1.21)

where M - molecular weight, q - charge density, n - charge of metal ions, ρ - the density.

The sonoelectrochemical effects are explained on the base of different physical mechanisms such as acoustic streaming, microstreaming and turbulence due to cavitation, and formation of microjets in the course of collapse of cavitation bubbles (Klima, 2011).

The main advantage of pulsed ultrasound assisted electrolysis method is that the electrochemically deposited nanoparticle's shape and dimensions can be adjusted by changing the electrolyte composition and pH value, by changing electrolysis temperature, by varying current density and ultrasonic power, by synchronizing the current pulse duration, the operation and relaxation time of ultrasonic pulse (Gedanken, 2004; Saez et al., 2009).

Continuous ultrasound is another way to get the nanoparticles (Fig. 1.14). The formation of nanoparticles, their binding to the nanoclusters run continuously compared with pulsed sonoelectrodeposition. As it mentioned above the growth of nanoparticles up to its maximum size is followed by decomposition into smaller nanoparticles and the reaction is repeated again and again until the ultrasound is switched off. In this way it is possible to get the desired size of nanoparticles or nanoclusters. The products are sometimes nanoamorphous particles, and in other

cases, nanocrystalline depending on technological (experimental) conditions (Gedanken, 2004; Saez et al., 2009; Tsyntsaru et al., 2013).
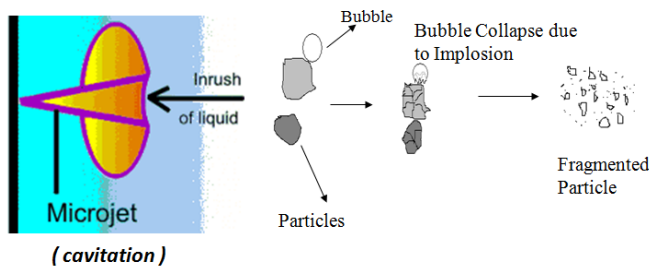
Fig. 1.14 Mechanism of ultrasonic agitation (Birkin et al., 2005)

It is well-known (Delphine et al., 2003; Klima, 2011; Tsyntsaru et al., 2012; Tsyntsaru et al., 2013) that co-deposition method might be applied for the formation of tungsten nanoparticles. However electrodeposition of pure tungsten is requires special technological conditions: it might be deposited from the corresponding salt melts at a high temperature and at large cathode current densities (Abdel Hamid, 2003; Subramanian et al., 2002; Vasauskas et al., 2008). This limits availability of pure tungsten NPs. Nevertheless, in some cases it is possible to replace pure tungsten NPs by tungsten/alloy nanoparticles characterized by their own features however exhibiting some similarities to W nanoparticles. A lot of information could be found about tungsten/metal alloy electrodeposition from the aqueous solutions containing salts of iron group metals (Fe, Co, Ni) (Abdel Hamid, 2003; Gedanken, 2004; Haram et al., 1996; Saez et al., 2009; Subramanian et al., 2002; Tsyntsaru et al., 2012). The essence of these models is that at first reduction of the tungstate (VI) ion to tungsten (IV) oxide and other complex oxygen compounds of various compositions occur. When the nodules of crystallites of iron group metals are formed on the surface of the electrode the tungsten oxide and their complexes easy reduce to metallic tungsten. Thus, electrochemically deposited tungsten form alloys with Fe, Co or Ni (Dontez et al., 2003; Subramanian et al., 2002).

Electrodeposited tungsten-rich alloys of iron group metals are of interest for various applications (Gedanken, 2004; Saez et al., 2009). So electrodeposited tungsten alloys possess a good wear resistance competing with chromium, a mechanical durability (Tsyntsaru et al., 2013), a premium hardness (Vasauskas et al., 2008), a smooth surface (Birkin et al., 2005; Yen et al., 1999), soft magnetic properties (Tsyntsaru et al., 2013), and a reasonable corrosion resistance (Gedanken, 2004; Saez et al., 2009; Tsyntsaru et al., 2013). The structure of the tungsten-based alloys depends on the electrodeposition conditions, and ranges from a crystalline one down to a nano-crystalline one (Gedanken, 2004; Saez et al., 2009). The current efficiency and the composition of the electrodeposited tungsten alloys are strongly affected by the pH of the electrolytes (Gonzalez-Garcia et al., 2010; Klima, 2011; Tsyntsaru et al., 2012; Walton et al., 2002). Due to hydrogen evolution that takes place during the electrodeposition of tungsten alloys, the pH near the electrode

38

increases which can cause nonuniform tungsten content along the thickness of electrodeposited coatings. This effect can be avoided by using electrolytes possessing a sufficient buffer capacity that is achieved by the addition of ammonia or ammonium salts (Dontez et al., 2003; Subramanian et al., 2002), but the presence of ammonia is not critical to achieve high electrodeposition rates of W-Co in contrast to Ni-alloys. Thus, non-volatile citrate electrolytes containing boric acid as a buffering agent for Co alloy electrodeposition are appealing for long-term electrodeposition at higher temperatures. It is known, that electrodeposition can be carried out both in direct (DC) and pulse (PC) current modes. Consequently, tungsten - nickel (W-Ni) and tungsten - cobalt (W-Co) alloys are especially interesting due to their unique combination of tribological, specific magnetic, electrical, mechanical, thermal and corrosion resistance properties (Indyka et al., 2014; Tsyntsaru et al., 2013). These alloys exhibit good mechanical properties (e.g., high tensile strength and premium hardness, as well as superior abrasion resistance), good corrosion resistance in different aqueous media, high melting temperature and anisotropic magnetic properties. To improve the tribological properties and thermal stability of tungsten alloys, it is sometimes eligible to increase tungsten content in the coating. Unfortunately, this is difficult, even when the WO_4^{2-} ion in solution is in large excess compared to the Ni^{2+} ion. It possible to increase the tungsten concentration in the alloy by removing the ammonia (NH_3) from the bath and using citrate $(C_6H_5O_7)^{3-}$ as a ligand, the tungsten content of the alloy may be increased up to 50 at. % (76 wt. %).

Hoshino et al. (2005) as well as Karami and Mohammadzadeh (2010) synthesized cobalt nanowires by constant current electrosynthesis method in cobalt ions solution. The obtained results indicated that pulsed sonochemical method can be used as a reliable and controllable method of producing the cobalt nanorods. Ultrasonication causes the decrease of diameter and increases the lengths of nanorods. Pulse time, relaxation time, pulse height, synthesis temperature, pH, structure additive and ultrasonic irradiation are the most important parameters affecting the morphology, particles sizes and phase compositions of cathode products (Birkin et al., 2005; Hoshino et al., 2005; Indyka et al., 2014; Karami et al., 2010; Tsyntsaru et al., 2013; Walton et al., 2002). The low pulse height is responsible of producing small and uniform nanoparticles due to slow nucleation rate that is lower than particle growth rate as well as the high pulse height causes the producing of big nanoparticles, which are nonuniform and agglomerated. Hence, when the electrosynthesis was performed at temperature ~ 45 °C and lower, the synthesis was slow, due to this the prepared samples were amorphous and agglomerated. At temperatures higher than 45 °C, the synthesis rate is fast, amorphous percent of samples is increased due to high reaction rate, and the nucleation and particle growth processes are not controllable. At 45 °C and lower, pure metallic cobalt can be synthesized. At high temperature (70 ° and more), cobalt will be formed in oxide forms such CoO, Co_2O_3 and CoO_2. Based on the results, the

metallic cobalt content of samples is decreased when the synthesis temperature is increased from 45 °C up to 70 °C and more.

Cobalt tungsten alloys with tungsten content to 30% by weight are ferromagnetic. Abdel Hamid (2003) studied the optimal conditions for cobalt tungsten alloy electrodeposition process, such as temperature, current density, concentration of metal ions or surfactants, the morphology of alloy surfaces, their microhardness and resistance to corrosion. He observed that adding tungsten to cobalt resulted in smoothening of the coating. With tungsten content ranging from 3 to 10% by weight, the alloy had a fine-grained structure, whereas when tungsten content increased to 15% by weight, the structure of the alloy was fibrous with even finer grains. At high current densities, the percentage content of tungsten decreased, whereas increased bath temperature resulted in higher content of tungsten in the alloy. Tsyntsaru et al. (2013) and Vasauskas et al. (2008) studied the mechanical strength and corrosion resistance of cobalt tungsten alloys. They observed that heating the alloys increased their mechanical strength, but decreased their corrosion resistance and tribological properties. The mechanical strength of cobalt tungsten alloys was also studied by Weston et al. (2013). They checked the tear and wear rate of cobalt, chromium and cobalt tungsten alloy coatings according to the loads applied. They concluded that cobalt tungsten alloys demonstrate very good mechanical strength and hardness. They observed a significant influence of the current density, morphology and hardness of the coatings. Moreover, the tribological properties of the coatings were found to be greatly dependent on their grain size, microhardness, surface morphologies and composition. Tsyntsaru et al. (2013) demonstrated that higher tungsten content in cobalt tungsten alloys improved their corrosion resistance.
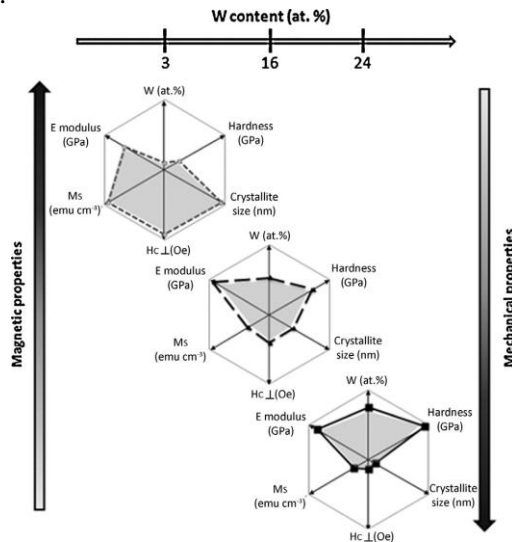
Fig. 1.15 Mapping chart correlating intrinsic and extrinsic properties of Co–W coatings (Tsyntsaru et al., 2013)

40

Tsyntsaru et al. (2012, 2013) obtained nanocrystalline Co–W coatings with 13 – 36 at. % W from citrate–borate electrolyte under DC and PC plating conditions at pH 5, 6.7 and 8. A crystalline structure was obtained when the tungsten content is in the range of 13 to 20.8 at. % W. Investigated coatings presented a mixture of two crystalline phases: W solid solution in hcp Co and a small quantity of Co with fcc structure. When the quantity of W exceeds 21 – 22 at. % the lattice constants of hcp Co gain values characteristic of Co_3W (Fig. 1.15.).

The increased content of tungsten in alloys results in the grain size decrease. The grain size depends rather on the tungsten content than on the electrodeposition conditions (Tsyntsaru et al., 2013).

Summary. A majority of analysis and studies of the W-Co alloy nanoparticles, are due to protect surfaces against mechanical, chemical impact, but the W-Co nanoparticles embedded in a polymer matrix, could create a polymer nanocomposite This is an innovation in this scientific area. There is lack information on similar research. In polymer nanocomposites W-Co nanoparticles could replace the lead, which is toxic and hazardous. W-Co NPs stop ionizing radiation the same as the lead stops (Adliene et al., 2015). Thus, the W-Co polymer composites could be adapted for protection against ionizing radiation.

1.3.   Carbons

When investigating nanostructured materials, special attention shall be paid to carbons that are able to form materials ranging from crystals to amorphous and polymer-like materials in which formation of nanostructures may take place leading to occurrence of nanostructured materials having similar structure as polymer nanocomposites have.

1.3.1.   Classification

Carbon is a fascinating chemical element that exists in more than 90 % of all known chemical materials. The interest for carbon based materials remains high over the years. These materials, especially amorphous ones, having no dominant crystalline lattice structure exhibit outstanding mechanical, optical, electrical and chemical properties (Chu et al., 2006; Godet et al., 1998; Grill, 1999; Lifshitz, 1998; Mahalik et al., 2011; Robertson, 2002) as well as advantageous tribological properties (Santra et al., 2010; Santra et al., 2011). These materials usually compose a blend of graphite and diamond microstructures and thus contain properties of the two. Amorphous carbon films obtained in different forms of matrices and are generally doped with a large amount of hydrogen thus making the materials more different. Generally chemical bonds in amorphous carbon are sp^3, sp^2 and to less extent sp^1 hybridizations (Fig. 1.16).
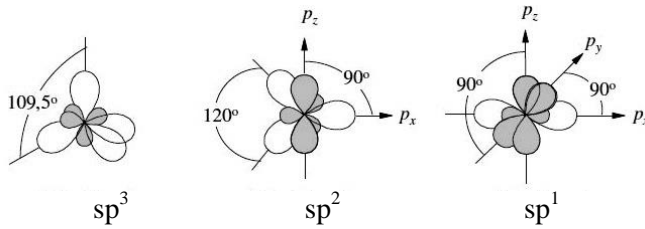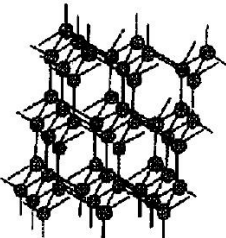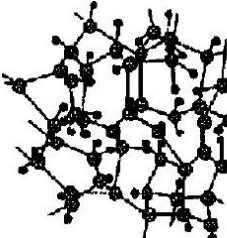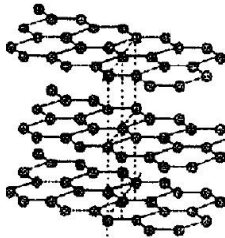
Fig. 1.16 Carbon hybridization forms (Jakubienė, 2009)

The sp^2 hybridized carbon represents a graphite structure where carbon atom has three sp^2 orbitals forming three σ bonds and the remaining p orbital forms a π bond. sp^3 hybridized carbon represents diamond structure where carbon atom has four sp^3 orbitals making a strong σ bond to the neighboring atom. The three σ bonds and π bond usually create a ring plane in sp^2 clusters. Depending on the hybridization, carbon can form structures of various geometries with different fractions of sp^3 and sp^2 bonding in both crystalline and non-crystalline forms. Diamond and graphite are the crystalline forms of carbon (Casari et al., 2008; Fang, 2009; Jakubienė, 2009).

Glassy carbon, DLC, carbon fibers and others are the noncrystalline forms of carbon, which are amorphous containing a mixture of sp^3 and sp^2 bonded carbon and has the properties between diamond and graphite. Amorphous carbon consists of mixture of sp^3 and sp^2 carbon structures interconnected in different ways, having or not sp^2 bonded graphite-like clusters embedded in an amorphous sp^3 bonded carbon matrix (Table 1.2) (Ferrary et al., 2004).

Table 1.2 Comparison of diamond, diamond like carbon and graphite (Casiraghi et al., 2007)

	Diamond	Diamond like carbon	Graphite
Structure	Crystalline (sp^3 bondings)	Amorphous (sp^3 and sp^2 bondings)	Crystalline (sp^2 bondings)
Constitutive element	C	C-H	C
Process	PECVD (nonequilibrium plasma)	PECVD, Ion plating, etc. (nonequilibrium plasma)	CVD (equilibrium plasma)
Reactive gas	C_nH_m and H_2 $CH_4:H_2 = 1:100$	C_nH_m or CVapor CH_4; C_2H_2; C_6H_6 and etc.	C_nH_m
Processing temperature	~700 °C	RT ~300 °C	>1500 °C

Even nanocrystalline graphite and diamond structures can be observed when the sizes of sp^2 and sp^3 clusters become large enough. It should be taken into account that clusters may be produced by fusing double bonds and rings (Buijnsters et al., 2012): due to annealing, irradiation (Godet et al., 1998; Mahalik et al., 2011; Santra et al., 2010) or as as-deposited under a high temperature (Santra et al., 2011; Yadav et al., 2009). Generally, amorphous carbons contain significant quantities of hydrogen. Hydrogen appears to play a very significant role (Ferrary, 2002; Lackner et al., 2009; Robertson, 2002) since it can increase the fraction of C–C sp^3 and C–H bonds.

Raman spectroscopy (RS) is widely used for the characterization of the carbon films (Casiraghi et al., 2007; Ferrary, 2002; Yadav et al., 2009). It has been found that a-C:H films have a broad asymmetrical peak in the 1100 – 1700 cm^{-1} range and it may have two shoulders at 1570 and 1350 cm^{-1} (Fig. 1.17). Both these peaks are due to sp^2 sites. The effect of sp^3 sites is mainly via their influence on the sp^2 configuration. Changes in the G peak position and width are associated with changes of the disorder level in the sp^2-bonded fraction of a-C:H. The D peak position and intensity correlates with the fraction of sp^3-bonded carbon. The D and G peak intensity ratio I_D/I_G is associated with the sp^3/sp^2 bonding ratio and the size of graphite clusters (Ferrary, 2002; Robertson, 2002).
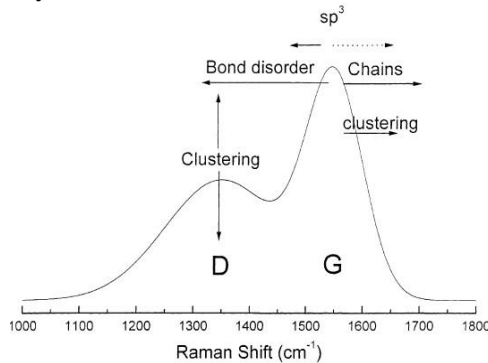
Fig. 1.17 Raman spectra characterization of carbon films (Robertson, 2002)

Depending on the sp^3 content, H content and based on the main binding framework carbon films can be classified as (Casiraghi et al., 2007; Ferrary, 2002; Godet et al., 1998; Grill, 1999; Lifshitz, 1998; Robertson, 2002):
1. a-C:H films with the highest H content (40 – 70 %) called polymer-like a-C:H (PLC). Their band gap ranges from 2 to 4 eV. These films can have up to 70 % sp^3, but, most of the sp^3 bonds are hydrogen terminated and these materials are soft and have low density. These films are usually deposited by plasma-enhanced chemical vapor deposition (PECVD) at low bias voltage.
2. a-C:H films with intermediate H content (20 – 40 %), called diamond-like a-C:H (DLC). Their band gap ranges from 1 to 2 eV. Actually if these films have lower sp^3 content, they form more C–C sp^3 bonds than PLC. Therefore, they

have better mechanical properties. These films are usually deposited by PECVD, or electron cyclotron resonance, or reactive sputtering at moderate bias voltage.

3. a-C:H with low H content (less than 20 %), called graphite-like a-C:H (GLC). Their band gap is under 1 eV. They have a high sp^2 content and sp^2 clustering. These films are usually deposited by PECVD at high bias or by magnetron sputtering.

4. Hydrogenated tetrahedral amorphous carbon films (ta-C:H). ta-C:H films are a class of DLC for which the C–C sp^3 content can be increased while keeping a fixed H content. However, the ta-C:H films with the highest sp^3 content (~ 70 %) and ~ 25 atm. % H content do really fall in a different category. Their optical gap can reach 2.4 eV. These films are deposited by high-density plasma sources such as electron cyclotron wave resonance and plasma beams.

The ternary diagram proposed by Robertson (2002) and Ferrary (2004) illustrates the specific domains of various carbon-based coatings with respect to their sp^2 and sp^3 type bonding characteristic and hydrogen content, but it does not include quantitative aspect of carbon form evaluation that might lead to some confusion identifying a-C:H coatings. To identify which of the carbon forms is on a particular coating, the fraction of hydrogen and the fraction of sp^3 bonded carbon atoms (not graphite) must be measured. Knowing those two numbers enables a user to plot the "location" of the coating on the VDI-map (Fig. 1.18) (VDI, 2012). The closer to the upper left corner that a material plots, the better (and more) pure is the DLC.
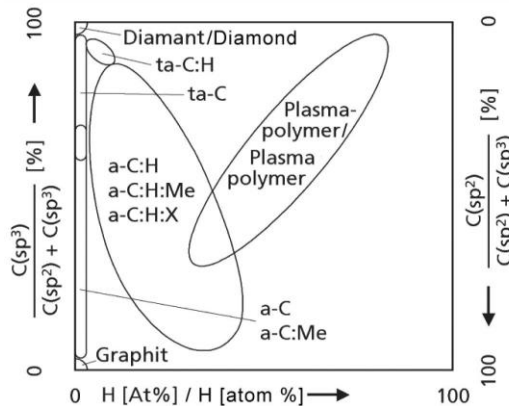
Fig. 1.18 VDI-map of diamond like carbon coatings (VDI, 2012)

According to VDI standard (2012) the bond types have a considerable influence on the material properties of amorphous carbon films. If the sp^2 type is dominant the film will be soft, if the sp^3 type is dominant the film will be hard. The fractional content of hydrogen is a second factor of quality. Some of the production methods involve hydrogen as a catalyst, due to this, the considerable percentage of hydrogen can remain in the finished DLC material. It is notable, that soft plastics are

made from carbon that is bonded purely by the diamond like sp^3 bonds, but also includes chemically bonded hydrogen; it is not surprising to learn that fractions of hydrogen remaining in DLC films degrade them almost as much as do residues of sp^2 bonded carbon (Ferrary, 2004; Robertson, 2002; VDI, 2012).

a-C:H films that have a large H content (40 – 70 %) and low density are called polymer-like a-C:H (PLC) or soft a-C:H and consist of an amorphous matrix with carbon clusters and crystallites in it (Ferrary, 2004; Robertson, 2002; Oliveira et al., 2012; VDI, 2012). The existence of polymeric a-C:H films that are free of nanocrystalline diamond has been also experimentally approved (Buijnsters et al., 2012; Chu et al., 2006; Saito et al., 2000; Yadav et al., 2009). DLC/PLC films provoke huge research interest: they exhibit special optical absorption, intense photoluminescence and electron affinity, are highly flexible to wide range of different modifications due to the high hydrogen content (Chu et al., 2006; Grill, 1999; Lifshitz, 1998). PLC coatings demonstrate features of polymeric micro- and nanostructured materials (Fig. 1.19) and are applicable as dielectric and optical coatings that inhibit corrosion and may protect surfaces of micro electromechanical and electronic devices (MEMS) in harsh chemical environment and to some extent also in radiation harsh environment (Luo et al., 2007).

DLC   PLC
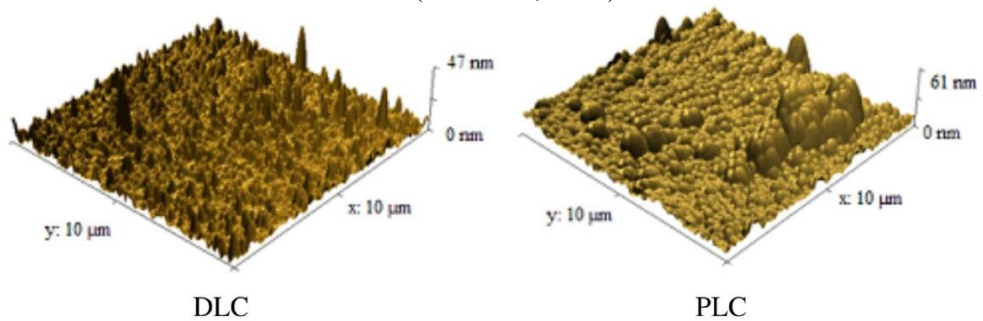
Fig. 1.19 3D AFM images of DLC and PLC films deposited by PECVD on silicon (Oliveira et al., 2012)

Fig. 1.19 shows AFM images of DLC and PLC a-C:H films deposited (PECVD method) on silicon substrate varying deposition parameters. Different surface morphology of coatings was observed: an irregular morphology, including rounded grains with different sizes and nucleation shapes, was present on the surface of the PLC films. DLC films presented rough and more structured surface indicating formation of needle like micro-structures. Thus, the PLC and DLC phases showed different surface morphologies due to variations in the deposition parameters (Oliveira et al., 2012).

According to Robertson (2002) and Saito et al. (2000) the most properties of a PLC films depend on the hydrogen concentrations, formation of sp^2 and sp^3 bonds in the coating, sp^2/sp^3 ratio and the concentrations of C±Hn groups. Their concentrations decrease with decreasing gas ratio due to the etching effect of

hydrogen (Saito et al., 2000). These parameters are controlled when relevant deposition method and process parameters are chosen. A special attention shall be paid to the coating deposition temperature, since it affects structural and some mechanical properties of synthesized coatings (Mahalik et al., 2011; Plaipaite–Nalivaiko et al., 2013; Santra et al., 2011). Mechanical properties of a-C:H films are defined by sp^3 bonds. Hydrogen can affect mechanical properties of the coatings due to the decreased content of sp^3 bonds (Godet et al., 1998; Grill, 1999; Lifshitz, 1998; Robertson, 2002). Electrical and optical properties of PLC films depend upon sp^2 bonds. PLC films are characterized by a wide optical band gap (1.8 – 4 eV) (Ferrary, 2002; Ferrary, 2004; Robertson, 2002), which decreases with growing cluster size or sp^2 distortion.

Various deposition methods (ion beam deposition (Aisenberg et al., 1972; Schwarz et al., 2009), pulsed laser deposition (Eskusson et al., 2009), plasma-enhanced CVD, plasma-assisted CVD (Lackner et al., 2009; Oliveira et al., 2012; Santra et al., 2010), and etc.) are used to produce PLC films from different gas sources: acetylene, methane, benzene and others at low bias voltage. The properties of precipitated coatings depend on the chosen deposition method, initial gas mixture content, admixing additives, fabrication conditions or technological parameters. Among many CVD methods plasma enhanced chemical vapor deposition (PECVD) process is very efficient method to produce homogeneous organic thin films on large area substrates and offers good control over the film properties (Kim et al., 2004). The plasma-enhanced chemical vapor deposition (PECVD) method is the one of few methods, that can produce hydrogenated amorphous carbon (a-C:H) coatings/films from gaseous hydrocarbons. The properties of plasma deposited a-C:H films are strongly affected by kinetic energy of ions bombarding the growing film surface (Novikov et al., 1997). Depending on the chosen pressure and gas mixture at low bias voltage precipitated coatings have a large H and C–H sp^3 content and low density, also C–C sp^2 sites form small clusters that tend to be olefinic.

Due to the unique structure of amorphous carbons it is possible to modify their properties applying different methods (Adlienė et al., 2008; Grigonis et al., 2011; Marcinauskas et al., 2012). Modification of a-C:H coatings with high energy photons, ions and electrons shall be also considered (Adlienė et al., 2008, 2010; Imai et al., 2014). Taking into account that at least highly hydrogenated a-C:H have a structure which is similar to that of polymers, unique properties of irradiated materials can be achieved due to radiation induced polymerization, cross-linking and modification of polymeric structures (Marcinauskas et al., 2012; Plaipaite–Nalivaiko et al., 2013). High irradiation doses (at least of kGy range) are applied for polymer modification in most industrial applications (Makuuchi and Cheng, 2012), however it is also known (Adlienė et al., 2010; Imai et al., 2014) that low dose irradiation induced polymerization is also possible. Possible rearrangement of carbon network upon its interaction with high energy photons and electrons is one of the attractive features of PLC coatings since radiation may induce nanoclusterization within

46

polymeric matrix and lead to the formation of new structures characterized by the new properties (Makuuchi et al., 2012; Šniurevičiūtė et al., 2009).

Imai et al. (2014) has found that the irradiation of PLC films with X-rays lead to the hydrogen desorption and surface etching proportional to irradiation dose. These changes resulted in decreased surface roughness and increased hardness of the irradiated films. Similar results for a-C:H were firstly provided by Adlienė et al. (Adlienė et al., 2008; Adlienė et al., 2010). According to these investigations it was found that the surface of the irradiated films became smoother as compared to not irradiated films (Fig. 1.20). It was also shown that some rearrangements in carbon bonding network due to hydrogen release from material were present that resulted in increased refractive index and hardness. Experimental findings regarding structural changes in films are also supported by the theoretical calculations (Adlienė et al., 2008) that explain formation (due to induced radiation defects) and desorption of hydrogen H_2 from the coating. Recently it was shown that X-ray irradiation is responsible for the increased film density and refractive index (Imai et al., 2014).
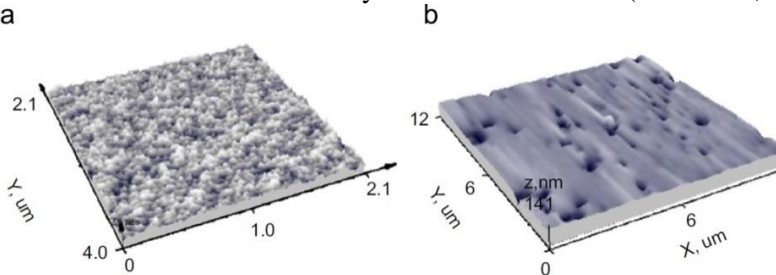
Fig. 1.20 Surface morphology of the a-C:H film: a) before irradiation, b) after high energy X-ray irradiation (Šniurevičiūtė et al., 2009)

Investigation of stress and strain in the amorphous a-C:H was dependent on film deposition time and their structural organization. Additional stress induced by high-energy (12 MeV) electron beam bombardment of DLC coatings was higher in the films with non-uniform structure. Radiation induced changes of the sp^3/sp^2 ratio and hydrogen content are most likely responsible for the changes of the residual stress in irradiated films. Competing stress relaxation processes present after the rearrangements in the film structure due to the irradiation with higher doses could be possible (Šniurevičiūtė et al., 2009).

Novikov et al. (1997) have investigated that bombardment of PLC film with ions may lead to film hardening which might be assessed when analyzing hysteresis loop of irradiated coating (Fig. 1.21). Formation of hysteresis loop is typical for polymers and is caused by their viscoelastic behavior when deformed. It has been found that the mechanical properties of a-C:H films are strongly dependent on the pressure in the reactor. When the pressure decreases the nanohardness and wear resistance increases. Load displacement curves for polymer-like a-C:H film hardened by ion bombardment and without hardening are provided in Fig. 1.25. High elastic recovery of the indent depth after load removal is observed in PLC

films bombarded by ions. The work, carried out on indenter penetration, is spent mainly for elastic deformation of the coating in and around the indent. This curve differs from load displacement curve constructed for initial polymer-like a-C:H film.
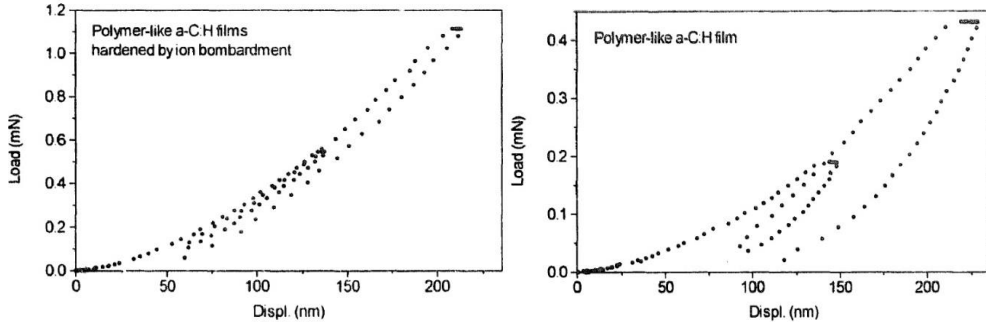
Fig. 1.21 On the left: Load displacement curve for polymer-like a-C:H film hardened by ion bombardment. On the right: Load displacement curve for initial polymer-like a-C:H film (Novikov et al., 1997)

The accelerated electrons bombardment induced grafting and crosslinking of polymeric structure of PLC films (Makuuchi et al., 2012; Novikov et al., 1997). Some recent studies (Casari et al., 2008; Makuuchi et al., 2012; Santra et al., 2011) have disclosed that the application of the multifunctional monomers in irradiation resulting in the shorter irradiation time and the lower dose. Also, the improved physico-mechanical characteristics accelerated ageing resistance and fastness to chemicals and a minimization of macromolecular chain splitting reaction.

Summary. A lot of investigations regarding modification of a-C:H coating properties by high energy photons and especially electrons have been reported, however it is to notice, that the low irradiation dose and low dose rate induced effects in polymer like carbon coatings are still not fully understood and disclosed in details. Taking into account that PLC have polymeric structure and there are graphite (sp^2 phase) clusters present within polymer matrix, it is to expect that upon radiation PLC will obtain a broad spectra of different features that are characteristic to irradiated polymeric composites.

1.4. Radiation interaction with material

1.4.1. Radiation enhanced synthesis processes (radiolysis)

Irradiation is one of the important methods for the synthesis of metal clusters under ambient conditions and has important advantages as compared to the chemical reduction method (Chmielewski et al., 2007). It does not require the addition of reducing agents, reducing species are uniformly distributed in the solution; the overall process can be performed at room temperature.

The radiolysis does not require the addition of reducing agents because the metal reduction is performed by radical species formed after interaction of ionizing

48

radiation with the solvent (Biswal et al., 2013). In fact, the interaction of high-energy radiation with a solution of metal ions induces ionization and excitation of the solvent, and leads to the formation of radiolytic species (Eq. (2.18)). In particular, the solvated electron e_{aq}^-, and hydrogen atom, $^\bullet H$, produced by radiolysis of water, are strong reducing agents capable to reduce metal ions to lower valences and finally to metal atoms (Calinescu et al., 2014; Jovanovič et al., 2012; Liu et al., 2009).

$$H_2O \rightarrow e_{aq}^- + {}^\bullet OH + {}^\bullet H \tag{2.18}$$

Radiation enhanced synthesis processes were analyzed in order to prove the applicability of high energy irradiation and its effectiveness in producing of silver NPs within host substrate (Saion et al., 2013). However before starting this analysis it is necessary to distinguish between physical processes that are present due to electron and photon interaction with materials, taking also into account that the particle penetration depth and energy transfer processes are different (Fig. 1.22, Fig. 1.23).

A   B
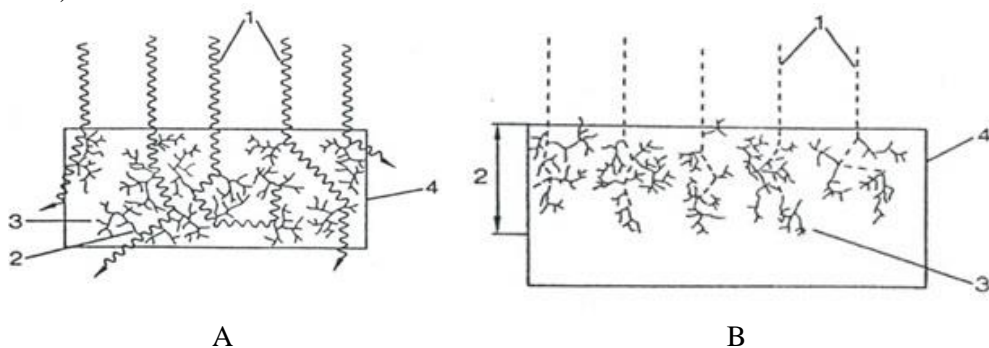
Fig. 1.22 Illustration of different processes induced in material by penetrating ionizing radiation. A - illustration of gamma or X-ray photons induced processes in material; 1-gamma or X-ray photons; 2-Compton electrons; 3-secondary electrons; 4-irradiated medium; B - illustration of electron induced processes in material; 1-electron beam (primary electrons); 2-depth of penetration; 3-secondary electrons; 4-irradiated medium (Drobny, 2012)

A   B
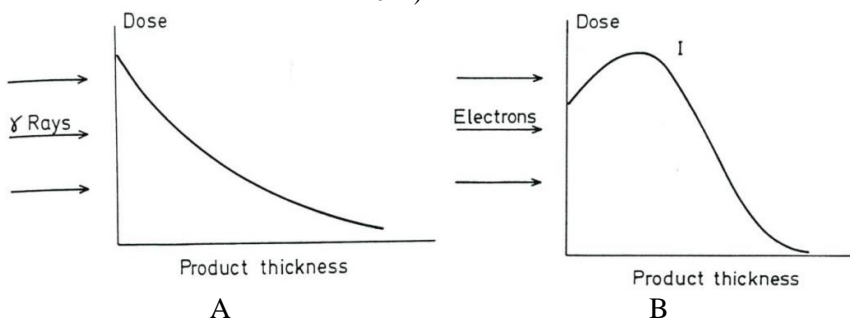
Fig. 1.23 Penetration depth of radiation. A – gamma or X-rays; B – electrons. Adapted from (Drobny, 2012)

1.4.2. High energy electron interaction with material

The electron is ejected and atom is ionized when the energy transferred to the irradiated material is higher than of a particular orbital electron. If the energy is not high enough for ionization, the electron emerges in upper energy level, resulting in excitation. The main parameter describing energy transfer to the target is the stopping or mass stopping power, which might result in production of the secondary (ejected) electrons within limited depth (collision stopping power), or production of the secondary X-ray radiation (radiation stopping power). For light charged particles like electrons are, $S_{col} > S_{rad}$ for the energies < 10 MeV. Ionization might also be responsible for the breaking of chemical bonds in materials that lead to formation of new nanostructures. Generally, the changes in a material depend on the amount of absorbed energy, which in turn, is related to radiation dose and dose rate.
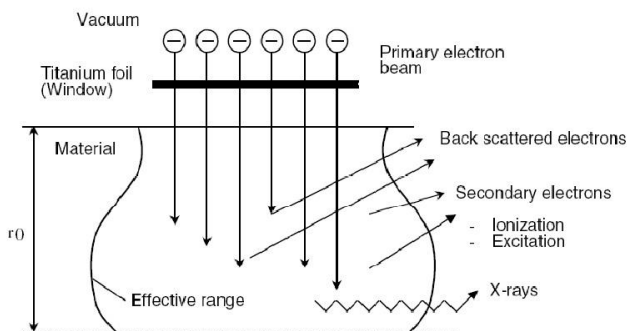
Fig. 1.24 High energy electron interaction with matter (Drobny, 2012)

When the high energy electrons enter the material, they lose their energy as a result of a large number of interactions, each with only a small energy loss (Drobny, 2012; Pomogailo et al., 2005). The interactions with atomic electrons result in production of excited atoms or molecules and ionization. Contrarily, the interactions with atomic nuclei result in production of X-rays (Bremsstrahlung) (Drobny, 2012; Pomogailo et al., 2005). Energy transfer during interaction of high-energy electrons with organic matter (Fig. 1.24) results in:

1. Ionization, which occurs when energy transferred is higher than the bonding energy of the bond electron:
   $AB \rightarrow AB^+ + e^-$;
2. Excitation, when electron from the ground state moves to the excited state:
   $AB \rightarrow AB^\bullet$;
3. Low energy electron capture by atoms or molecules:
   $AB + e^- \rightarrow AB^-$;
4. Dissociation of ionized or excited molecules into free radicals and radical ions:
   $AB^+ \rightarrow A^\bullet + {}^\bullet B^+, AB^\bullet \rightarrow A^\bullet + B^\bullet, AB^- \rightarrow A^\bullet + {}^\bullet B^-$;

50

Newly formed free radicals may initiate polymerization, cross-linking, backbone or side-chain scissions, structural rearrangements in polymers or participate in chemical reactions resulting in change in the properties of materials.

1.4.3. Photon irradiation

Interaction of γ-radiation with matter is of electromagnetic nature so the physical mechanism of such interaction differs from that of charged particles (Kharisov and Kharissova, 2013). Photon interaction processes are of probabilistic origin and depend on photon energy and atomic number of target material. The relative importance of the photon interaction processes are presented in Fig. 1.25.
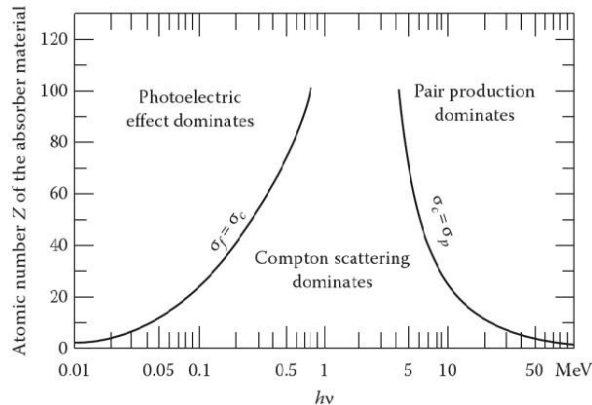
Fig. 1.25 The relative importance of various processes of photon interaction with matter (Kharisov and Kharissova, 2013)

The γ-rays emitted from the decaying atoms (discrete energy) and artificially in X-ray tubes generated X-rays (broad energy spectrum), participate in ionization of irradiated material mainly through secondary electrons.

The main processes of high energy photon interaction with matter are:

- Photoelectric effect, which is based on liberation of bond electron when it absorbs sufficient energy transferred by photon.
- Compton scattering, which is based on partial energy transfer from photon to electron that results in scattered photon of lower energy and recoil electron.
- Electron-positron pair production, which is based on creation of electron and positron pair when high energy photon interacts with nucleus.

The passage of a high energy photon through matter stimulates a complex cascade of processes that result in the dissipation of the primary energy, eventually as thermal energy and chemical reactions. If the energy of photons is relatively low two most important energy loss processes are observed: Compton scattering and photoelectric effect. In the case of Compton scattering photon interacts with an electron resulting in ejection of the electron and deflection of the photon with reduced energy. The probability of Compton scattering event and the consequent

energy of the ejected electron and scattered photon depend on the primary energy of the photon and the electron density of the material. In the case of the photoelectric effect, total energy of the photon is absorbed by a single electron. Whereas the energy of the electron is reduced, there is an increased possibility of recombination of cations and secondary electrons to form excited states. The excited-state molecules may return to the ground state, or endure dissociation reactions to form free radicals, which are supposed to be the main agents in further radiochemical reactions. Heterolytic bond decay may in addition result in the formation of charged species or very reactive intermediates. Suchlike intermediates can follow some reaction paths, which result in rearrangements and/or formation of new bonds. The eventual effects of these reactions can be the formation of oxidized products, grafts, scission of main polymer chains (degradation) or cross-linking. The degree of these transformations depends on the structure of the polymer and the conditions of treatment before the irradiation, during and after irradiation.

Energy lost by photons penetrating target due to photon interactions in irradiated material, results in decrease of photon intensity (Fig. 1.26).
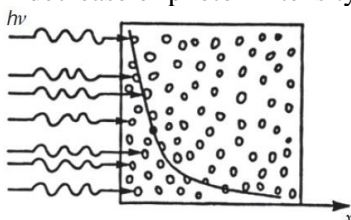
Fig. 1.26 A scheme of photon interaction with matter (Drobny, 2012)

Photon absorption by matter is described by Beer-Lambert law:

$$I = I_0 e^{-\mu x};\qquad(1.22)$$

where I_0 - photon beam intensity at the surface of material, I - photon beam intensity at the certain penetration depth x in material, μ - linear absorption coefficient of material.

The interaction of high-energy radiation with a solution of metal ions induces ionization and excitation of the solvent, and leads to the formation of radiolytic molecular and radical species throughout the solution (Saion et al., 2013). For example, in aqueous solutions (Eq. (1.23))

$$H_2O \rightarrow e_{aq}^-, H_3O^+, H^\bullet, OH^\bullet, H_2, H_2O_2;\qquad(1.23)$$
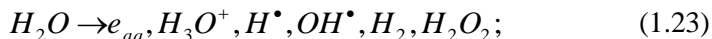
The produced solvated electrons e_{aq}^- and hydrogen atom $H^\bullet$ are strong reducing agents capable to reduce metal ions to lower valences and finally to metal atoms. For instance, from monovalent cations metal atoms are formed according to:

$$M^+ + e_{aq} \rightarrow M^0;\qquad(1.24)$$

$$M^+ + H^\bullet \rightarrow M^0 + H^+;\qquad(1.25)$$

Oxidation by hydroxyl radical $OH^{\bullet}$ is avoided by addition of radical scavengers, such as 2-propanol or polyvinylalcohol which yield after reactions with $OH^{\bullet}$ and $H^{\bullet}$ to a secondary reducing radical $(CH_3)_2C^{\bullet}OH$ (Saion et al., 2013):

$$(CH_3)_2CHOH + OH^{\bullet} \rightarrow (CH_3)_2C^{\bullet}OH + H_2O; \qquad (1.26)$$

$$(CH_3)_2CHOH + H^{\bullet} \rightarrow (CH_3)_2C^{\bullet}OH + H_2; \qquad (1.27)$$
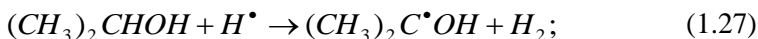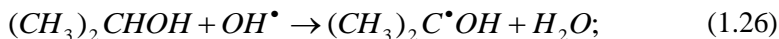
Metal atoms formed in solution by reduction then tend to associate with other ions and coalesce into dimers. These dimers progressively grow into oligomers followed by larger clusters which eventually precipitate. In the case of homonuclear monovalent metal ions, the reactions can be written as follows:

$$M^0 + M^+ \rightarrow M_2^+; \qquad (1.28)$$

$$M^0 + M^0 \rightarrow M_2; \qquad (1.29)$$

$$M_{m+x}^{x+} + M_{n+y}^{y+} \rightarrow M_p^{z+}; \qquad (1.30)$$

To obtain stable clusters, to control NPs shape, possible aggregation or precipitation of NPs and to limit their coalescence, a great variety of stabilizers, including donator ligands, surfactants, and polymers are used.

Taking into account, that the final size of nanocluster (NPs) depends on the type of stabilizing polymer, the polymer/metal ratio, the irradiation dose and the dose rate (Remitta et al., 2005). In order to obtain better insight to the energy deposition and irradiation effects in hosting polymers, three types of ionizing radiation were used: electron beam, gamma and X-rays.

1.4.4. Radiation impact on polymer structures

The effect of ionizing radiation on polymers is that macromolecules change their degree of polymerization and structure. Polymer resistance to natural factors depends not only on the main circuit connection, strength, and any number of alternatives links and chemical composition. Mostly links substituent to reduce the carbon chain macromolecules resistant to physical destruction. Replacing all bound with the main chain atoms of hydrogen, natural resistance factors rises again. In addition, the destruction rate and the product composition depends on the type and intensity of exposure, concentration of the polymer and its environment. Physical destruction of the macromolecular chain is always destruction: first of all active centers formed like free radicals, continues, branching, and completing the radical reactions of kinetic chain.

Radiation destruction of macromolecules might be induced by X-ray, γ-rays, electrons and other particles. Macromolecules operating power can be 9 to 10 eV. It is significantly higher than the binding energy between atoms of macromolecules, which is in range from 2.5 eV to 4 eV. Ionizing radiation energy is sufficient for the irradiation of the polymer from atomic orbitals to dislodge electrons. But it consumes only a small part of absorbed energy. Ionization of macromolecule due to irradiation, results in the appearance of a secondary electron: $M_{n+m} \rightarrow M_{n+m}^+ + e^-$. It

might transfer molecule to the excited-state: $M_{n+m}^{+} + e^{-} \rightarrow M_{n+m}^{\bullet}$. Being excited macromolecule can split into two macro radicals: $M_{n+m}^{\bullet} \rightarrow M_{n}^{\bullet} + M_{m}^{\bullet}$.

Electron interaction processes with neighboring molecules are very fast and take only 10^{-12} seconds. Cross-linking and scission together with grafting and curing are main radiation induced mechanisms in polymers (Fig. 1.27).
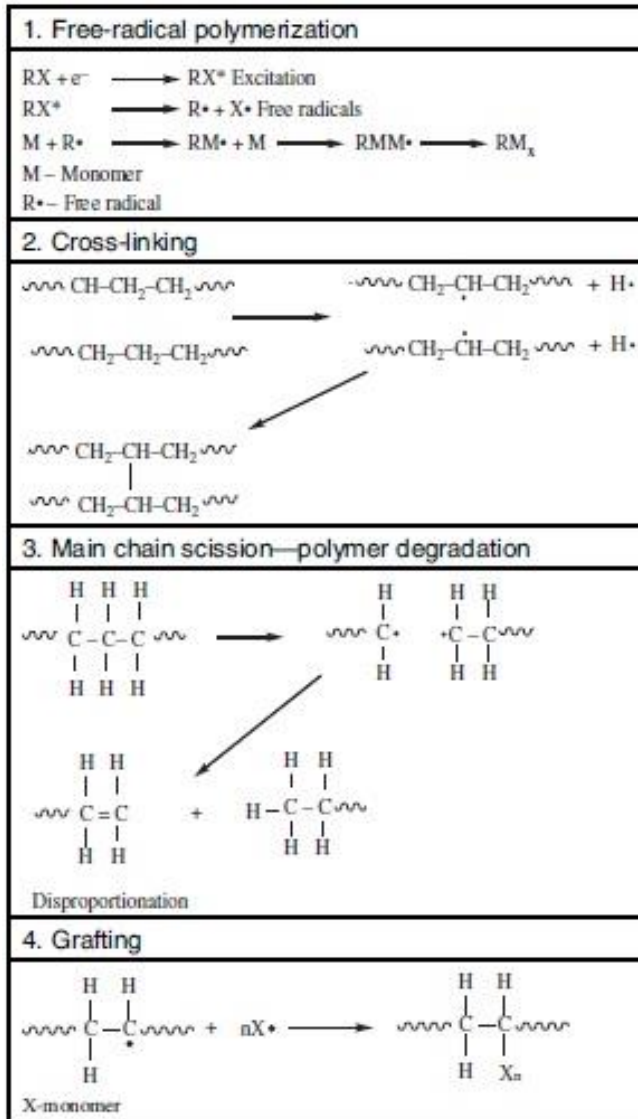
Fig. 1.27 Radiation induced mechanisms in polymer (Drobny, 2012)

Cross-linking is the intermolecular bond formation of polymer chains. The degree of crosslinking is proportional to the radiation dose. The mechanism of crosslinking involves the splitting of a C–H bond on one polymer chain to form a hydrogen atom, followed by occurring of a second hydrogen atom from a neighboring chain to produce molecular hydrogen. Then the two adjacent polymeric radicals combine to form a crosslink (Bhattacharya, 2000). The overall effect of cross-linking is that the molecular mass of the polymer steadily increases with radiation dose, leading to branched chains until the three-dimensional polymer network is formed when each polymer chain is linked to another chain.

Scission is an opposite process of cross-linking in which the break-up of C–C bonds occurs. Cross-linking increases the average molecular weight while the recent process reduces it. Provided the energy of the radiation is high, chain breaking occurs through the splitting of C–C bond. The mechanism of scission process is indirect due to free radicals of polymers. In the presence of oxygen polymeric free radicals form peroxy species and this lead to polymer decomposition into smaller molecules. The oxidative degradation of the polymers depends upon the solvent used in the system and competes with the oxidation of the solvent (Ahmad et al., 2005, Bhattacharya, 2000).

Grafting is a process when monomers are attached laterally to the polymer chain. It should be noted that *curing* is the rapid polymerization of an oligomer monomer mixture to create a coating, which is in fact bonded by physical forces to the substrate (Berret et al., 2006).

There are a lot of similarities between grafting and curing, but though there are specific differences. The grafting process can continue minutes, hours or days, but for curing process it lasts only a second. Covalent C–C bonds are formed in grafting processes as well as in curing, bonding usually relays on weaker van der Waals forces. Van der Waals bonding proceeds at the distances associated with smaller energies. Nevertheless, covalent bonding is effective at small internuclear distances and is associated with higher energies. Curing reactions may occur at the same time as concurrent grafting leading to improved mechanical properties of irradiated species.

Three different techniques might be applied to achieve polymer grafting:
    a) pre-irradiation;
    b) peroxidation;
    c) mutual irradiation.

Applying pre-irradiation technique, the polymer backbone is irradiated simultaneously in vacuum or in gas to form free radicals.

Applying peroxidation grafting method, the trunk polymer is subjected to high-energy radiation in the presence of air or oxygen, which leads to the formation of hydroperoxides or diperoxides depending on the nature of the polymeric backbone and the irradiation conditions. Stable peroxy products are then treated with the monomer at high temperature, from where the peroxides undergo decomposition

to free radicals that initiate grafting. The advantage of this technique is that the intermediate peroxy products can be stored for long period before performing the grafting step (Pandey et al., 2014).

Applying mutual irradiation technique, the polymer and the monomers are irradiated simultaneously to form the free radicals and thus addition takes place. Since the monomers are not exposed to radiation in the preirradiation technique, there are no problems related to homopolymer formation which occurs applying the simultaneous technique. However, applying the pre-irradiation technique the scission of the base polymer due to its direct irradiation is possible. The latter brings forth predominantly the formation of block copolymers rather than graft copolymers.

Polymer resistance to natural factors depends not only on the main circuit connection, strength, and any number of alternatives links and chemical composition. Mostly links substituent to reduce the carbon chain macromolecules resistant to physical destruction. Replacing all bounds with the main chain atoms of hydrogen, natural resistance factors rises again. In addition, the destruction rate and the product composition depends on the type and intensity of exposure, concentration of the polymer and its environment.

Radiation induced modifications depend on the irradiation dose rate and may lead to the deterioration of mechanical and optical properties.

1.4.5. Radiation induced processes in carbons

Depending on the hybridization, carbon can form structures of various geometries with different fractions of sp^3 and sp^2 bonding in both crystalline and non-crystalline forms. In this work attention is paid to amorphous hydrogenated diamond like carbons and polymer like carbons. Structural fragment of polymeric chains containing a C=C bond is provided in Fig. 1.28.
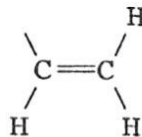
Fig. 1.28 Structural fragment of polymeric chains containing a C=C bond (Novikov et al., 1997)

Hydrogen atoms bonded to the carbon network are believed to play an important role in saturating the carbon dangling bonds and softening the carbon network. A significant loss of hydrogen creates a number of carbon dangling bonds which in turn could bond together under the impact of deposited extra energy, resulting in a structural change.

There are some models describing amorphous carbon structure (Liu et al., 2004; Robertson, 2002). Nevertheless all of the models suggest that carbon may be composed of sp^2-bonded clusters interconnected by a random network of sp^3-bonded

atomic sites. The range of cluster sizes is large, but usually sp^2 islands are limited to single sixfold rings (aromatic) and short chains (olefinic). Even more: three dimensional sp^2 bonding is possible as well as the structure composition with dispersed cross-linked sp^2 sites that provide the network with rigidity (Fang, 2009; Godet et al., 1998; Yadav et al., 2009). Although the sp^3 and sp^2 bonds do not as long distance as they are in crystalline diamond or graphite, sometimes the bonds can admix and present extended order on a nanoscale. The plenty of larger clusters can be produced by fusing double bonds and rings (Ferrary, 2002; Rodil et al., 2001). The rings can be together with each other, or may be deformed in the rigid sp^3 network.

In this work we consider that from C_2H_2 gas produced carbon films consist of sp^2 bonded clusters interconnected in the random network of sp^3 bonded atomic sites. Presence of the large amount of hydrogen in the film is favorable when performing modification of films structure due to high energy electron and photon irradiation: release of hydrogen in any form allows tetrahedral coordinated carbon atoms (sp^3 hybrids) to form strongly cross-linked three-dimensional network in which small graphitic clusters are embedded (Fig. 1.29). This leads to the film hardening and modification of optical and mechanical properties.
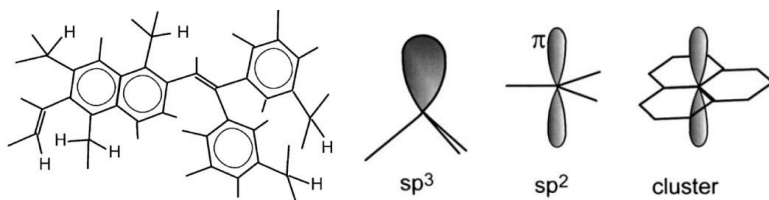
Fig. 1.29 sp^2 clusters and the schema of producing the cluster after the modification with ionizing radiation or ion bombardment (Robertson, 2002)

Penetration of high energy electrons into the film is followed by a cascade of secondary electrons produced in the vicinity of the primary collision event, causing energy deposition on the carbon network in a short time of 10^{-13} s. Therefore, the bonding rearrangement could only occur very locally, and then quench in a very short time if the irradiated ion flux is so small that the interaction among the incident electrons can be neglected. It is known that at the energies < 10 MeV electron stopping is dominant process of energy deposition in the target a-C:H film.

The interaction of the electrons and a-C:H film results in an ionization volume in which the target atoms are excited or ionized so as to break some of the C–H and C–C bonds. The released hydrogen atoms and some small hydrocarbon units could re-combine together to form hydrogen molecules or even methane molecules and diffuse out of the irradiated film. Therefore a number of carbon dangling bonds would be produced. The carbon dangling bonds may rebound, under the influence of the extra deposited energy, to form a more stable carbon network.

2.   INSTRUMENTS AND METHODS

2.1.   Experimental equipment

2.1.1.   Plasma enhanced chemical vapor deposition

Polymer like a-C:H carbon coatings have been synthesized by plasma-enhanced chemical vapor deposition (PECVD) method at room temperature under almost atmospheric pressure from pure (99 %) acetylene (C_2H_2) in RF (13.56 MHz) dual-plasma reactor, which was constructed on the basis of the industrial system YBH-72M-2 (Fig. 2.1.).
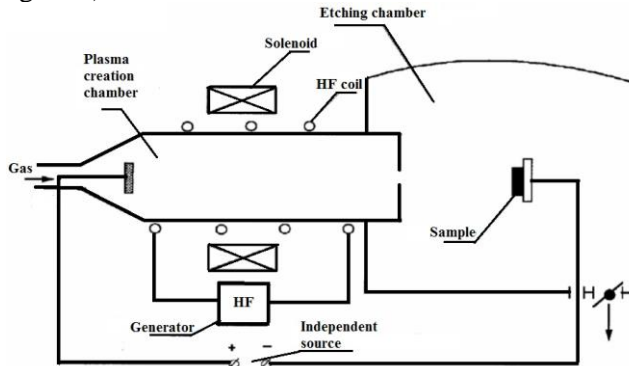
Fig. 2.1 Experimental PECVD set-up. Adapted from (Grigonis and Rutkūnienė, 2007)

Plasma-enhanced chemical vapor deposition (PECVD) is a process in which a gas mixture reacts to form a solid product which is deposited as a coating on the surface of a substrate. The types of coatings that can be obtained by PECVD are varied: insulating, semi conductive, conductive, or super conductive coatings; hydrophilic or hydrophobic coatings, ferroelectric or ferromagnetic layers; coatings resistant to heat, wear, corrosion or scratching; photosensitive layers, etc. PECVD is mainly used for the deposition of high quality thin films; to generate plasma, it uses RF shower head electrode. The plasma is formed in the reaction chamber using an RF generator. The necessary energy for the chemical reaction is not introduced by heating the whole reaction chamber but just by heated gas or plasma. It contains reactive ions and radicals. The growth of the deposit starts easily because of the activation and cleaning of the surface by the more or less intense bombarding with ions from the plasma. The retainer heated resistively or cooled with chilled water circulation. The chamber is evacuated to low pressure turbomolecular pump backed with mechanical pump. Standard equipment comes with one inert gas, three reactive gas lines and four mass flow controllers. The plasma source with its unique gas distribution system makes it possible to meet wide range of requirements such as plasma density, uniformity and separate activation of reactive species to cover the broadest possible deposition parameters as well as good adhesion and high growth

rates. The properties of the coated layers can be better influenced with PECVD than in simply thermal deposition technique, because more process parameters can be varied. Important are the adjustment of adhesion, compressive and tensile stress causing war page, hydrogen content and density, etch ability, etch rate and selectivity in etching, step coverage as well as stoichiometry (consistence) and cleanliness of the deposited layers, which can be evaluated by the refractive index. The PECVD process parameters influence the maximum thickness of the deposit and the best uniformity of the coating. Also some film properties can be modified subsequently.

2.1.2. Centrifuge

The experimental silver/polymer composites were obtained by the spin coating technique using a centrifuge "Dynapert Precima" (Colchester, UK). The coatings were spin-coated on substrates and performed at 60 s rotation speed of 1800 min^{-1}.

The centrifuge "Dynapert Precima" (Fig. 2.2) is a centrifugal separation equipment that the bowl driven by motor and revolve in a high speed, to separate the liquid with smaller density from material or carry out the settling, stratification, and separation. Some mixed liquids are easy to be stratification; some of them can be stratification in quite a long time and not very clear. The centrifuges revolve in high speed, and form powerful centrifugal force. However, the separating speed is fast, according to the different properties of different materials, so that form many centrifuges with different specifications.
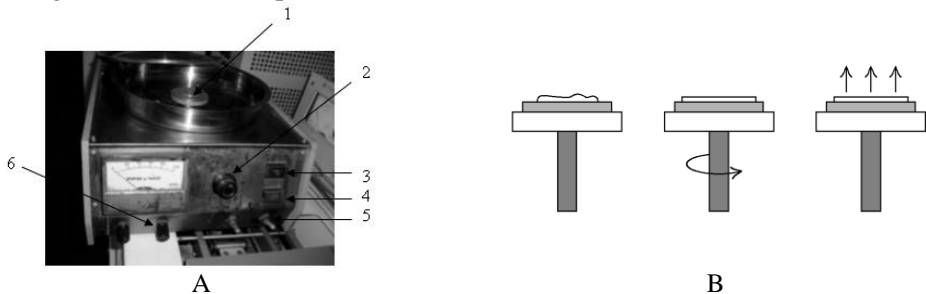
Fig. 2.2 A – "DYNAPERT PRECIMA" centrifuge: 1– sample holder; 2 – time speed control button, 3 – "ON" button; 4 – "OFF" button, 5 – vacuum, 6 – speed monitoring button; B – a schematic view of spin coating technique processing steps

2.1.3. UV irradiation

Synthesis of Ag nanoparticles was performed using photocatalytic reduction of silver atoms directly in a thin layer of deposited polymer. UV light source Hibridas Exposure Unit MA4 (power 1200 W, wavelength 300 – 400 nm) was used for this purpose. Applied UV exposure time of 5 min. was enough for photoreduction of Ag ions and formation of silver nanoparticles.

2.1.4. Continuous ultrasound NPs synthesis

Method of continuous ultrasound assisted sonoelectrochemical synthesis used for the production of W-Co NPs is based on application of pulsed potential mode to working electrode under continuous impact of ultrasound waves on electrolyte. Electrochemical synthesis of W-Co NPs was performed in 100 cm^3 volume beaker which was filled up to the half with the corresponding electrolyte. Beaker was placed into ultrasound bath (cleaner) Sono Swiss SW3H (ultrasonic frequency 38 kHz, effective ultrasonic power 80 W) keeping the same level of the electrolyte and of water in the ultrasound bath (Fig. 2.3).
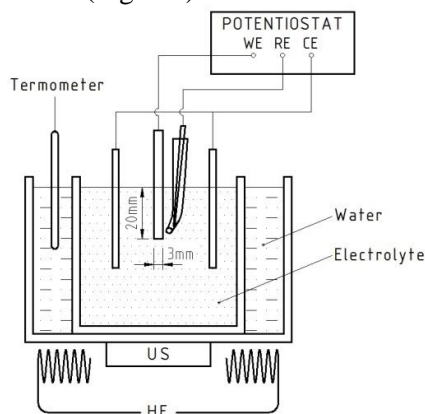
Fig. 2.3 Experimental set-up: HE – heating coil; US – piezoelectric ultrasonic transducer; WE – working electrode; RE – saturated Ag/AgCl reference electrode; CE – counter (auxiliary) electrode; electrolyte containing tungstate(VI) and cobalt(II) ions

The electrolyte was heated up to the 60 °C and this temperature was kept throughout the entire electrosynthesis procedure which was performed under continuous ultrasound impact. The mode of pulsed potential was maintained using potentiostat-galvanostat SP-150 (France, BioLogic) interfaced with EC-Lab (v10.23) software. The working electrode (cathode) was 0.5 mm thick titanium alloy Ti90-Al6-V4 plate with dimensions of 3 x 100 mm. It was dipped about 20 mm in electrolyte during synthesis process thus working area of this electrode was approximately 140 mm^2. It should be emphasized that the main reason to choose Ti alloy for working electrode (cathode) was a poor adhesion of electrodeposits on this alloy.

Two square-shaped platinum plates with dimensions of 10 x 10 mm each were symmetrically arranged on both sides of the working electrode as auxiliary electrodes (parallel connected two anodes). Before the experiment surface of Ti alloy working electrode was polished with Nr. 600 emery paper, washed with distilled water and degreased with isopropanol. The potential control of the working electrode (cathode) was carried out using saturated Ag/AgCl electrode for reference. During the experiment working electrode was pulse polarized from steady-state
60

potential of approx. -0.16 V to -1.5 V (vs. Ag/AgCl). The impulse duration was t_{imp} = 500 ms. Electrochemical system relaxed between the pulses at open circuit conditions for t_{occ} = 800 ms. The sonoelectrochemical synthesis in pulsed potential mode lasted for 1h.

Synthesized W-Co NPs were transferred from the aqueous electrolyte to the in water insoluble trichloromethane (chloroform, $CHCl_3$) solvent protecting them from corrosion. Transfer of W-Co NPs was performed by centrifugation of mixture containing equal volumes of trichloromethane and electrolyte. This was possible due to the fact that the density of $CHCl_3$ (d = 1.483 g/cm^3) is higher than the density of water. Centrifugation was carried out for 30 minutes in laboratory centrifuge CL-1 at the speed $\geq$ 3500 rpm.

2.1.5. Irradiation equipment

Ionizing radiation used to modify physical, chemical and biological properties of the materials. The main applications of radiation are materials modification like as polymerization, polymer cross-linking, and nanoclusterization.

Gamma ray irradiation equipment. Gamma rays were generated in ROKUS-M irradiation facility with ^{60}Co isotope as the gamma radiation source (Fig. 2.4).
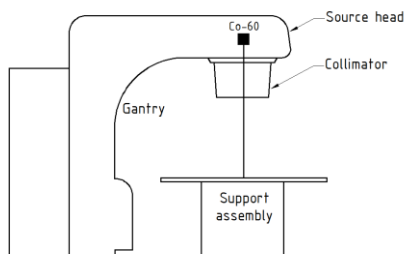
Fig. 2.4 ROKUS-M schematical view
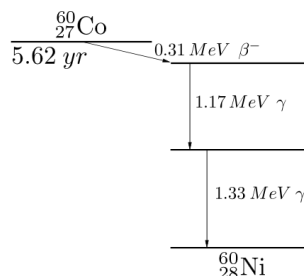
Fig. 2.5 Decay scheme of Co-60

^{60}Cobalt (Fig. 2.5) is a synthetic radioactive isotope with a half-life $T_{1/2}$ = 5.27 yrs. It emits beta and gamma rays. The beta decay energy is low (E = 0.31 MeV) and easily shielded, but the gamma-ray emission lines have energies E_1 = 1.17 MeV and E_2 = 1.33 MeV and are highly penetrating.

Polymer like a-C:H coatings were irradiated with medical teletherapy unit ROKUS-M. Gamma photons were emitted from ^{60}Co source. Varying the bias voltage the activity of ^{60}Co source was 6.52 · 10^{13} Bq with the dose rate of 6.5 mGy/s. Varying the temperature the activity of ^{60}Co source was 4.28 · 10^{13} Bq with dose rate of 2.8 mGy/min. The maximum distance between the source and irradiation surface (SSD) was 75 cm and the irradiation field was 10*10 cm^2. Total irradiation dose varied in the range 2 – 50 Gy.

X-ray irradiation equipment. Experimental films were irradiated to different doses at dose rate of 3.5 mGy/min using 35 keV and 30 mA X-ray photons

generated in X-ray diffractometer DRON-3 (Fig. 2.6). The diffractometer was equipped with a single crystal graphite flat monochromator for transmitting a narrow Cu K_α wavelength ($\lambda = 0.15405$ nm). Irradiation of coatings was performed with the aim to investigate low dose X-ray radiation induced modification of their optical properties, caused by polymer degradation and formation of metal nanoparticles within polymer matrix.

Fig. 2.6 X- ray diffractometer DRON 3.0

Fig. 2.7 Clinac 2100

Electron beam irradiation equipment. High energy (up to 12 MeV) electrons have been generated in medical linear accelerator Clinac DMX and Clinac 2100C (VARIAN) (Fig. 2.7): the energy of electrons was 12 MeV and 6 MeV respectively. The dose rate was 2 Gy/min and 3 Gy/min respectively as well as the maximal irradiation dose was 2 and 3 Gy respectively.

The electrons are generated in a high vacuum. The electrons emitted from the cathode are accelerated in an electrostatic field applied between cathode and anode. The acceleration takes place from the cathode that is on a negative high voltage potential to the grounded vessel as anode. The accelerated electrons might to be focused by an optical system to the window plane of the accelerator (Adliene et al., 2009). The energy gain of the electrons is proportional to the accelerating voltage and is expressed in electron volts (eV), which represent the energy gained by a particle of unit charge by passing the potential difference of 1 V. The electrons leave the vacuum chamber only if their energy is high enough to penetrate the $15 - 20$ μm thick titanium window of the accelerator. When an EB enters a material the energy of the accelerated electrons is significantly changed.

2.2. Analytical methods

Characterization of nanoparticles and polymer like carbon coatings is important to understand and control their synthesis and applications. Characterization is performed using a variety of different techniques such as transmission, scanning electron and optical microscopy (TEM, SEM, OM), atomic force microscopy (AFM), Fourier transform infrared spectroscopy (FTIR), Raman

spectroscopy (RS), photon correlation spectroscopy (PCS), and UV–VIS spectrometry (UV–VIS).

These techniques are used for determination of different parameters such as particle size, shape, pore size and surface area. Moreover, orientation, intercalation and dispersion of nanoparticles in nanocomposite materials could be determined by these techniques. For instance, TEM, SEM and AFM could determine the morphology and particle size. The advantage of AFM over traditional microscopes such as SEM and TEM is that AFM measures three-dimensional images so that particle height and volume can be calculated. Furthermore, dynamic light scattering is used for determination of particles size distribution. Moreover, UV–VIS spectrometry is used to confirm film formation by showing the plasmon resonance.

2.2.1. Ultraviolet-visible spectrometry

Optical spectra of polymer like a-C:H coatings were characterized using the USB4000–UV–VIS spectrometer. The USB4000–UV–VIS Spectrometer was pre-configured with order-sorting filter to cover the 200 – 850 nm wavelength range. Light Source: integrated deuterium tungsten halogen light source and pixel resolution: 0.2 nm; Logger Pro 3 (version 3.6 or newer) software is required

Optical absorbance spectra (carrying information about plasmonic properties of material) of the silver/polymer nanocomposite films were measured using UV-VIS Avantes UV/VIS/NIR AvaSpec–2048 spectrometer in the wavelength range 190 – 1100 nm. The AvaSpec–2048 Fiber Optic Spectrometer (Fig. 2.8) is based on the AvaBench–75 symmetrical Czerny-Turner (Fig. 2.9) design with 2048 pixel CCD Detector Array. The spectrometer has a fiber optic entrance connector, collimating and focusing mirror and diffractional grating. A choice of 15 different gratings with different dispersion and blaze angles enable applications in the 200 – 1100 nm range. The AvaSpec–2048 is especially suitable for low light level and high resolution applications. An optional detector coating enhances the CCD performance for the UV range and a detector collection lens offers high sensitivity. Resolution is 1.4 nm.

Fig. 2.8 AvaSpec 2048 UV–VIS spectrometer
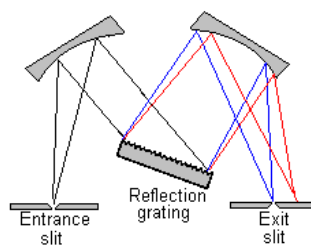
Fig. 2.9 Czerny-Turner grating monochromator

The UV–VIS spectrometer is a portable ultraviolet light and visible light spectrophotometer. UV–VIS spectrometry records the change of intensity of light upon interaction with matter to the initial incident intensity. The analysis is based on Beer–Lambert Law, and gives information about the chemical composition of the material, thickness and absorption coefficient. It is used for the determination of main optical characteristics of different materials that might be evaluated from absorption spectrum taking into account transmittance and reflectance of the light passing through the experimental films. The absorption spectrum reflects the transitions of electrons from a ground state to an excited state in the molecular orbitals that are appropriate in the wavelength range of investigation. The electronic transitions observed in the UV–VIS spectroscopy generally appear as broad peaks because of the interactions of polymer molecules with each other and the solvent molecules.

The size of synthesized nanoparticles plays also an important role in the setting of the absorption spectrum in UV–VIS range, since metal nanoparticles have very specific absorption peaks in the visible region, so called surface plasmon resonance (SPR) band.

Absorption coefficient with reference to optical transmittance and reflectance measurements may be calculated according to:

$$\alpha = \left(\frac{1}{d}\right)\ln\left[\frac{T}{(100-R)^2}\right]; \tag{2.1}$$

where T – Optical transmittance; R – reflectance and d – film thickness.

Due to that the refraction was not measured, the absorption coefficient was estimated with reference to measured UV-VIS transmittance spectra, according to Beer-Lambert law:

$$\alpha = \left(\frac{2.303}{d}\right)\log\left(\frac{1}{T}\right); \tag{2.2}$$

where T – Optical transmittance; d – film thickness.

As mentioned above, nanoparticles of noble metals like silver and gold have very specific absorption peaks in the visible region called surface plasmon resonance (SPR) band, which make those nanoparticles important in optical applications (Dadosh, 2009; Ponelyte and Palevicius, 2014). SPR band originates from the quantum size effect of the nanoparticles, since nanoparticles have neither atomic nor metallic electronic properties, because of their confined energy levels. Their electronic properties strongly depend on the particle size, interparticle distance, and nature of the protecting shell and the shape of the nanoparticles (Amendola et al., 2010). The quantum size effect is seen when the de Broglie wavelength of the valence electrons is of the same order as the size of the particle itself. When this happens, particles behave electronically as zero-dimensional quantum dots. Freely mobile electrons get trapped in such metal boxes and show a characteristic collective

64

oscillation frequency of the plasma resonance, which is called surface plasmon resonance band (Hutter and Fendler, 2004).

2.2.2. Fourier transform infrared spectroscopy

The bonding configuration of polymer like a-C:H coatings was studied by means of infrared spectroscopy. Reflectance and transmittance spectra of coatings were measured in the range of 650 – 4000 cm^{-1} and in the range of 400 – 4000 cm^{-1} respectively using Fourier-transform infrared spectrometer Nicolet 5700. Silicon wafer and air gap were taken for the reference.

Bonding structure of experimental Ag/PMMA nanocomposite films was investigated using Fourier Transform infrared spectrometer Bruker Vertex 70, in the wavenumber range from 400 cm^{-1} to 4000 cm^{-1}, with a resolution of 0.5 cm^{-1}.

Spectroscopy is the study of matter and its interaction with electromagnetic radiation. All matter contains molecules; these molecules have bonds that are continually vibrating and moving around. These bonds can vibrate with stretch motions or bend motions. FTIR is a versatile experimental technique for identifying the functional groups. The IR region of the spectrum composes of radiation with wave numbers ranging from about 12500 cm^{-1} to 50 cm^{-1} wavelength. IR region lies between visible and microwave region. The IR region constitutes 3 parts:
1. the near IR (0,8 μm – 2,5 μm or 12500 cm^{-1} – 4000 cm^{-1});
2. the middle IR (2,5 μm – 15 μm or 4000 cm^{-1} – 667 cm^{-1});
3. the far IR (15 μm – 200 μm or 667 cm^{-1} – 50 cm^{-1}).

The most of the analytical applications are confined to the middle IR region because absorption of organic molecules is high in this region. It gives sufficient information about the structure of a compound. FTIR can be used to obtain important information about everything from delicate biological films to tough materials. The most significant advance in IR spectroscopy is well-established mathematical process of Fourier-transformation. FTIR has improved the quality of IR spectra and minimized the time required to obtain data (Chu et al., 2006). IR absorption arises from vibrational modes with a dipole moment. It is widely used in a-C:H to determine the C–H bonding configurations also provides precise information about orientation of specific functional groups within the polymer film.

It should be noted that IR spectroscopy is useful in determining chemical structure because energy that corresponds to specific values allows identifying various functional groups within a molecule. An IR spectrum usually extends from radiation around 4000 cm^{-1} to 500 cm^{-1} and can be split into the functional group region and the fingerprint region. The functional region can be further split into 3 regions: the first region from 4000 cm^{-1} to 2500 cm^{-1} corresponds to single bonds to H, e.g. O–H, C–H; the second region from 2500 cm^{-1} to 2000 cm^{-1} corresponds to triple bonds, e.g. C≡C; the third region from 2000 cm^{-1} to 1500 cm^{-1} corresponds to double bonds, e.g. C=C, C=O; and fingerprint region from 1500 cm^{-1} to 500 cm^{-1} corresponds to single bonds, e.g. C–O, C–C.

A FTIR spectrometer (Fig. 2.10) simultaneously collects spectral data in a wide spectral range. The term Fourier transform infrared spectroscopy originates from the fact that a Fourier transform (a mathematical process) is required to convert the raw data into the actual spectrum. A radiation from the source falls on the interferometer. It comprises of beam splitter, moving mirror, fixed mirror. The beam splitter splits the light into two half beams of equal intensities. One half of the beam is passed to the fixed mirror. Other half is directed towards the mirror. It moves at short distance away the beam splitter at constant speed. Light enters the spectrometer and is split by the beam splitter. The figure above shows what is referred to as the Michelson interferometer. Speed of the moving mirror is controlled by using a helium-neon laser beam. Because of the steady movement, detector receives constants signals of maxima and minima. Beams after undergoes reflection from the respective mirrors are recombined and send signal to the detector. Combined signal is called as interferogram. After that, the interferogram is both transmitted and reflected to the coating cell. Coatings absorb only those IR frequencies that cause vibration within the coating molecules. The signal is transmitted to the detector where it gets measured. The coded signal has been decoded by using computer. FT spectroscopy can be employed for a long range of frequencies varying over ultraviolet, visible, near infrared, mid infrared and far infrared regions by selecting different beam splitters and detectors for the required ranges. No other dispersive technique can be used for such a wide range of frequencies (Rodil et al., 2001).
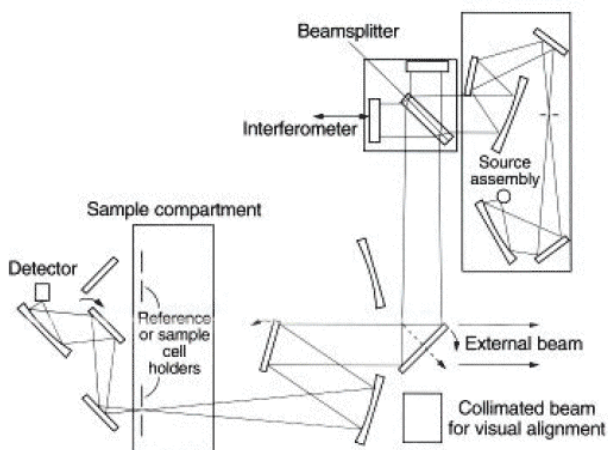
Fig. 2.10 Fourier transform infrared spectrometer

$$I(\delta) = \int\limits_{0}^{+\infty} B(v)\cos(2\pi v\delta)dv \ ; \qquad (2.3)$$

$$B(v) = \int\limits_{-\infty}^{+\infty} I(\delta)\cos(2\pi v\delta)d\delta \; ; \qquad\qquad (2.4)$$

2.2.3. Ellipsometry

Coating thickness and refractive index was estimated using null ellipsometry (ellipsometer Gaertner 117 with He-Ne laser: λ = 632.8 nm). The angle of incidence of the light is 30 °, 50 °, 70 °. Laser ellipsometry is based on the analysis of parameters of polarization of monochromatic polarized light beam reflected from the coating. Thickness of films possible for analysis is 0.001 – 1 μm. Uncertainty of thickness measurements is ± (0.5 – 1) nm. The accuracy of the refractive index measurements is ± 0.01. A schematic view of the ellipsometer components is presented in Fig. 2.11.
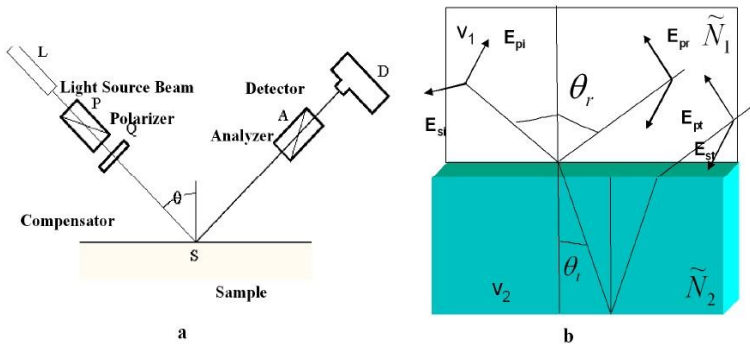
Fig. 2.11 Ellipsometry. a – a schematical view of ellipsometer; and b – light interaction with thin film

It is made of:
1. Light source beam (L): Lasers and arc lamps are typical sources for an intense light beam. For spectroscopic ellipsometers, an arc lamp of variable wavelengths is used while for a single wavelength ellipsometer a laser source is used.
2. Polarizer (P): is a linear polarizer. It generates linearly polarized light.
3. Compensator (Q): is an optical element that introduces a phase shift between the two linear polarizations, enabling the generation of an arbitrary states.
4. Sample (S): the sample represents the thin film understudy.
5. Analyzer (A): is another polarizer situated after the sample.
6. Detector (D): collected the output signal from the sample.

Interaction of light with the film layers will lead to changes in the polarization of light due to refraction and reflection. Fresnel coefficients describe the ratio of change between the incoming and the outgoing signals.

When a radio wave propagating through a medium encounters a boundary layer, which is plane and large compared to the wavelength the wave is partially

reflected and partially transmitted, respectively. If the second medium is perfectly electric conducting, then all incident energy is reflected back into the first medium without any loss of energy. The electric field strength of the reflected and transmitted waves may be related to the incident wave through the Fresnel reflection and transmission coefficients R_k and T_k respectively. The Fresnel coefficients depend on the material properties, wave polarization, angle of incidence, and material parameters which are frequency dependent. A polarized electromagnetic wave may be mathematically represented as a sum of two orthogonal components, such as vertical and horizontal, or left-hand and right-hand circularly polarized components. For an arbitrary polarization, linear superposition may be used to compute the reflected fields from a surface.

2.2.4. Microscopy

Microscopy is the technical field of using microscopes to view objects and areas of objects that cannot be seen with the naked eye. There are a lot of various microscope types (figure below) that are used in different scientific and industrial fields.
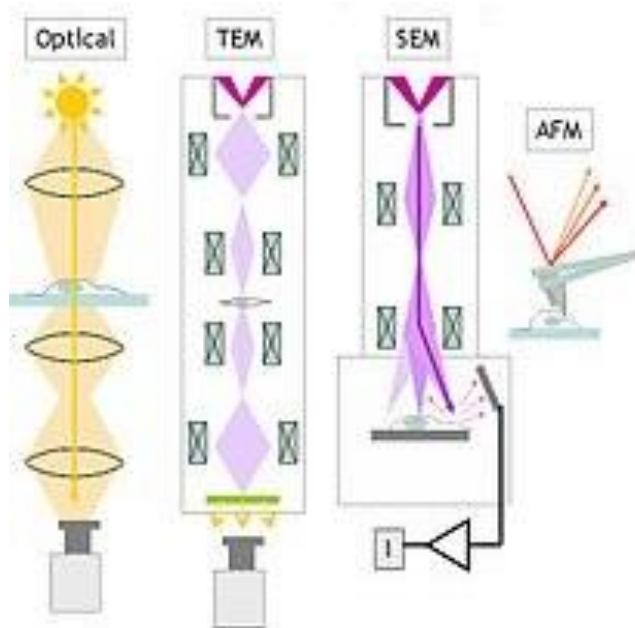
Fig. 2.12 Various types of microscopes

Optical microscopy. The morphology of the Ag/PMMA nanocomposite films and bulk composition were investigated using optical microscope Optika B-600 MET with coaxial coarse and fine focusing mechanism (0,002 mm).

Optical or light microscopy involves passing visible light transmitted through or reflected from the film through lenses to allow a magnified view of the film. The single lens with its attachments, or the system of lenses and imaging equipment, along with the appropriate lighting equipment, film stage and support, makes up the basic light microscope.

Scanning electron microscopy/energy dispersive spectroscopy. The morphology of the silver/polymer nanocomposite films and bulk composition were investigated in a scanning electron microscope (JSM–5610 LV) with attached energy dispersive X-ray analysis (EDX JED–2201; JEOL, Japan).

The morphology of W-Co NPs and their chemical composition were investigated with a scanning electron microscope (FEI Quanta 200 FEG) with attached energy dispersive spectroscope (Bruker XFlash® 4030).

The scanning electron microscope (SEM) is a type of electron microscope that images the films surface by scanning it with a high-energy beam of electrons in a raster scan pattern. The electrons interact with the atoms that make up the film producing signals that contain information about the film's surface topography, composition and other properties.

Energy dispersive X-ray spectrometer EDX detects all characteristic X-ray emitted from a specimen simultaneously. It allows even a specimen containing many types of elements to be analysis in a short time. Full Quantitative/Qualitative analysis procedures can be combined with X-ray digital maps, area and line element distribution using the SEM–EDX integration features.

Transmission electron microscopy. The particulars about morphology of W-Co NPs were extracted from the transmission electron microscope (JEOL JEM 1210; max. accelerating voltage 120 kV) images.

Transmission electron microscopy (TEM) is a microscopy technique in which a beam of electrons is transmitted through the specimen, interacting with the specimen as it passes through. An image is formed from the interaction of the electrons transmitted through the specimen.

Atomic force microscopy. Surface morphology of PLC coatings have been characterized by atomic force microscope (AFM NT–206) using V–shaped ULTRASHARP Si cantilever (force constant 1.5 Nm^{-1}). The measurements were performed using tapping mode. Corresponding software was used for the evaluation of the roughness parameters of coatings within the scanned area of 3 μm × 3 μm and 10 μm × 10 μm.

Surface morphology of Ag/PVP nanocomposites films was investigated by atomic force microscope (AFM) NT–206. V–type silicon cantilever NSC11/15 (constant force 3 N/m, resonant frequency 21 kHz) was used for AFM measurements in tapping mode. Mechanical properties of Ag/PVP films were determined from load-distance measurements using AFM.

Characteristics of the AFM: maximum scan field area: up to 30 × 30 μm; measurement matrix up to 512 × 512 points and more; maximum range of measured heights: 4 μm; lateral resolution: 2 nm, vertical resolution: 0.1 – 0.2 nm.

The atomic force microscope (AFM) is a very high resolution type of scanning probe microscopy with demonstrated resolution of fractions of a nanometer more than 1000 times better than the optical diffraction limit. The AFM is one of the foremost tools for imaging, measuring and manipulating matter at the nanoscale. The information is gathered by tapping the surface with a mechanical probe. Piezoelectric elements that facilitate tiny but accurate and precise movement on command enable the very precise scanning. The technique involves imaging a coating through the use of a probe or tip, with a radius of 20 nm. The tip, which is attached to the end of a cantilever 100 to 200 μm long, is held several nanometres above the surface using a feedback mechanism that measures surface–tip interactions on the scale of nN. A detector measures the cantilever movement as the tip moves over the coating. From these tip movements and data from the detector, a computer is used to reconstruct a map of the surface morphology. The forces between the tip and the coating surface (van der Waals, magnetic, electrostatic) cause the cantilever to bend or deflect are shown in Fig. 2.13 as function of tip to coating distance. The force most commonly associated with atomic force microscopy is an interatomic force called the Van der Waals force.
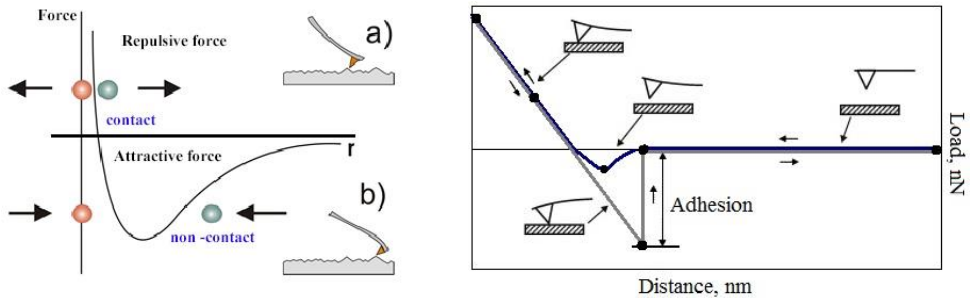
Fig. 2.13 Interatomic force vs. distance curve: a) repulsive force, b) attractive force

There are two AFM modes:

1. Contact mode (soft physical contact) is the simplest AFM method. In the contact mode, the tip scans across the coating surface, coming into "direct" physical contact with the coating. As the probe tip scans, varying topographic features cause deflection of the cantilever. The force here is usually repulsive. The amount of motion of the cantilever or the force it applies to coating can then be used in a feedback loop to control the Z piezo, maintaining constant cantilever deflection. In this way, topographic data is obtained.

2. In the non-contact mode, the cantilever is oscillated near the surface of a coating at its resonant frequency. The spacing between the tip and surface is on the order of tens to hundreds of angstroms. As the probe gets closer to the coating

70

surface, the attractive force between the tip and coating (largely a result of long-range Van der Waals interaction) will change the oscillation amplitude and the changes in phase can be detected and used by the feedback loop to produce topographic data. Amplitude detection is the non-contact method usually used for high-amplitude oscillation. Phase detection is the method usually used when the oscillation amplitude is relatively small and/or higher sensitivity is needed for stable feedback. Non-contact AFM method is ideal for scanning soft and adhesive coatings, for example polymers, because takes place without any physical contact between the probe tip and coating surface.

2.2.6. Raman spectroscopy

The structure of experimental as-prepared and irradiated polymer like a-C:H coatings was *ex-situ* characterized using Raman spectroscopy (RS). RS of experimental coatings were obtained in the range of $1000 - 2000$ cm^{-1} using Ivon Jobin spectrometer with a Spectra Physics Nd:YAG laser ($\lambda = 532.3$ nm, 50 mW at a 0.3 mm spot size). The overlapped background corrected Raman spectral bands were fitted with multi-Gaussian contours, using Least Square Fitting software.

RS is a fast and non-destructive method for the characterization of carbon materials. All carbon show common features in their RS in the $800 - 2000$ cm^{-1} region, the so called *G* and *D* peaks, which lie at around 1560 and 1360 cm^{-1}, respectively for visible excitation, and the *T* peak at around 1060 cm^{-1}, which is only seen for UV excitation. The *G* peak is due to the bond stretching of all pairs of sp^2 atoms in both rings and chains. The *D* peak is due to the breathing modes of sp^2 atoms in rings. The T peak is due to the C–C sp^3 vibrations (Ferrary and Robertson, 2004; Ferrary, 2002; Rodil et al., 2001).

The Raman effect occurs when electromagnetic radiation affects on a molecule and interacts with the polarizable electron density and the bonds of the molecule in the phase (solid, liquid or gaseous) and environment in which the molecule finds itself. For the spontaneous Raman effect, which is a form of inelastic light scattering, a photon (electromagnetic radiation of a specific wavelength) excites (interacts with) the molecule. The intensity of the Raman scattering is proportional to the electric dipole-electric dipole polarizability change. The Raman spectra (Raman scattering intensity as a function of the Stokes and anti-Stokes frequency shifts) is dependent on the rotational and vibrational energy levels of the ground electronic states of the coating. This dependence on the electric dipole-electric dipole polarizability derivative differs from infrared spectroscopy where the interaction between the molecule and light is determined by the electric dipole moment derivative, the so-called atomic polar tensor; this contrasting feature allows one to analyze transitions that might not be IR active via Raman spectroscopy, as exemplified by the rule of mutual exclusion in centrosymmetric molecules. Bands which have large Raman intensities in many cases have weak infrared intensities and vice versa. For very symmetric molecules, certain vibrations may be both infrared

and Raman inactive (within the harmonic approximation). In those instances, one can use a technique inelastic incoherent neutron scattering to determine the vibrational frequencies.

2.2.7. Photon correlation spectroscopy

Photon Correlation Spectroscopy (PCS) is based on dynamic light scattering. The time decay of the particles caused by the Brownian motion is used to estimate the size of nanoparticles through the Stokes-Einstein relation. At fixed temperature T the method requires the knowledge of the viscosity of the liquid for the estimation of the average particle size and its distribution function. According to temperature and viscosity liquid molecules are moving at a fixed speed. While they run into a particle suspended in the liquid an elastic pulse is resulting. This impact moves the particle in accordance to its size. Small particles will react rather fast while rough particles will move slower as they also may be impacted by more than one molecule from different directions at the same time because of their bigger volume.

The effect can be described as diffusion by the Stokes-Einstein equation:

$$D(x) = \frac{k_B T}{3\pi\eta x} ; \qquad (2.5)$$

where D – diffusion constant (coefficient); k_B – Boltzmann constant; T – absolute temperature; η – liquids dynamic viscosity; x – particle diameter.
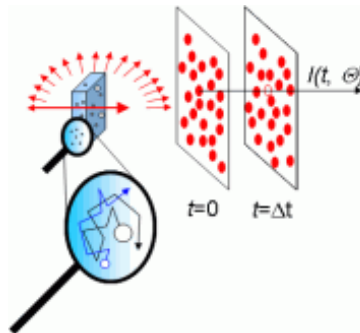
Fig. 2.14 The Brownian motion results from impacts of the movement of the molecules of the suspending fluid on the particles

A laser beam is diffracted by sub-micron particles in suspension. The spread of particles causes rapid fluctuations in scattering intensity of the laser around a mean value at a certain angle (varying from 10 to 90°) and this depends on particle size. The calculated correlation function results in a diffusion coefficient for a given temperature and viscosity, that can be converted into particle size. The technique is used to identify the average particle size in a range between 3 and 3000 nm. The measurements result in an average and mode effective hydrodynamic diameter and polydispersity index.

72

As it was mentioned above PCS is based on the Brownian motion enabled by elastic pulses between liquid molecules and particles. Any minute particle suspended in a liquid (or gas) moves chaotically under the action of collisions with surrounding molecules. The intensity of this chaotic motion is increased with an increase in temperature. The main physical principle of Brownian motion is that the mean kinetic energy of any molecule of a liquid (or gas) is equal to the mean kinetic energy of a particle suspended in this medium. The mean kinetic energy of forward motion E can be written as:

$$E = \frac{mv^2}{2} = \frac{3kT}{2};$$ (2.6)

where m – mass of a particle, v – velocity of a particle, k – the Boltzman constant, and T – temperature.

It is seen that mean kinetic energy of Brownian motion is proportional to the temperature. With a random velocity, a Brownian particle will move in a disorderly path, and will progress with time away from its original location. Calculations show that the mean-square displacement $r^2 = x^2 + y^2 + z^2$ of a Brownian particle is described by the equation:

$$r^2 = 6kTBt;$$ (2.7)

where B – mobility of the particle, which is inversely proportional to the medium viscosity and the size of the particle; k – the Boltzman constant, T – temperature; t – time.

2.3.   Materials and preparation of samples

2.3.1.   Polymer like carbon coatings

Polymer like a-C:H carbon coatings were synthesized by PECVD method at room temperature from pure (99%) acetylene (C_2H_2) in RF (13.56 MHz) dual-plasma reactor. Two parameters were varied when producing experimental coatings:

Coating fabricated varying the bias voltage. Bias voltage varied from 80 V to 480 V as well as primary ion current varied from 1.0 to 1.4 mA, keeping gas flow rate of 5,6 cm^3/s. Deposition pressure of 25 Pa was kept during entire deposition process. Deposition time of all coatings was 420 s.

Coating fabricated at different temperatures. Deposition of carbon coatings was performed at different temperatures ranging from 298 to 673 K using acetylene (C_2H_2) as a precursor. Deposition time of PLC coatings was 300 seconds. Deposition pressure of 33 Pa was kept during entire deposition process.

2.3.2.   Ag/polymer nanocomposites

Ag/PVP nanocomposites. Silver nitrate ($AgNO_3$) and poly (N-vinylpyrrolidone) (PVP, average MW = 10000) and sodium dodecyl sulfate (SDS, MW = 288.38) were obtained from Sigma Aldrich. Deionized water was prepared with a Millipore water purification system.

1 g of PVP and 170 mg of AgNO$_3$ was dissolved in 4 ml and in 1 ml water, respectively. Ag$^+$ salt's solution was admixed to PVP solution. 100 μm of 20% of SDS was dropped to Ag/PVP colloid as a surfactant.

Ag/PVP films were deposited on the silica substrates. Prior the deposition the substrates were sonically pre-treated in acetone for 10 min., chemically etched in the warm special chrome solution (K$_2$CrO$_7$ + H$_2$SO$_4$ + H$_2$O) for 10 min, and dried in the air stream. Ag/PVP films were spin-coated using "DYNAPERT PRECIMA" centrifuge from Ag/PVP colloidal solution on the pre-treated silica substrates at 1800 rpm for 60 s and dried in electrical oven at 100 °C for 10 min.

Ag/PVP nanocomposite films were obtained irradiating deposited Ag/PVP films by UV light source (Hibridas Exposure Unit MA4, power 1200 W, wavelength 300 – 400 nm). Applied UV exposure time of 5 min. was sufficient enough for photoreduction of Ag ions and formation of silver nanoparticles.

Ag/PMMA nanocomposites. Poly-methyl methacrylate (PMMA) solution with metal powder (Ag) additives was prepared dissolving 0.001 M of AgClO$_4$ in 50 ml of 1% PMMA solution in chloroform. ~ 1 mm thin layers of polymeric structures were spin-coated on the surface of polished optical glass using "DYNAPERT PRECIMA" centrifuge. Prepared films were dried in the desiccator (air humidity ~ 30%). PMMA films without additives were also produced for the comparison.

Ag/PMMA nanocomposites were produced by *in-situ* polymerization technique without using any external chemical reagent. PMMA was acting as a protective agent that restricts the mobility of silver ions during the reaction, and hence, agglomeration was mostly controlled. Chloroform was used as a solvent to form chemical network between silver nanoparticles and PMMA. Synthesis of Ag nanoparticles was performed using photocatalytic reduction of silver atoms directly in a thin layer of deposited polymer. UV light source (Hibridas Exposure Unit MA4, power 1200 W, wavelength 300 – 400 nm) was used for this purpose. Applied UV exposure time of 5 min. was sufficient enough for photoreduction of Ag ions and formation of silver nanoparticles.

3.3.   Metal alloy/polymer nanocomposites

W-Co NPs were electrochemically synthesized in aqueous electrolyte containing 0.05 M of cobalt sulfate (CoSO$_4$ · 7H$_2$O, Aldrich 99.0 %) and 0.2 M of sodium tungstate (Na$_2$WO$_4$ · 2H$_2$O, Aldrich 99.0 %) as the source of metal species, and 0.25 M tri-sodium citrate dehydrate (Na$_3$C$_6$H$_5$O$_7$ · 2H$_2$O, Lachema 99.0 %) as the complexing and buffering agent. The 0.01 mM of sodium dodecylsulphate (CH$_3$(CH$_2$)$_{11}$OSO$_3$Na, Merck 99.0 %) was added to the mixture as a surfactant and stabilizer of synthesized W-Co NPs in electrolyte. All reagents were dissolved in double-distilled water with specific conductivity of < 0.5 μS·cm^{-1}. Prepared at room temperature electrolyte was weakly alkaline (pH = 9.1), however pH value of heated up to the working temperature of 60 °C electrolyte was slightly lower i.e., 8.5.

2.4. Characterization of samples

2.4.1. Polymer like carbon coatings

Coating thickness, ractive index and extinction coefficient were obtained using laser ellipsometer Gaertner 117 with He-Ne laser ($\lambda = 632.8$ nm).

The chemical bonding structure of coatings was studied by means of infrared spectroscopy. IR spectra of coatings were measured in the range of $650 - 4000$ cm^{-1} using FTIR spectrometer Nicolet 5700.

The structure of carbon coatings was ex-situ characterized using Raman spectroscopy (RS). RS of experimental coatings were obtained in the range of $1000 - 2000$ cm^{-1} using Ivon Jobin spectrometer with a Spectra Physics Nd:YAG laser ($\lambda = 532.3$ nm, 50 mW at a 0.3 mm spot size). The overlapped background corrected Raman spectral bands were fitted with multi-Gaussian contours, using Least Square Fitting software.

Optical reflectance spectra of coatings were obtained in the wavelength range of $200 - 850$ nm using the USB4000-UV-VIS spectrometer with a special filter.

Surface morphology of carbon coatings has been characterized by atomic force microscope (AFM NT–206) using V–shaped ULTRASHARP Si cantilever (force constant 1.5 Nm^{-1}). The measurements were performed using tapping mode. Corresponding software was used for the evaluation of the roughness parameters of coatings within the scanned area.

2.4.2. Ag/polymer nanocomposites

Bonding structure of experimental coatings was investigated using Fourier transform infrared spectrometer Bruker Vertex 70, in the wavenumber range from 400 cm^{-1} to 4000 cm^{-1}, with a resolution of 0.5 cm^{-1}.

Optical spectra (carrying information about plasmonic properties of material) of the Ag/PVP nanocomposite films were measured using UV-VIS Avantes UV/VIS/NIR AvaSpec–2048 spectrometer in the wavelength range $190 - 1100$ nm. Surface morphology of Ag/PVP nanocomposites films was investigated by atomic force microscope (AFM) NT–206. V–type silicon cantilever NSC11/15 (constant force, 3 N/m, resonant frequency, 21 kHz) was used for AFM measurements in tapping mode. Elastic properties of Ag/PVP films were determined from load-distance measurements using AFM. The thickness of Ag/PVP nanocomposite films was measured using custom made scratch testing apparatus and AFM NT–206.

The morphology of the coatings and bulk composition were investigated using a scanning electron microscope (JSM–5610 LV) with attached energy dispersive X-ray analysis (EDX JED-2201; JEOL, Japan) and/or using optical microscope Optika B–600 MET.

3.4. Metal alloy/polymer nanocomposites

Two commercially available monochromatic lasers: red beam (wavelength, $\lambda = 640$ nm, power, $N = 1$ mW) and green beam (wavelength, $\lambda = 532$ nm; power, $N = 50$ mW) were used for irradiation of electrolyte after entire sonoelectrochemical synthesis procedure searching for Tyndall effect which proves the presence of differently sized nanoparticles in electrolyte. The size of synthesized W-Co NPs and distribution according to their size was investigated in details by photon correlation spectroscopy (PCS) using Delsa™ Nano C (USA, Beckman Coulter) analyzer.

The morphology of W-Co NPs and their chemical composition were investigated with a scanning electron microscope (SEM, FEI Quanta 200 FEG) with attached energy dispersive spectroscope (EDS, Bruker XFlash® 4030). The solution or, more precisely, suspension of W-Co NPs in trichloromethane was dripped on a polished silicon wafer (20 mm x 20 mm) and particles remaining on the silicon substrate after the evaporation of volatile organic solvent were analyzed. More detailed information about morphology of W-Co NPs was extracted from the transmission electron microscope (TEM, JEOL JEM 1210; max. accelerating voltage 120kV) images.

2.5. Modification of samples

2.5.1. Polymer like carbon coatings

Coatings produced at different bias voltage were irradiated with gamma photons in teletherapy unit ROKUS-M with ^{60}Co source (the activity of ^{60}Co source at the time of investigation was $4.28 \cdot 10^{13}$ Bq; the dose rate was 2.8 mGy/min) and with 12 MeV electrons, generated in medical linear accelerator Clinac DMX (the dose rate was 2 Gy/min). Irradiation dose was the same – 2 Gy.

Irradiation of coatings produced at different deposition temperatures to high energy (6 MeV) electrons was performed in medical linear accelerator Clinac2100C (VARIAN) at the dose rate of 3 Gy/min. Maximal irradiation dose was 3 Gy.

2.5.2. Ag/polymer nanocomposites

Teletherapy unit "ROKUS–M" with ^{60}Co (1.25 MeV) source was used to irradiate Ag/PVP nanocomposites. The activity of ^{60}Co source was $6.52 \cdot 10^{13}$ Bq and the dose rate was 6.5 mGy/s. The distance between the source and irradiation surface (SSD) was 75 cm and the irradiation field was 10×10 cm^2. Total irradiation dose varied in the range $2 – 50$ Gy.

UV exposed PMMA and polymeric nanocomposite (Ag/PMMA) films were irradiated to different doses up to 2 Gy. The dose rate was 3.5 mGy/min and the energy of X-ray photons generated in X-ray diffractometer DRON-3 was 35 keV. Diffractometer DRON-3 was equipped with a single crystal graphite flat monochromator for transmitting only a narrow Cu K$_\alpha$ wavelength ($\lambda = 0.15405$ nm).

Irradiation of films was performed with the aim to investigate soft X-ray radiation induced modification of their optical properties, caused by two processes: polymer degradation and formation of metal nanoparticles within polymer matrix.

3. RESULTS AND DISCUSSIONS

3.1. Polymer like carbon coatings

Modification of polymer like amorphous hydrogenated carbon (a-C:H) coatings fabricated varying deposition parameters has been performed applying high energy photons and electrons. Mechanisms of structural changes in irradiated coatings have been analyzed and discussed on the basis of the obtained results in order to assess the role of hydrogen in the formation of the stable 3D network structure of tetrahedral configured carbon atoms (sp^3 hybridization) with embedded small graphite clusters or formation of polymer nanocomposite similar structure consisting of polymer like carbon matrix with sp^2 clusters in it. Discussed new formations have unique physical and chemical properties and have a broad spectrum of different applications.

In this work modification of two types of polymer like a-C:H coatings have been investigated: coatings produced varying bias voltage and coatings produced varying deposition temperature.

3.1.1. Carbon coatings fabricated varying bias voltage

Carbon coatings were synthesized at room temperature from pure (99 %) acetylene (C_2H_2) in RF (13.56 MHz) dual-plasma reactor, on silica substrates. The bias voltage varied from 80 V to 480 V as well as primary ion current varied from 1.01 to 1.36 mA, keeping gas flow rate of 5.6 cm^3/s. Deposition pressure of 25 Pa was kept during the deposition process as well as deposition time of all coatings was 420 s. Information on deposition parameters is provided in the Table 3.1.

Table 3.1 The deposition parameters of carbon coatings

Parameters	RP3	RP4	RP5	RP6	RP7	RP8	RP9
Bias voltage, V	80	100	120	200	300	400	480
Primary ion current, mA	1.16	1.04	1.03	1.01	1.08	1.16	1.36
Initial chamber pressure, Pa	22.22	26.56	26.56	26.56	24.24	23.19	24.24
Chamber pressure with forming gas, Pa	29.23	29.23	29.23	29.23	45.44	45.44	45.44
Substrate heating time, s	120	120	120	120	180	180	180

Deposited coatings were prepared for the exploration. Index RP was assigned to the "as prepared" coatings, RE – to the electron beam irradiated coatings and RG – to the coatings irradiated by photons.

Characterization of as prepared coatings was performed using the results of null laser ellipsometry. Ellipsometric parameters were measured at three tilting angles and in at least three randomly selected locations on the coating's surface, as it is indicated in Fig. 3.1 for RP4 coating.
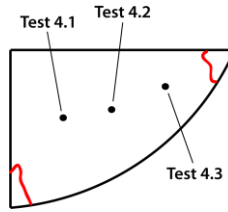
Fig. 3.1 Measurement points on the RP4 coating surface

The particular model of the formed structures were applied. Model represents structure, containing of a quartz target and deposited carbon coating on the top of the coating (Table 3.2). A set of measured ellipsometric parameters for the experimental coating RP4 is shown in the Table 3.3.

Table 3.2 Applied model

Model	Refraction index	Extinction coefficient
Carbon coating	1.5 – 1.7	0 – 0.200
quartz 0.5mm	3.882	0.019

Table 3.3 Measured ellipsometric parameter of the RP4 coating

Meas. loc.	Meas. angle, deg	P_1	A_1	P_{2n}	A_{2n}	P_2	A_2	Ψ	Δ	Ref. index	Extinction coefficient	Coating thickness, nm
Test 4.1	30	43.9	40.3	133.9	139.7	133.8	139.8	40.3	182.3	1.542	0.003	1160
	50	65.0	35.0	155.0	145.0	155.2	145.9	34.6	139.8			
	70	53.9	28.0	83.9	152.0	84.3	151.4	28.3	98.2			
Test 4.2	30	48.0	40.5	138.0	139.5	137.9	139.9	40.3	174.1	1.607	0.010	1003
	50	20.1	50.1	110.1	129.9	110.4	132.0	49.1	129.5			
	70	72.7	19.3	162.7	170.7	161.9	170.8	9.3	125.4			
Test 4.3	30	45.1	40.4	135.1	139.6	134.9	139.3	40.6	180.0	1.568	0.006	1225
	50	43.8	69.2	133.8	110.8	132.6	110.4	69.4	183.6			
	70	59.9	10.4	149.9	169.6	148.8	169.6	10.4	151.3			
								Averaged		*1.572*	*0.006*	*1129*

The same evaluation procedure was applied for all fabricated experimental coatings. Results of the evaluation are provided in Table 3.5.

Table 3.4 The characteristics of all fabricated coatings

Parameters	Experimental coatings						
	RP3	RP4	RP5	RP6	RP7	RP8	RP9
Bias voltage, V	80	100	120	200	300	400	480
Refraction index	1.615	1.572	1.626	1.675	1.669	1.690	1.690
Extinction coefficient	0.007	0.006	0.003	0.004	0.006	0.010	0.011
Coating thickness, nm	766	1129	856	1343	1005	1001	854

It was found, that applying the model for the performance of the test measurements at different locations of the same coating, overestimation of the refractive index was possible. These uncertainties might be related to the assumption regarding constant SiO_2 layer thickness and have an impact on the average refraction index values of a certain coating leading to misinterpretation of the obtained results. To overcome this problem, experimental data collected following coating structure was considered for further investigation.

Taking into account estimated refraction index values (Fang, 2009) investigated carbon coatings were identified as amorphous hydrogeneted/polymer like carbon coatings. Starting with RP6 carbon coatings were identified as coatings containing graphite clusters. It was found, that at the lowest bias voltage (80 V, RP3) coating thickness was not uniform and the refractive index at different coating surface points varried significantly: from 1.42 to 1.69. Well pronounced polymer like coating structure with a surface roughnes $R_q = 0.9$ nm was observed at 100 V bias (RP4), where refracton index values at different measurement points varried within interval 1.541 – 1.610; however surface thickness was not uniform (Fig. 3.2 A).

X:10.9um Y:10.9um Z:9.9nm [144.0:1]
Ra: 0.7nm Rq: 0.9nm

A

X:10.9um Y:10.9um Z:8.5nm [128.6:1]
Ra: 0.7nm Rq: 0.9nm

B

X:10.9um Y:10.9um Z:3.7nm [294.5:1]
Ra: 0.3nm Rq: 0.4nm

C
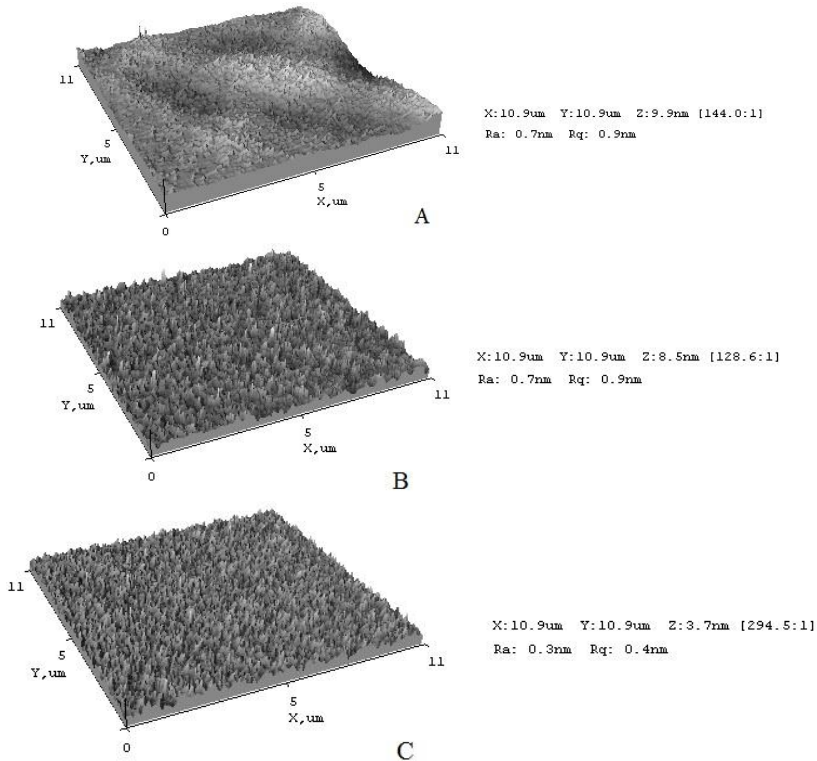
Fig. 3.2 Three dimensional AFM images of as prepared coatings: A – AFM image of RP4 coating: $R_q = 0.9$ nm, $R_a = 0.7$ nm; B – AFM image of RP6 coating: $R_q = 0.9$ nm, $R_a = 0.7$ nm; C – AFM image of RP8 coating: $R_q = 0.4$ nm, $R_a = 0.3$ nm

The increase of bias voltage lead to formation of some graphite clusters within polymer matrix of experimental coating. At 200 V (RP6) refractive index values of 1.810 and 2.143 were registered at two randomly selected measurement points on the coating surface. Due to this the number of ellipsomeric measurement points on the coating surface was increased to 10 as total. The refractive index values at these points varried arround 1.65 ± 0.005 indicating polymer like carbon structure. Surface structure of the RP6 coating was more uniform as compared to coatings produced at lower bias, however surface roughness remained the same $R_q = 0.9$ nm (Fig. 3.2 B). The average refraction index values were not changing significantly and varried arround 1.74 ± 0.03 when the bias voltage was increased to ≥ 300 V, but the coating surface became smoother ($R_q = 0.4$ nm) (Fig. 3.2 C).

After the analysis of initial coatings, the modification of carbon coatings using high energy electron and photon beams was estimated. Considering that radiation impact on amorphous/polymeric structures is responsible for the scission and cross-linking of polymeric chains that lead to structural rearrangements, experimental coatings were irradiated to high energy (12 MeV) electrons generated in medical linear accelerator Clinac DMX (VARIAN). The dose of 2 Gy was delivered at 2 Gy/min dose rate. For the comparison some of coatings were irradiated by gamma photons in teletherapy unit ROKUS–M with ^{60}Co source. Irradiation dose was the same – 2 Gy at the dose rate of 0.281 Gy/min.

Suggesting that the model developed by Liu et al. (2004) and Saito et al. (2000) and adapted by us for electron beams describes the behavior of hydrogen in the coating properly, experimental evaluation of the structure and properties of the irradiated coatings was performed applying ellipsometry, UV–VIS spectrometry, Raman spectroscopy, FTIR spectroscopy, AFM and other relevant coating examination methods.

Raman spectra of experimental coatings were obtained in the range of 1100 – 1800 cm^{-1}. The D and G bands were fitted simultaneously by Gaussian at a linear background. G position was chosen as the maximum of the function rather than its center, to allow comparison with symmetric curve fits. Robertson (2002) and Ferrari (2004) have proposed that G peak observed in 1500 – 1630 cm^{-1} range is due to the bond stretching of all sp^2 sites in rings and chains. The D peak becomes active only in the presence of disorder. The full width at half-maxima ($FWHM$) of D and G peaks as well as the integral intensity ratio between D and G peaks (I_D/I_G) was estimated. All evaluation and calculation results are provided in Table 3.6.

It was found that D peak location of as prepared coatings varied in the range from 1309 cm^{-1} to 1369 cm^{-1}, whereas G peak's location – from 1526 cm^{-1} to 1581 cm^{-1}. Full width at half-maxima $FWHM_G$ of the G peak varied from ~ 90 cm^{-1} to ~ 140 cm^{-1} as well as the full width at half-maxima $FWHM_D$ of the D peak varied from ~ 140 cm^{-1} to ~ 180 cm^{-1} respectively. In line with increasing bias voltage the estimated I_D/I_G ratio of all coatings is increasing in the range from 1.09 to 1.19. These findings indicate that coatings most probably are polymer like and contain

considerably high number of C–H sp^3 bonds as it is described in Das et al., (2011) and Novikov et al. (1997) papers. However, it should be noted that increasing intensity ratio I_D/I_G is related to the increase of sp^2 phase in the structure, though sp^3/sp^2 ratio may depend on the other properties of the coating structure and on the hydrogen content in it. Similar results were obtained in Casiraghi et al. (2007) and Tai et al. (2006) research.

Table 3.5 The evaluation and calculation results of Raman spectroscopy

ID No	Bias voltage, V	Characteristics of Raman spectra of as prepared coatings				
		D, cm^{-1}	$FWHM_D$, cm^{-1}	G, cm^{-1}	$FWHM_G$, cm^{-1}	I_D/I_G
RP3	80	1319	160	1581	100	1.09
RP4	100	1309	180	1562	140	1.13
RP5	120	1328	180	1549	130	1.15
RP6	200	1318	150	1550	110	1.18
RP7	300	1323	150	1545	110	1.18
RP8	400	1369	150	1526	100	1.19
RP9	480	1352	140	1548	90	1.19
ID No	Bias voltage, V	Characteristics of Raman spectra of electron irradiated coatings				
		D, cm^{-1}	$FWHM_D$, cm^{-1}	G, cm^{-1}	$FWHM_G$, cm^{-1}	I_D/I_G
RE3	80	1396	120	1617	70	1.46
RE4	100	1380	130	1578	100	1.43
RE5	120	-	-	-	-	-
RE6	200	1384	100	1558	60	1,38
RE7	300	-	-	-	-	-
RE8	400	1396	120	1578	90	1.34
RE9	480	-	-	-	-	-

Analyzing Raman spectra of experimental coatings after the irradiation with high energy electrons it was found that the intensity, location and *FWHM* of characteristic *D* and *G* peaks have changed. Raman shift of the *G* (graphite) and *D* (diamond) peak towards higher wave numbers were observed for the all experimental coatings, the I_D/I_G ratio increased as compared with initial coatings. The *D* and *G* peaks become more intensive. These changes are related to the rearrangements in the coating structure: decreased number of sp^3 bonds, increasing of sp^2 sites and reduced amount of bonded hydrogen coatings (Ferrary, 2004).

The Raman spectra of experimental coatings are presented in Fig. 3.3, Fig. 3.4, Fig. 3.5 and Fig. 3.6.
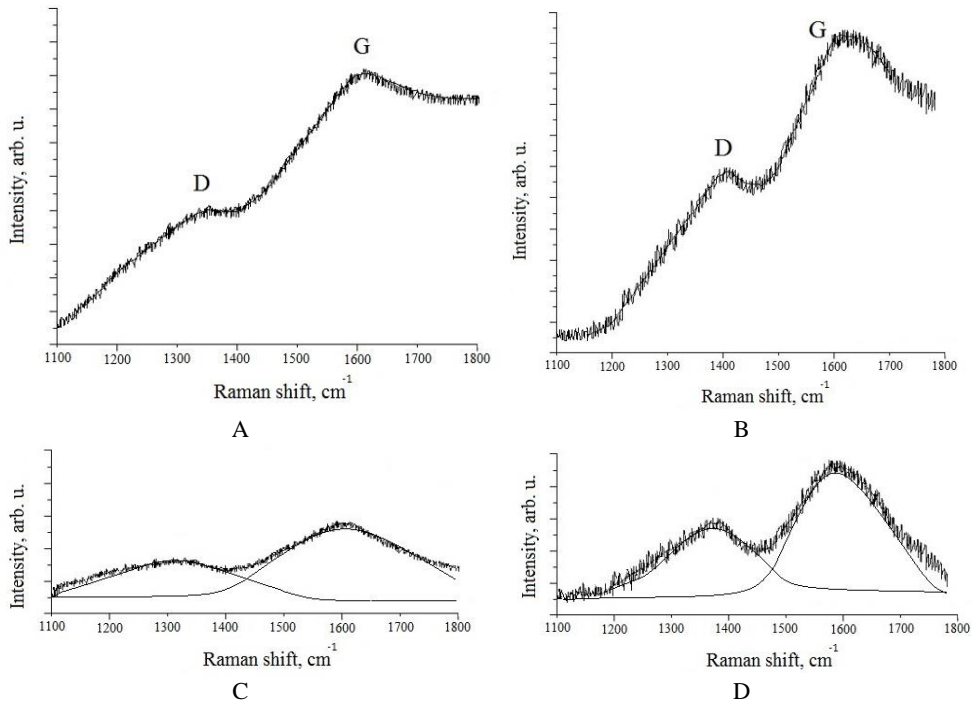
Fig. 3.3 Raman spectra of experimental coatings deposited at lowest 80 V bias: A, C – as prepared (RP3), B, D – irradiated with high energy (12 MeV) electrons (RE3)

Fig. 3.3 shows the as prepared (RP3) and irradiated with 12 MeV energy electrons (RE3) Raman spectra of coatings deposited at lowest bias (80 V). The D peak means the disorder carbon bonding centered at around 1319 cm^{-1} and G peak means the graphite carbon bonding located at around 1581 cm^{-1}. After irradiation the D peak gradually grows and its height is less than that of G peak, whereas Raman line shapes have a slight skewed potential for D and G peak to shift higher peak position. The G peak position shifts from 1581 cm^{-1} (as prepared) to 1617 cm^{-1} (irradiated) but $FWHM_G$ of G peak decreases from 100 cm^{-1} to 70 cm^{-1}, respectively. The same trend is observed in the D peak position shift. The D peak position shifts from 1319 cm^{-1} (as prepared) to 1396 cm^{-1} (irradiated) and the $FWHM_D$ of D peak decreases from 160 cm^{-1} to 120 cm^{-1}, respectively. The relative ratio of the D peak to G (I_D/I_G) is 1.09 (for as prepared coating) increases up to 1.46 (for the irradiated coating) and this means that coating starts to increase its disorder performance due to slight graphitization and losing the hydrogen as a result in the graphitization conversion for C–C and C–H sp^3 bonded carbon to transform to C–C sp^2 bonded carbon (Tai et al., 2006). The intensity of D peak increases because of conversion of sp^3 bonds to sp^2 bonds, desorption of hydrogen and conversion of carbon structure to nanocrystalline graphite (Chu and Li, 2006). The G peak value of 1617 cm^{-1} (Fig.

3.3 D) is attributed to the sp^2 $C=C$ and indicates olefinic configuration of the bonds (Ferrary, 2004).
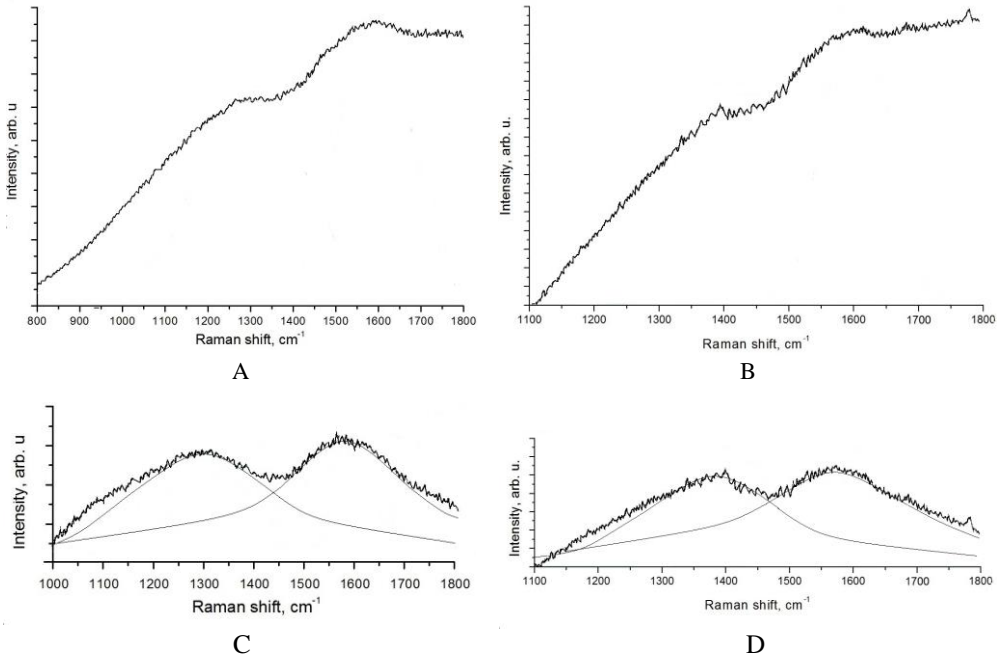
Fig. 3.4 Raman spectra of experimental coatings deposited at 100 V bias: A, C – as prepared (RP4), B, D – irradiated with high energy (12 MeV) electrons (RE4)

The Raman spectra of the coating deposited at 100 V bias (Fig. 3.4 A) consists from the two separated peaks attributed to well-known *D* and *G* bands (Ferrary, 2004). To estimate the positions and *FWHM* of *D* and *G* peaks, the Gaussian fitting was done. It was found that *D* peak is located at 1309 cm^{-1}, while *G* band position is at 1562 cm^{-1}. The *FWHM* of *D* and *G* peaks are 180 cm^{-1} and 140 cm^{-1}, respectively. The relative ratio of the *D* peak to *G* (I_D/I_G) is 1.13. After the irradiation with 12 MeV energy electrons both peaks (Fig. 3.4 B) changed their position, as well as peaks intensity and shape have changed too. The *D* and *G* peaks slightly intensified and shifted to the higher wave numbers – 1380 cm^{-1} and 1578 cm^{-1}, respectively. The *FWHM* of both peaks has narrowed after the irradiation with 12 MeV energy electrons from 180 cm^{-1} to 140 cm^{-1} and from 130 cm^{-1} to 100 cm^{-1}, correspondingly. The integral intensity ratio I_D/I_G has increased to 1.43 after irradiation. According to Casiraghi et al., (2007) there may be some reasons for the shape of the spectrum and *FWHM* values: changes of bonding structure in the irradiated coating (increased number of sp^2 sites), radiation induced stress and formation of clusters in the polymer like a-C:H coating's polymer matrix.
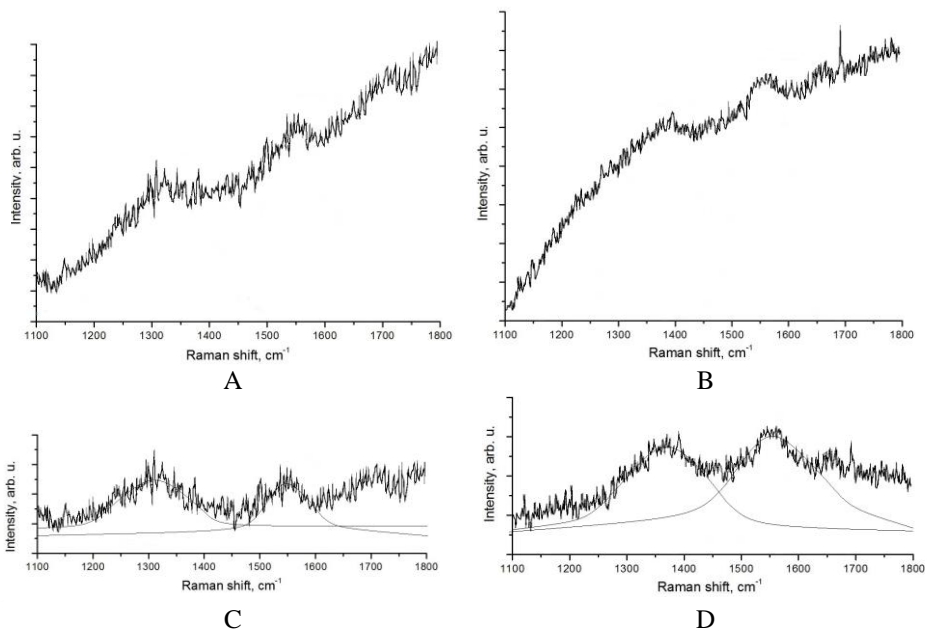
Fig. 3.5 Raman spectra of experimental coatings deposited at 200 V bias: A, C – as prepared (RP6), B, D – irradiated with high energy (12 MeV) electrons (RE6)

Examination of Raman spectra of coating deposited at 200 V bias (Fig. 3.5 A) has shown that the main D and G peaks of RP6 coating were obtained at 1318 cm^{-1} and 1550 cm^{-1}, respectively. The $FWHM$ of D and G peaks are 130 cm^{-1} and 70 cm^{-1}, respectively. The I_D/I_G ratio is high in comparison with different types of carbon coatings and shows that the relative fraction of sp^2 sites is higher than sp^3. According to Robertson (2002) and Marcinauskas et al. (2007) it is related with reduction of bond angle disorder and growth of graphite domains. After the modification with high energy electrons the structure of RE6 coating become like polymer composite with incorporated graphite domains. The main D and G peaks of coating shifted towards higher wave numbers accordingly to 1384 cm^{-1} and 1558 cm^{-1}, as well as the $FWHM$ of D and G peaks narrowed to 100 cm^{-1} and 60 cm^{-1}, respectively. The I_D/I_G ratio increased as compared with initial coating (RP6) to 1.38. The intensity of D peak increases due to reorganization of sp^3 bonds to sp^2 bonds, desorption of hydrogen as well as the narrowed $FWHM_G$ according to the formation of the strong sp^2 C=C bonds (Marcinauskas et al., 2010).

A

B

C

D
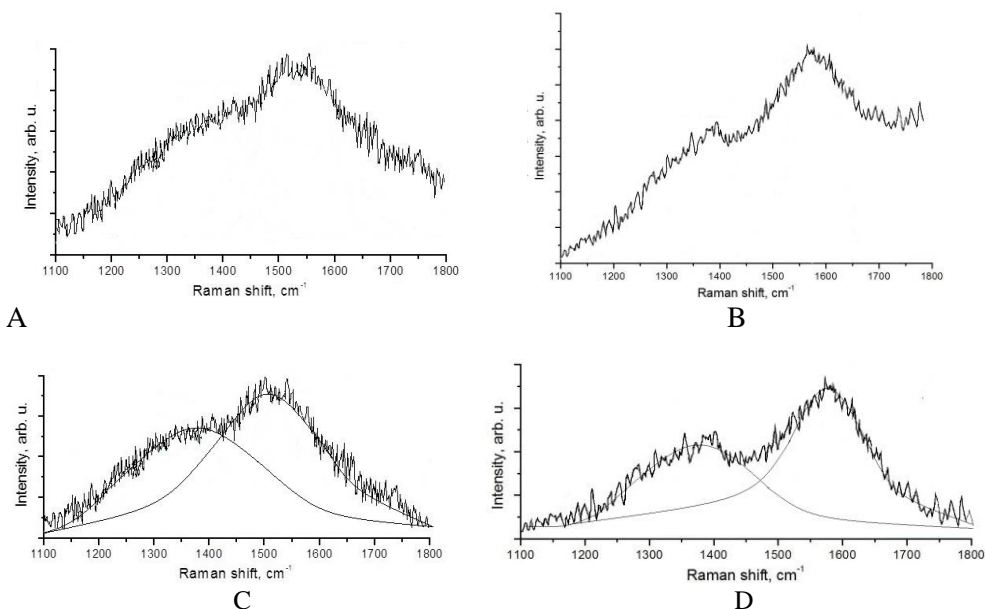
Fig. 3.6 Raman spectra of experimental coatings deposited at 400 V bias: A – as prepared (RP8), B – irradiated with high energy (12 MeV) electrons (RE8)

Analysis of Raman spectra of experimental coatings deposited at 400 V bias (Fig. 3.6) have shown, that after the irradiation D and G peaks were shifted towards higher wave numbers from 1369 cm^{-1} to 1396 cm^{-1} (D peak) and from 1526 cm^{-1} to 1578 cm^{-1} (G peak). Meanwhile I_D/I_G ratio was increased from 1.19 to 1.34, the *FWHM* of D and G peaks slightly narrowed from 150 cm^{-1} to 120 cm^{-1} and from 120 cm^{-1} and 100 cm^{-1}, respectively.

Raman spectrum of irradiated carbon coating produced at 120 V (RE5), 300 V (RE7) and 480 V (RE9) does not indicate any typical peaks related to the carbon structures in the range of 1100 cm^{-1} – 1800 cm^{-1}. According to the RS measurements we could not identify the structure and the changes of these coatings after the modification with high energy electrons.

Making presume the high energy photons entering the experimental coatings produce high energetic electron-positron pairs or recoil electrons through Compton scattering (Plaipaite-Nalivaiko et al., 2012). The electrons can break C–H bond or even C=C bond in the films, that can cause rearrangements in film structure (Plaipaite-Nalivaiko et al., 2012). Formation of the strong C–C bonds and changes of the unbound hydrogen concentration, which could be then released from the films by forming hydrogen molecules, is a result of the direct high energy photon irradiation of carbon coatings (Plaipaite-Nalivaiko et al., 2012). The shape of the spectrum and narrow *FWHM* values indicates that the production of hydrogen leads to the formation of nanocrystalline graphite clusters in experimental coatings. According to Robertson (2002) and Adliene (2008) the nano clusterization is

86

possible. It seems it is easy to rearrange films with the low density networking structure. But it is possible when the radiation produced free radicals and ions in air interact with the material (oxygen or hydrogen etching) creating the new connections at least in the surface layer of the film (especially with the unbound hydrogen). According to Robertson (2002) while the G peaks width decreases, the Urbach energy continues to increase. Urbach energy is a value of inhomogeneous disorder that shows the range of sp^2 cluster sizes present. In such a case, while Urbach energy increases, inhomogeneous disorder increases and the optical gap of PLC coatings are increasing too.

The interaction of the electrons and a-C:H film results in an ionization volume in which the target atoms are excited or ionized so as to break some of the C–H and C–C bonds. The released hydrogen atoms and some small hydrocarbon units could re-combine together to form hydrogen molecules or even methane molecules and diffuse out of the irradiated film. Therefore, a number of carbon dangling bonds would be produced. The carbon dangling bonds may rebound, under the influence of the extra deposited energy, to form a more stable carbon network.

Assuming that the mechanisms for the bond transformation from C–C to C=C under the impact of high electron energy could be similar to those happening in thermal annealing (Saito et al., 2000), if the electron flux density is significant enough ($\sim 10^{16}$ cm^{-2}) and might be described by following reactions:

$$6C(sp^3) - C(sp^3) \rightarrow C(sp^2) = C(sp^2) + 4C(sp^3) - (sp^2); \quad (3.1)$$
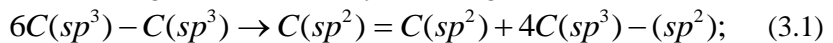
and formation of H$_2$ from sp^3-H$_n$

$$2C(sp^3) - H \rightarrow C(sp^3) - C(sp^3) + H_2; \quad (3.2)$$
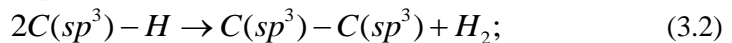
Reactions (3.1) and (3.2) are endothermic with energies of about 0.11 eV and 0.49 eV, respectively. Hydrogen loss from the irradiated film may also realize through a formation of methane, with an endothermic energy of 0.14 eV, which is actually smaller than that to form a hydrogen molecule:

$$4C(sp^3) - H + 6C(sp^3) \rightarrow CH_4 + C(sp^2) = C(sp^2) + 4C(sp^3) - C(sp^2); \quad (3.3)$$
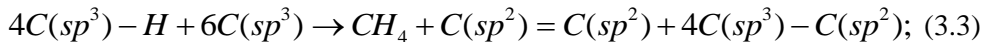
With hydrogen release and the creation of hydrogen free $C(sp^3)$–$C(sp^2)$ bonding clusters, more and more $C(sp^2)=C(sp^2)$ bonds are simultaneously produced so that they could rearrange into the bigger size of $C(sp^2)$ atom rings.

Optical properties of carbon coatings were investigated using USB4000–UV–VIS spectrometer in the 200 – 850 nm wavelength range. The UV–VIS transmittance spectra of RP6 coating (without modification), RE6 coating (after modification by electrons) and RG6 coating (after modification by photons) are shown on Fig. 3.7. Analyzing UV–VIS transmittance spectra, it is clearly seen that due to the modification with high energy electrons and photons, the transparency of experimental coatings has reduced.
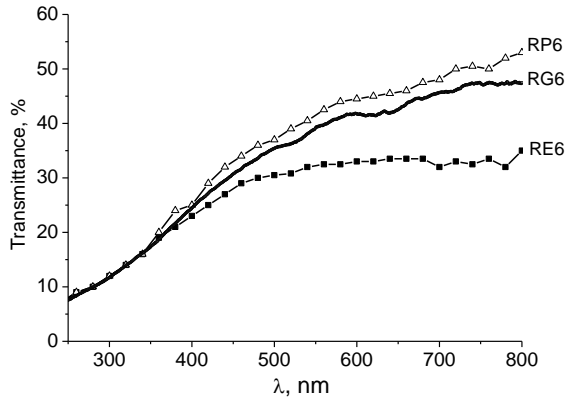
Fig. 3.7 UV–VIS transmittance spectra of RP6 coating before irradiation and after it's modification with high energy electrons RE6 and photons RG6

Decreasing tendency of UV-VIS transmittance spectra occurs due to hydrogen release from coating, restructuration processes and formation of new polymeric chains. According to the calculations and τ approximation method it was found that increasing bias voltage the refractive index increasing while the optical band gap narrowing (Table 3.6). Such trends have been observed in other author's works (Saito et al., 2000; Santra et al., 2011). On the other hand, after exposure to high-energy electrons and photons, the band gap width of experimental coatings slightly increases (Fig. 3.6).

Table 3.6 The width of optical band gap

	RP3	RG3	RE3	RP4	RG4	RE4	RP5	RP6	RG6	RE6	RP7	RP8	RG8	RE8	RP9
Bias, V		80			100		120		200		300		400		480
E, eV	2.28	2.95	3.02	1.61	1.75	1.81	1.97	1.51	1.79	1.95	1.91	1.56	1.75	1.94	1.58
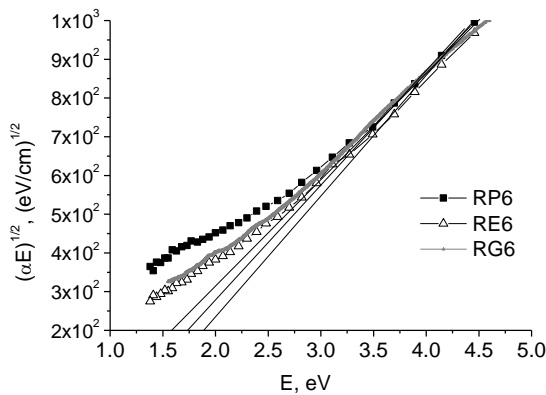
Fig. 3.8 The estimation of band gap from UV–VIS spectra

Reduced sp^3 content and changed chemical bonding structure in irradiated coatings was identified from the FTIR spectra as well. FTIR reflectance and transmittance spectra were investigated with a purpose to get additional information about chemical bonds experimental coatings. The initial FTIR reflectance spectra of the coatings RP3, RP6 and RP8 (produced at the bias voltage of 80 V, 200 V and 400 V respectively, within a time of 420 s are provided in Fig. 3.9, Fig. 3.10 and Fig. 3.11. The FTIR spectra measured after coating's irradiation with gamma photons from ^{60}Co source (RG3, RG6 and RG8) and the FTIR spectra obtained from the coating irradiated with 12 MeV electrons (RE3, RE6 and RE8) are presented in Fig. 3.9, Fig. 3.10 and Fig. 3.11 as well.

Increased IR absorption level was observed in irradiated experimental coatings as a result of rearrangements in the bonding structure due to their bombardment with high energy particles. The FTIR spectra show sp^3 CH_{2-3} (methylene) groups in asymmetric and symmetric stretching and bending modes at approximately 2900 cm^{-1}, as it is usual for hydrogenated a-C:H. It is important to note that the irradiation with high energy electrons have greater impact on substrates than irradiation with gamma photons. All the modifications could be related to hydrogen content changes in the coating, appearance and disappearance of specific bonds and links as it was observed in the case of sp^2 C=O replacement by newly created sp^2 C=C bonds. Most of the hydrogen is bonded to the sp^3 carbon and forms methylene compounds sp^3 C−H$_{2-3}$. It is clearly seen that radiation induces defects and dangling bonds that can be easily occupied by oxygen and create C=O and O−H bonds (Santra et al., 2010; Kim et al., 2004). Intensive peaks at 1723 cm^{-1} and 1107 cm^{-1} (RE3) coating are related to sp^2 C=O valence vibrations. Broad low intensity band observed in the range of 3300 cm^{-1} − 3700 cm^{-1} corresponds to the sp^1 O−H stretching vibrations. Part of this peak might be related to sp^1 carbon (C≡C−H) (Robertson, 2002). The fraction of sp^3 CH$_3$ at 1390 cm^{-1} increases depending on the type of radiation. The strong absorption at approximately 1642 cm^{-1} which is attributed to the presence of vibration mode of sp^2 C=C and indicates the presence of aromatic and olefinic configuration of the bonds. The peak at 1232 cm^{-1} (RG3, after gamma irradiation) indicates growing influence of the mixed sp^2/sp^3 C−C bonds and possible transformation from polymer like to graphite like coating. In a mixed sp^2/sp^3 network 2 types of defects might be distinguished: isolated sp^3 dangling bonds and small sp^2 clusters where the π bonds can be distorted.
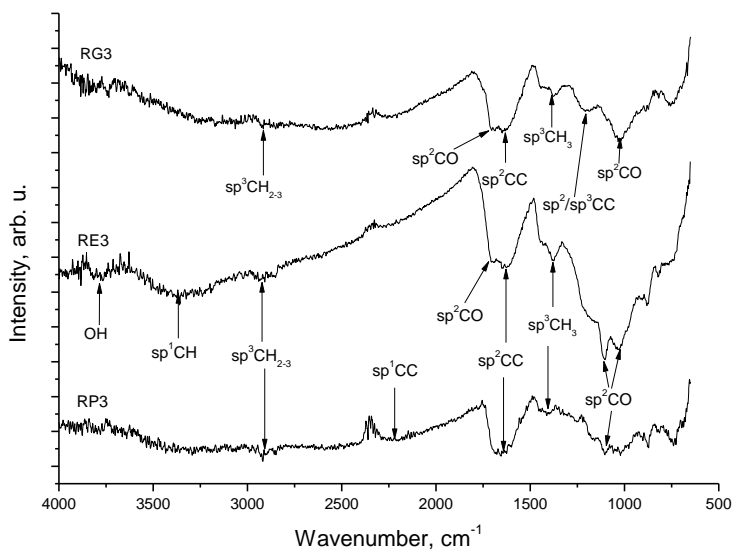
Fig. 3.9 FTIR reflectance intensity spectra of RP3 coating before irradiation and after it's irradiation with gamma photons (RG3) emitted by ^{60}Co (1.25 MeV) source and after it's irradiation with 12 MeV energy electrons (RE3)

FTIR spectrum of as prepared RP6 coating is very similar to the FTIR spectra of irradiated coatings – RG6 and RE6. Some intrinsic peaks shifted, as well as the intensity of peaks decreased. Existence of the wide band at 3100 cm^{-1} – 3400 cm^{-1} is attributed to OH bonds. Though, the width of this peak also indicates presence of the sp^1 CH sites in the films. The absorption at 2830 cm^{-1} and 2880 cm^{-1} is related to sp^3 CH$_2$ symmetric and asymmetric stretch modes, respectively. The peaks appearing at 1725 cm^{-1} and 1450 cm^{-1} indicate sp^2 C=O stretching mode and C=C bonds, respectively (Marcinauskas et al. 2011). The C=C peak suggests that carbon bonds are aromatic and olefinic configurations. Yi et al. (2009) supposed that this broadness is due to interaction between the C=C vibrations and the neighboring sp^2 C–H bonds. The absorbance bands found at about 1190 cm^{-1} and 1175 cm^{-1} are related to C–H, C–C or C–O groups. Presence of the C=O and O–H bands in the a-C:H films according to Marcinauskas et al. (2007) shows a large concentration of free radicals, which react with oxygen.
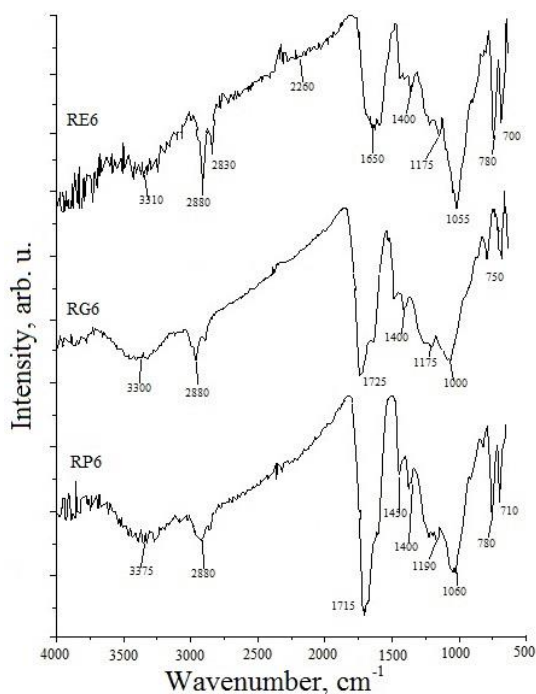
Fig. 3.10 FTIR reflectance intensity spectra of RP6 coating before irradiation and after it's irradiation with gamma photons (RG6) emitted by ^{60}Co (1.25 MeV) source and after it's irradiation with 12 MeV energy electrons (RE6)

Analyzing IR spectra of RP8 (400 V) coating it is clearly seen increased absorption level after modification with high energy photons. Broad low intensity band defining sp^1 OH stretching vibrations was observed in the range of 3300 cm^{-1} – 3700 cm^{-1} (RE8) (Robertson, 2002). Peak at 2900 cm^{-1} corresponding to the sp^3 CH$_{2-3}$ symmetric and asymmetric stretching modes that are usual for a-C:H were found in experimental coatings. All the rearrangements could be related to hydrogen content changes in the coating, appearance and disappearance of specific bonds and links as it was observed in the case of sp^2 C=O replacement by newly created sp^2 C=C bonds. Most of the hydrogen is bonded to the sp^3 carbon and forms methylene compounds sp^3 C–H$_{2-3}$. Intensive peaks (RG8 and RE8) at range from 1710 cm^{-1} to 1730 cm^{-1} coating are related to sp^2 C=O stretching mode. The band around 1480 cm^{-1} related to sp^3 CH$_3$ shifted to 1430 cm^{-1} and became more intensive and broader after irradiation. This peak could be related to sp^2 C–H in aromatic configuration of the bonds. It is possible rearrangement from polymer like to graphite like coating due to appearance of small sp^2 clusters where the π bonds can be distorted. The peak at 1210 cm^{-1} (RG8, after gamma irradiation) indicates growing influence of the mixed sp^2/sp^3 C–C bonds as well as the peak at 1230 cm^{-1} (RE8, after electron irradiation) are ascribed to sp^2/sp^3 C–C bonded carbon.

91
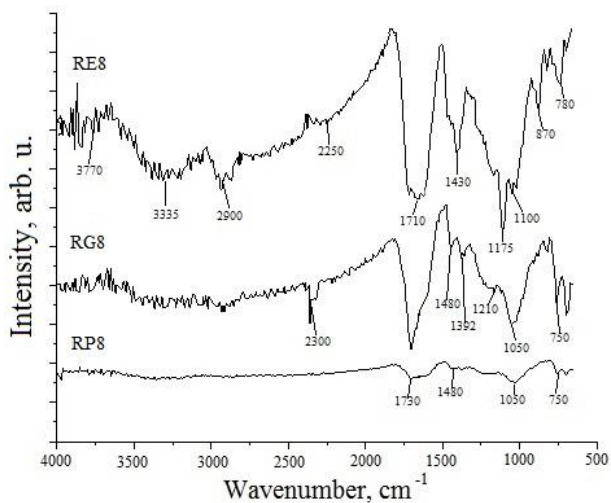
Fig. 3.11 FTIR reflectance intensity spectra of RP8 coating before irradiation and after it's irradiation with gamma photons (RG8) emitted by ^{60}Co (1.25 Mev) source and after it's irradiation with 12 MeV energy electrons (RE8)

The transmittance spectra of experimental coatings show the same structural information as the reflectance spectra for all coatings. The transmittance spectra of RP6 and RP8 coatings after their modification with photons and electrons showed below as an example (Fig. 3.12 and Fig. 3.13).
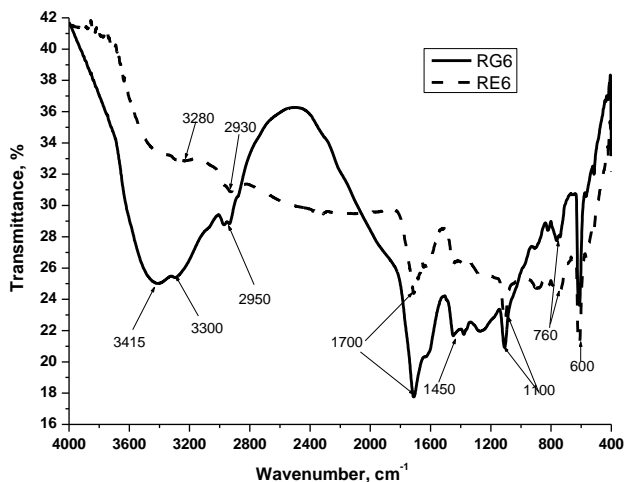
Fig. 3.12 FTIR transmittance spectra of RP6 coating after it's irradiation with gamma photons (RG6) emitted by ^{60}Co (1.25 MeV) source and after it's irradiation with 12 MeV energy electrons (RE6)
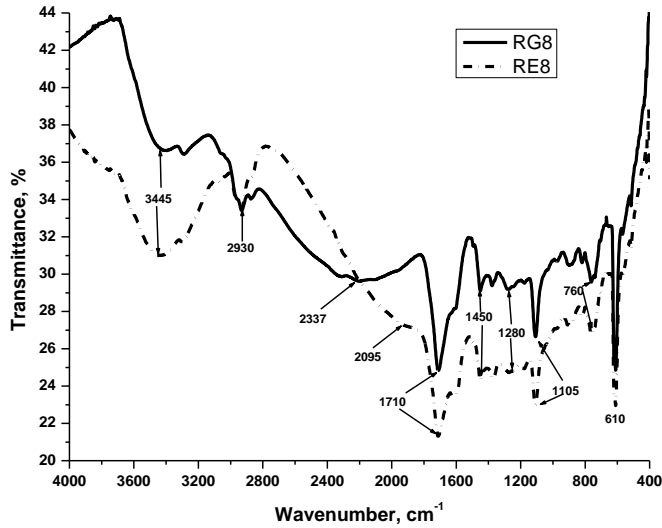
Fig. 3.13 FTIR transmittance spectra of RP8 coating after it's irradiation with gamma photons (RG8) emitted by ^{60}Co (1.25 MeV) source and after it's irradiation with 12 MeV energy electrons (RE8)

Rearrangements in chemical bonding structure after the irradiation correlate with the radiation induced changes of the morphological properties of the irradiated coatings. The surface morphology of experimental coatings was examined using atomic force microscopy (AFM, NT−206) with V−shaped ULTRASHARP Si cantilever and the roughness values were determined. 3−D topographic scans of the coatings before and after their modification by 12 MeV electron beam are provided in Fig. 3.14, Fig. 3.15 and Fig. 3.16. Each scan represents 10 μm × 10 μm lateral areas.
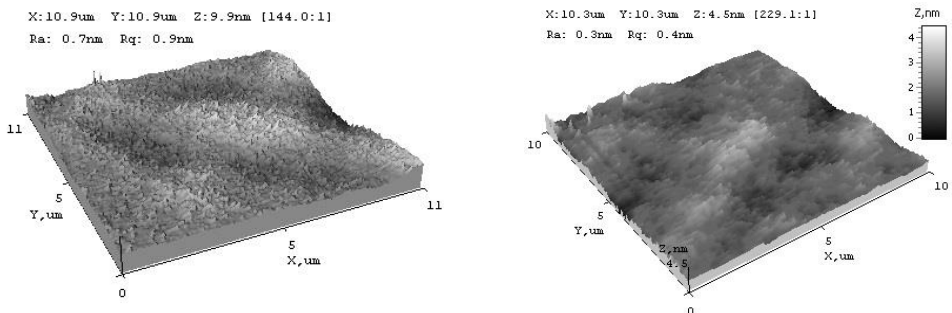
Fig. 3.14 Three dimensional AFM images of as prepared RP4 coating and of irradiated RE4 coating

As it was mentioned above and considering the estimated refractive index values all experimental coatings were identified as amorphous

93

hydrogenated/polymer like carbon coatings. Well pronounced polymer like coating structure with a surface roughness $R_q = 0.9$ nm was observed at 100V bias (RP4). After the modification with high energy electrons the coating's (RE4) surface became smoother whereas the surface roughness of coating decreases to $R_q = 0.4$ nm (Fig. 3.14).
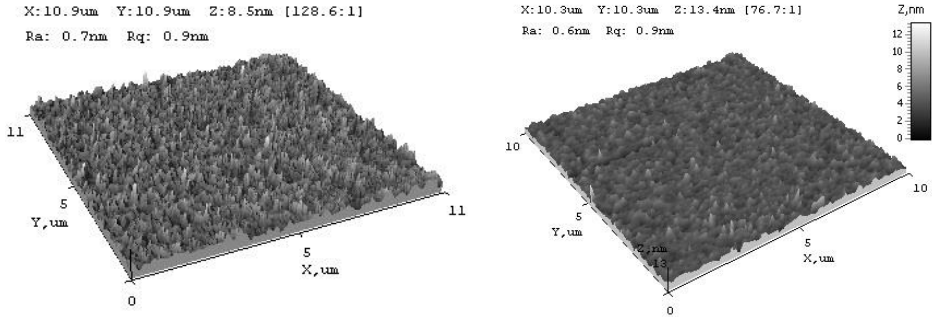
Fig. 3.15 Three dimensional AFM images of as prepared RP6 coating and of irradiated RE6 coating

The increase of bias voltage till 200 V (RP6) lead to formation of some graphite clusters within polymer matrix of PLC coating. Surface structure of the RP6 coating (Fig. 3.15) was more uniform as compared to coatings produced at lower bias, however surface roughness remained the same $R_q = 0.9$ nm. Due to rearrangements in the structure of the coating dependent on the electron beam energy and transferred dose the surface of irradiated coating (RE6) become smoother, however the surface roughness changed insignificant – $R_q = 0.8$ nm.
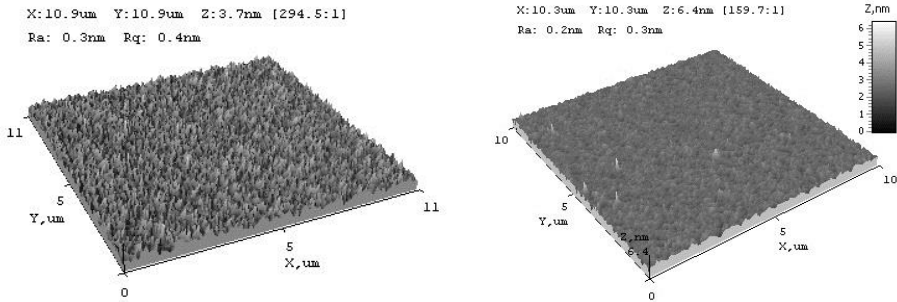
Fig. 3.16 Three dimensional AFM images of as prepared RP8 coating and of irradiated RE8 coating

Increasing the bias voltage up to ≥ 300 V the surface morphology of RP8 coating (Fig. 3.16) becomes smoother $R_q = 0.4$ nm as compared to coatings deposited in lower bias voltage. The same process is observed after the irradiation of experimental coatings with high energy electrons. The roughness of RE8 coating decreased to $R_q = 0.3$ nm.

94

The results support the assumption that the graphite clusters form in a polymeric matrix, which is associated with the internal restructuration of carbon coatings.

3.1.2. Carbon coatings fabricated at different temperatures

Carbon coatings were synthesized by PECVD method in RF (13.56 MHz) dual-plasma reactor on *n* type silicon (100) substrates. Prior to the deposition silicon substrates were cleaned and etched in acetone. The pre-cleaned substrates were pre-treated in Ar^+ plasma in order to achieve an oxygen free surface and a buffer layer and to enhance coating adhesion. Deposition of carbon coatings was performed at different temperatures ranging from 298 K to 673 K using acetylene (C_2H_2) as a precursor. Deposition time of PLC coatings was 300 seconds. Deposition pressure of 33 Pa was kept during entire deposition process.

Experimental coatings were prepared for the exploration. Index TA was assigned to the "as prepared" coatings, TE – to the electron beam irradiated coatings. Concerning the radiation impact on amorphous/polymeric structures experimental coatings were irradiated to high energy (6 MeV) electrons generated in medical linear accelerator Clinac 2100C (VARIAN) at the dose rate of 3 Gy/min. Maximal irradiation dose was 3 Gy.

The summary of the main characteristics of as-prepared experimental coatings obtained from ellipsometric measurements is provided in Table 3.7.

Table 3.7 The characteristics of polymer like a-C:H coatings

ID No	Precursor gas	Bias voltage, V	Deposition temperature, K	Refractive index	Extinction coefficient	Film thickness, nm
TA4	Acetylene C_2H_2	200	298	1.73	0.001	274
TA5			405	1.69	0.008	268
TA3			481	1.66	0.012	251
TA6			575	1.65	0.009	221
TA7			673	1.62	0.018	130

Ellipsometric results showed decreasing tendency of the thickness of the coatings and decreasing tendency of refractive index while the temperature was increasing. There was no well-established tendency observed between extinction coefficient and temperature. Investigated parameters strongly depend on the formed carbon coating structure and hydrogen content in it, as it was shown analyzing Raman spectra of experimental coatings.

Raman spectra of experimental coatings were obtained in the range of 1100 – 1800 cm^{-1}. The *D* and *G* bands were fitted simultaneously with multi-Gaussian contours at a linear background. *G* position was chosen as the maximum of the function rather than its center, to allow comparison with symmetric curve fits. The main role defining type of carbon coating play the *G* peak at 1500 – 1630 cm^{-1}

which arises from the bond stretching motion of pairs of sp^2 C atoms in aromatic rings or olefinic chains (Ferrary and Robertson, 2000; Rodil et al., 2001), and the D peak, which becomes active only in the presence of disorder is due to the breathing modes of rings. The full width at half-maxima (*FWHM*) of D and G peaks as well as the integral intensity ratio between D and G peaks (I_D/I_G) was estimated. All results are provided in Table 3.8 and Table 3.9.

Table 3.8 The main results of Raman spectroscopy of as prepared coatings

ID No	Deposition temperature, K	Characteristics of Raman spectra of as prepared coatings					
		D, cm^{-1}	$FWHM_D$, cm^{-1}	G, cm^{-1}	$FWHM_G$, cm^{-1}	T, cm^{-1}	I_D/I_G
TA4	298	1359	80	1573	150	1178	0.64
TA5	405	1352	120	1557	230	1171	0.57
TA3	481	1339	160	1532	210	1135	0.59
TA6	575	1363	60	1579	130	1180	0.62
TA7	673	1353	110	1581	200	1167	0.53

Analysis of Raman spectra has shown that the wave numbers corresponding to the D peak of experimental coatings varied in the range from 1339 cm^{-1} to 1363 cm^{-1}, whereas the G peak – from 1532 cm^{-1} to 1581 cm^{-1}. Intrinsic peak varied in a range 1135 cm^{-1} to 1180 cm^{-1} was observed for all experimental coatings. This peak is called T peak characterized as v_1 mode, also this peak called trans-poliacetylene peak. This peak could be related to the formation of nanocrystalline clusters however, it is not characterized as sp^3 phase bonds.

Table 3.9 The main results of Raman spectroscopy of irradiated coatings

ID No	Deposition temperature, K	Characteristics of Raman spectra of irradiated coatings					
		D, cm^{-1}	$FWHM_D$, cm^{-1}	G, cm^{-1}	$FWHM_G$, cm^{-1}	T, cm^{-1}	I_D/I_G
TE4	298	-	-	-	-	-	-
TE5	405	1358	80	1592	200	1179	0.59
TE3	481	1392	100	1568	150	1188	0.63
TE6	575	1363	80	1589	200	1191	0.71
TE7	673	-	-	-	-	-	-

The Raman spectra of experimental coatings are presented in Fig. 3.17, Fig. 3.18 and Fig. 3.19.

Fig. 3.17 shows the as prepared (TA3) and irradiated with high energy electrons (TE3) Raman spectra of coatings deposited at 481 K temperature. The D peak centered at around 1339 cm^{-1}, G peak located at around 1532 cm^{-1} and T peak was observed at 1135 cm^{-1}. After irradiation the D peak gradually grows and its height is less than that of G peak, whereas Raman line shapes have a slight skewed for D and G peak and shift higher peak position. It should be noted that the T peak intensity decreased after the irradiation with high energy electrons and its position has changed. The G peak position shifts from 1532 cm^{-1} (as prepared) to 1568 cm^{-1} (irradiated) as well as $FWHM_G$ of G peak decreases from 210 cm^{-1} to 150 cm^{-1},

respectively. The same trend is observed in the D peak position shift. The D peak position shifts from 1339 cm^{-1} (as prepared) to 1392 cm^{-1} (irradiated) and the $FWHM_D$ of D peak decreases from 160 cm^{-1} to 100 cm^{-1}, respectively. Equally the T peak position shifts from 1135 cm^{-1} (as prepared) to 1188 cm^{-1} (irradiated). The relative ratio of the D peak to G (I_D/I_G) is 0.59 (for as prepared coating) increases up to 0.63 (for the irradiated coating). The positions of D and G bands compared to typical D and G peaks of the polymer like a-C:H films are shifted to the higher frequencies. According to Marcinauskas et al. (2007) and Robertson (2002) it is related with reduction of bond angle disorder and growth of graphite domains. Whereas increasing tendency of I_D/I_G ratio and of $FWHM$ of both peaks means that coating starts to increase its disorder performance due to slight graphitization and losing the hydrogen as a result in the graphitization conversion for C–C sp^3 bonded carbon to transform to C=C sp^2 bonded carbon (Tai et al., 2006). The intensity of D peak increases because of conversion of sp^3 bonds to sp^2 bonds, desorption of hydrogen and conversion of carbon structure to nanocrystalline graphite (Chu and Li, 2006).
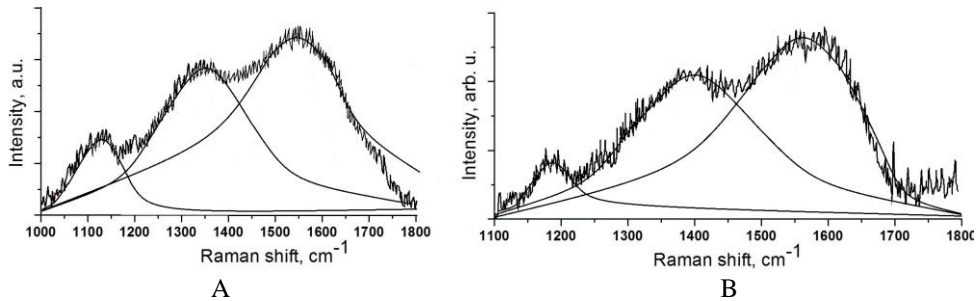
Fig. 3.17 Raman spectra of experimental coatings deposited at 481 K temperature: A – as prepared (TA3), B – irradiated with high energy (12 MeV) electrons (TE3)

It is evident that RS of experimental coatings (Fig. 3.18) contain some additional intrinsic peaks indicating more complicated structure of carbon coatings. The main Raman peaks of TA5 coating (Fig. 3.18 A) were obtained at 1352 cm^{-1} (D peak), at 1557 cm^{-1} (G peak) and at 1171 cm^{-1} (T peak). All peaks change their shape, intensity and position after irradiation with high energy electrons. The D and G peaks shifted to the higher wave number to 1358 cm^{-1} and 1592 cm^{-1}, respectively. Investigation of T peak shape and position after the irradiation has shown that peak intensity decreased and position shifted to higher wave number accordingly to 1179 cm^{-1}. The full width at half-maxima ($FWHM$) of D and G peaks is narrowed after the modification from 120 cm^{-1} to 70 cm^{-1} (D peak) and from 230 cm^{-1} to 180 cm^{-1} (G peak), respectively. The integral intensity ratio I_D/I_G increases from 0.57 to 0.59. According to Casiraghi et al. (2007) there may be some reasons for the shape of the spectrum and narrow $FWHM$ values: changes of bonding structure in the irradiated coating (increased number of sp^2 sites), radiation induced stress and formation of

clusters in the experimental coating, their size and distribution. In parallel, the intrinsic peak is observed in experimental coating TE5 (Fig. 3.18 B): the peak at about 1275 cm^{-1} can be assigned to C–O–C asymmetric stretch as polymerization product for experimental coating.
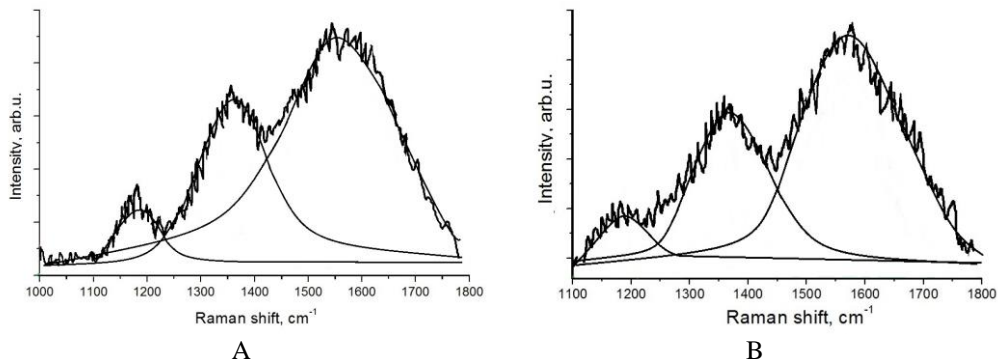
Fig. 3.18 Raman spectra of experimental coatings deposited at 405 K temperature: A – as prepared (TA5), B – irradiated with high energy electrons (TE5)

Analysis of Raman spectra has shown the similar tendency for Raman peak shifting for TA6 coating (Fig. 3.19 A); however the overall relative intensity of irradiated coating was lower.
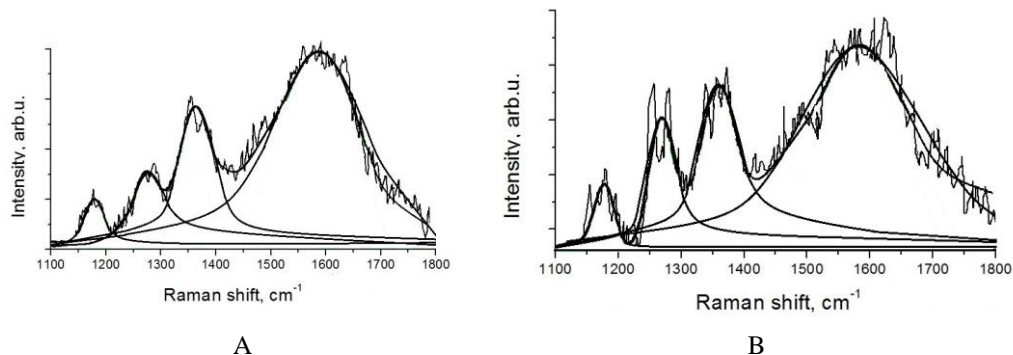
Fig. 3.19 Raman spectra of experimental coatings deposited at 575 K temperature: A – as prepared (TA6), B – irradiated with high energy electrons (TE6)

After irradiation D peak remains at the same position - 1363 cm^{-1}, however the intensity of this peak slightly increases. The increased intensity of D peak might be explained by the conversion of sp^3 bonds to sp^2 bonds, desorption of hydrogen due to radiation induced scission and crosslinking processes in polymeric structure. G peak of irradiated TE6 coating (Fig. 3.19 B) shifts from 1579 cm^{-1} to 1589 cm^{-1} and becomes broader. It is to point out that the *FWHM* values of the both peaks are higher after the irradiation and the I_D/I_G ratio increases from 0.62 to 0.71. Therefore,

98

it is possible to suggest that this coating became more polymer-like after its irradiation with high energy electrons. The intrinsic peak is observed at about 1275 cm^{-1} that can be assigned to C–O–C asymmetric stretch.

The surface conditions play an important role applying PLC as protective coatings. Due to this surface morphology of experimental coatings was examined using atomic force microscopy (AFM, NT-206) with V-shaped ULTRASHARP Si cantilever and the roughness values were determined. 3-D topographic scan of the coatings before and after their modification by 6MeV electron beam are provided in Fig. 3.20 and Fig. 3.21. Each scan represents 3 μm × 3 μm lateral areas.

As it was mentioned above and considering the estimated refractive index values all experimental coatings were identified as polymer like amorphous hydrogenated carbon coatings. Well pronounced polymer like coating structure with a surface roughness $R_q = 0.8$ nm was observed at 405 K temperature (TA5). After the modification with high energy electrons the coating's (TE5) surface became smoother whereas the surface roughness of coating decreases to $R_q = 0.7$ nm (Fig. 3.20).
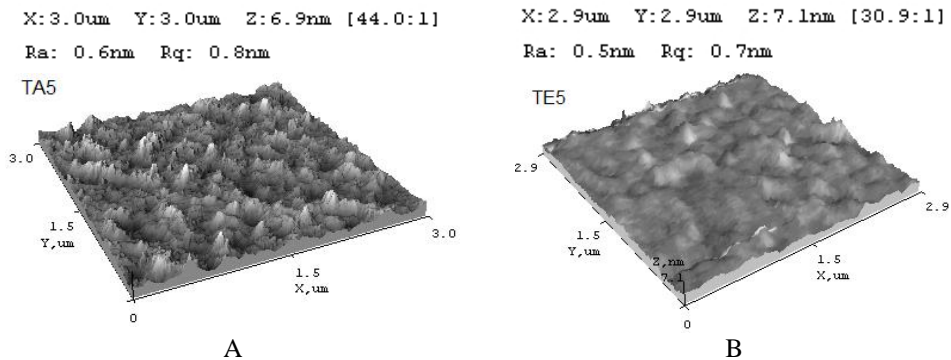
                              A   B
Fig. 3.20 Three dimensional AFM images: A – as prepared coating TA5, B – irradiated coating TE5

Increasing the temperature up to 575 K the surface morphology of TA6 coating (Fig. 3.21 A) becomes smoother $R_q = 0.4$ nm as compared to coatings deposited in lower temperature. The same process is observed after the irradiation of experimental coatings with high energy electrons. Due to rearrangements in the structure of the coating dependent on the electron beam energy and transferred dose the surface of irradiated coating (TE6) become smoother, however the surface roughness changed insignificant. The roughness of TE6 coating (Fig. 3.21 B) decreased to $R_q = 0.3$ nm.
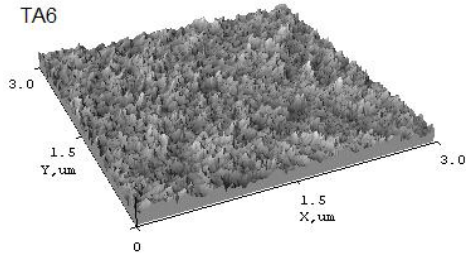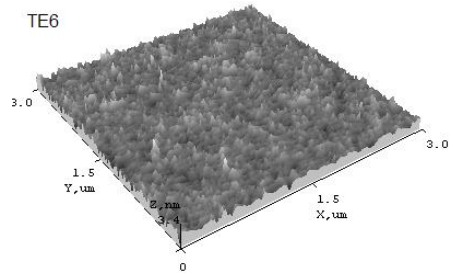
Fig. 3.21 Three dimensional AFM images: A – as prepared coating TA6, B – irradiated coating TE6

It is evident that the structure of carbon coating produced at higher temperatures (575 K for TA-6) is more polymer-like and smoother as compared to coatings produced at lower temperatures (405 K for TA-5). With reference to other publications electron bombardment of coatings is responsible for hydrogen evaporation (Plaipaite-Nalivaiko et al., 2013) and radiation induced polymerization processes (Novikov et al., 1997). Surface confined polymerization can significantly change surface morphology and smoother rough surfaces as it is observed in the case of irradiated coatings. It should be noted that the surface roughness of irradiated coatings decreases corresponding to rearrangements in the structure of the coatings that in turn are dependent on the electron beam energy and transferred dose.

Summary

All prepared experimental coatings were investigated and analyzed. It was found that variations of bias voltage and temperature had significant influence on the properties of modified coatings. Investigations have shown that the experimental coatings can be attributed to polymer like amorphous hydrogenated carbon films.

Increasing the bias, the refractive index is increasing too, while the optical band gap is narrowing. Coatings formed at higher bias are harder. Upon the high energy electron and photon irradiation, the bonds between hydrogen and carbon atoms are terminated, therefore the restructuration processes and sp^2 hybridization carbon cluster formation proceed. Due to structural changes in the irradiated coatings the optical transparency reduces in visible light range, the coating becomes harder.

Coatings formed at different temperatures are polymer like a-C:H carbon coatings. Irradiation of coatings formed at temperatures higher than 200 °C with high energy electrons leads to the hydrogen release from coatings, the restructurization, and changes of surface morphology. After modification with high energy electrons they reflected the increase of the bonding sp^2/sp^3 ratio, the

occurrence of enhanced clusterization and graphitization processes as well as changes in surface morphology.

3.2 Ag/polymer nanocomposites

3.2.1. Ag/PMMA nanocomposites

Poly-methyl methacrylate (PMMA) solution with metal powder (Ag) additives was prepared dissolving 0.001 M of $AgClO_4$ in 50 ml of 1% PMMA solution in chloroform. ~1 mm thin layers of polymeric structures were spin-coated on the surface of polished optical glass using "DYNAPERT PRECIMA" centrifuge. As prepared films were dried in the desiccator (air humidity ~ 30%). PMMA films without additives were also produced for the comparison.

Ag/PMMA nanocomposites were successfully synthesized by *in-situ* polymerization technique without using any external chemical reagent at ambient temperature. PMMA was acting as a protective agent that restricts the mobility of silver ions during the reaction, and hence, agglomeration was mostly controlled. Chloroform was used as a solvent to form chemical network between silver nanoparticles and PMMA. Synthesis of Ag nanoparticles was performed using photocatalytic reduction of silver atoms directly in a thin layer of deposited polymer. UV light source was used for this purpose. Applied UV exposure time of 5 min. was sufficient enough for photoreduction of Ag ions and formation of silver nanoparticles.

UV irradiation is a widely used technique to produce electrons in the corresponding solution for reduction of metal salts is used for the synthesis of nanoparticles. Within polymer matrix produced electrons reduce metal ions into metal atoms (in present case $- Ag^+$ and Ag^0 correspondingly). In accordance with (Eqs. (3.7) and (3.8)), metal atoms Ag^0 formed in solution from the Ag^+ reductions tend to associate with other ions and can grow into oligomers and larger clusters (Eq. (3.9)) (Jurasekova et al., 2011; Calinescu et al., 2014).

$$Ag^+ + e_{aq}^- \rightarrow Ag^0; \tag{3.7}$$

$$Ag^+ + {}^\bullet H \rightarrow Ag^0 + H^+; \tag{3.8}$$

$$Ag^0 + Ag^+ \rightarrow Ag_2^+ \Rightarrow Ag_{m+x}^{x+}; \tag{3.9}$$

$$Ag^0 + Ag^0 \rightarrow Ag_2 \Rightarrow Ag_n; \tag{3.10}$$
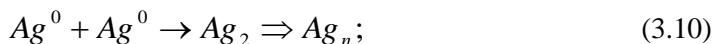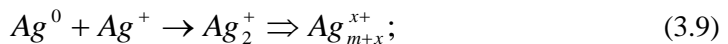
Moreover, silver atoms Ag^0 can condensate, forming neutral nuclei Ag_n (Eq. (3.10)), which can grow by reducing more silver ions, giving rise to large silver nanoparticles $(Ag)_L$ (Eqs. (3.11) and (3.12))

$$Ag_n + nAg^+ \rightarrow (Ag)_L; \tag{3.11}$$

$$Ag_n + Ag_m \rightarrow Ag_{n*m}; \tag{3.12}$$
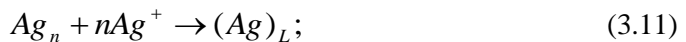
The produced silver atoms nucleate and grow into silver nanoparticles inside the polymer matrix as it is shown in Fig. 3.22 which was redrawn from (Yilmaz, 2011).
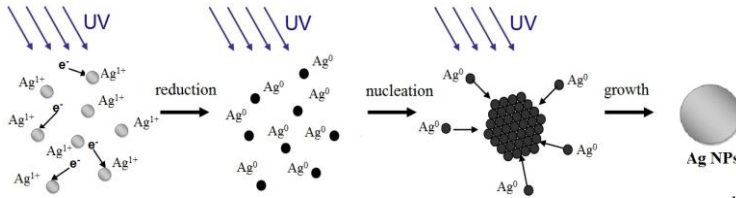
Fig. 3.22 Schematic representation UV radiation induced reduction of Ag^{1+} ions to Ag^{0} atoms and nucleation and growth of Ag nanoparticles in polymer matrix

During the UV irradiation of the polymer, cross-linking process prevails upon polymer scission limiting the growth of the nanoparticles after a critical particle size is reached. The *in-situ* reduction method doesn't destroy the polymer completely, only a very small part of the polymer is degraded (Fig. 3.23) (Puišo et al., 2013; Singho et al., 2014; Vodnik et al., 2009).
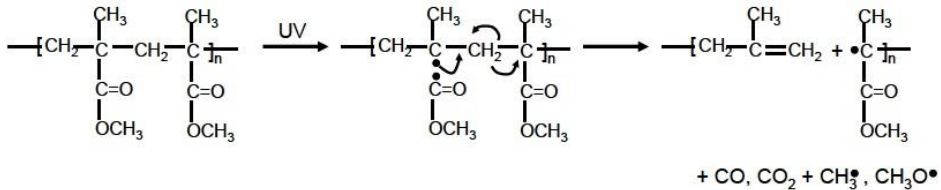
Fig. 3.23 UV radiation to PMMA (Singho et al., 2014)

Experimental films were irradiated to different doses from 0.02 Gy to 0.20 Gy at dose rate of 3.5 mGy/min using 35 keV X-ray photons generated in X-ray diffractometer DRON-3. The radiolysis of monomer solution results in the formation of radicals, which then initiate the polymerization of MMA to form polymer chains. The dispersed silver ions are reduced to silver atoms by reductive particles and sustain further growing to larger clusters leading to the formation of silver nanoparticles (Vodnik et al., 2009). Due to quick polymerization of MMA the ductility of the reaction system, resulting the formation of polymer chains, increases. This effect as well as the availability of carboxylate functional groups of PMMA with a high affinity for the Ag^{+} can limit the aggregation of silver nanoparticles and make them dispersed in polymer matrix homogeneously (Akhavan et al., 2010).

$$H_2O \xrightarrow{\text{gamma ray}} e_{aq}^- + H^{\cdot} + OH^{\cdot} + H_3O^+ + H_2 + \cdots$$

$$OH^{\cdot} + CH_3\underset{\overset{|}{OH}}{C}HCH_3 \longrightarrow CH_3\underset{\overset{|}{OH}}{\overset{\cdot}{C}}CH_3 + H_2O$$

$$Ag^+ + e_{aq}^- \longrightarrow Ag^0$$

$$Ag^+ + CH_3\underset{\overset{|}{OH}}{\overset{\cdot}{C}}CH_3 \longrightarrow CH_3\underset{\overset{\|}{O}}{C}CH_3 + Ag^0 + H^+$$

$$nAg^0 \longrightarrow Ag_2 \longrightarrow Ag_n \longrightarrow AgNPs$$

Fig. 3.24 The mechanism of formation of Ag/PMMA nanocomposite proposed by (Akhavan et al., 2010)

Nanocomponents were made from precursors in the liquid phase employing chemical and physical processes that initiate building of nanofeatured blocks within the final host material structure. Two types of host materials for Ag NPs were explored. NPs production within polymer resulted in formation of polymeric nanocomposite Ag/PMMA. Photoreduction and radiation enhanced synthesis processes were applied to produce Ag nanoparticles and other nanoderivatives in this work.

Optical properties of Ag/PMMA nanocomposites before and after X-ray irradiation were analyzed using Avantes UV/VIS/NIR Avaspec – 2048 spectrometer operating in the wavelength range of 200 nm – 700 nm.

The size of synthesized nanoparticles plays an important role in the setting of the absorption spectrum in UV-VIS range, since metal nanoparticles have very specific absorption peaks in the visible region, so called surface plasmon resonance (SPR) band. UV-VIS absorption spectra are quite sensitive to the formation of Ag NPs because the position of the SPR peak depends on their particle diameters and shapes (Khan et al., 2011).

UV-VIS absorption spectra of the pure PMMA and Ag/PMMA were obtained (Fig. 3.25). In comparison to pure PMMA, the Ag/PMMA composite shows an absorption band at about 397 nm, which is in good agreement with the results of other authors establishing SPR peak of silver nanoparticles (Deng et al., 2008; Jurasekova et al., 2011; Singho et al., 2014).

Small peak observed at 397 nm in absorbance spectrum of initial Ag/PMMA composite indicates that a number of Ag nanoparticles are already present in the polymer composite since they were synthesized during UV preirradiation of films. Presence of Ag nanoparticles contributes to the increased transparency of nanocomposites as compared to the PMMA. Irradiation of experimental films with X-rays shows deterioration of PMMA optical properties due to the degradation of polymer caused by scission of its main chain upon irradiation.
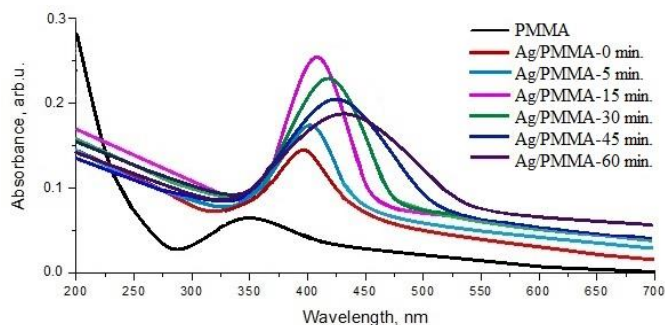
Fig. 3.25 UV-VIS absorbance spectra of pure PMMA and Ag/PMMA after irradiation with photons at low dose rate

Taking into account that the silver ions can also be reduced by the radicals produced by the degradation of the polymer and that further formation of silver nanoparticles within the polymer matrix is possible, more detailed analysis of absorption spectra of irradiated nanocomposites was performed. Growing SPR peak intensity after UV irradiation followed by photon irradiation indicated intensive formation of silver nanoparticles. Photon irradiation induced red-shift of SPR peak from 397 nm in initial Ag/PMMA composite towards higher wavelength to 436 nm and broadening of SPR peaks. Redshift of SPR peak of metallic particles indicates an increase of metal particle size or formation of the Ag nanoclusters.

This is valid also taking into account the electron mean free path effect, according to which the intensity of the SPR band should be higher for bigger particles while the critical size of the surface plasmon mode will be broadened. This is related to the energy transfer from the plasmon to single electron excitation between the quantized levels or to energy dissipation due to inelastic scattering of the transferred electrons, and leads to the strength reduction increasing the size of the metal particles. It should be noted that the exact position and broadening of SPR peak dependent on such parameters as shape of the particle, surface quality, size, and structure. Since SPR peak was observed in the range of 397 – 436 nm it was assumed that Ag particles have spherical shape (Petryayeva et al., 2011).

Investigation of the optical properties of polymer composites was obtained employing optical microscope (Optika B-600 MET). It has shown that silver nanoparticles were successfully doped in the PMMA matrix. The size of synthesized Ag particles was X-ray dose dependent, however not only the formation of particles

104

but polymer chain scission was the main process contributing to the deterioration of the nanocomposite's optical properties. This suggestion was supported by the results of surface morphology examinations. Surface morphology of experimental polymer films before and after their exposure to soft X-rays is shown in Fig. 3.26.

A   B   C
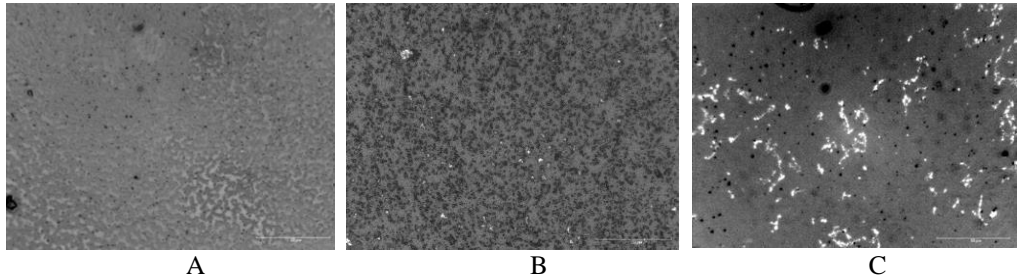
Fig. 3.26 Surface morphology of experimental films before their irradiation: A - PMMA, B - Ag/PMMA; and after irradiation to 2Gy: C - Ag/PMMA

It is clearly seen that distributed number of Ag particles is present in the PMMA matrix after its exposure to UV light (Fig. 3.26 B). However, X-ray irradiation of the experimental films to doses up to 2 Gy, degradation of PMMA surface and agglomeration of Ag particles to clusters in PMMA matrix (Fig. 3.26 C) was observed. More detailed information of surface morphology and bulk composition were investigated in a scanning electron microscope (JSM–5610 LV) with attached energy dispersive X-ray analysis (EDX JED-2201; JEOL, Japan)

As it was determined by microscopy measurements, that number of distributed Ag particles is present in the PMMA matrix after its exposure to UV light (Fig. 3.27). In Fig. 3.27 A, B, C small clusters are visible. The Ag nanoparticles tend to stick and form agglomerates due to their high surface energy. It is seen that the size of the Ag clusters vary in a wide range. This can explain the broad UV–VIS absorption peak in the absorption spectra of the composite (Fig. 3.25, red curve). All SEM photographs were enlarged 2000, 5000 and 10000 times.

A   B
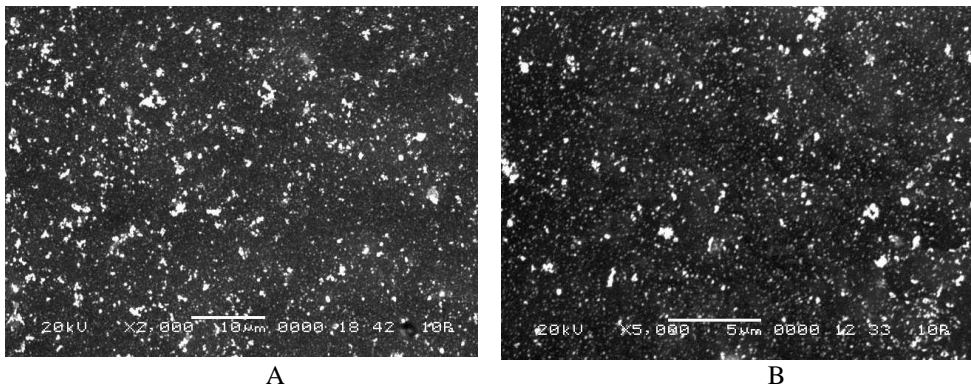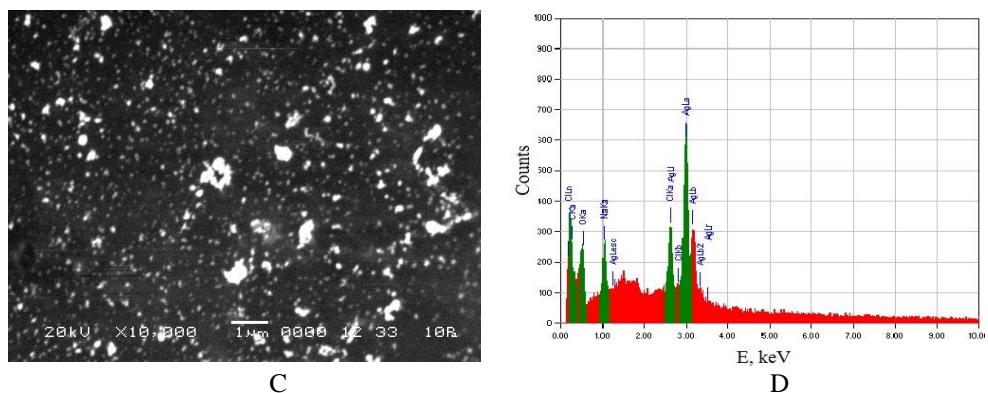
Fig. 3.27 SEM images and EDX spectra after films' irradiation to UV light

Analysis through energy dispersive X-ray (EDX) spectrometer confirmed the presence of elemental silver in Ag/PMMA composites (Fig. 3.27 D). The vertical axis displays the number of X-ray counts while the horizontal axis displays energy in keV. Identification lines for the major emission energies for silver (Ag) are displayed and these correspond with peaks in the spectrum, thus giving confidence that silver has been correctly identified. The chemical composition of Ag/PMMA nanocomposite is provided in Table 3.10.

Table 3.10 Chemical composition of Ag/PMMA composite

Element	E, keV	Mass, %	Error, %	At, %	Mass, % K
C K	0.277	1.32	0.38	3.69	0.5810
O K	0.525	31.78	1.51	66.72	17.7959
Na K	1.041	4.38	0.61	6.39	2.8748
Si K	1.739	0.18	0.27	0.21	0.1640
Cl K	2.621	5.63	0.20	5.34	8.7529
Ag L	2.983	56.71	0.64	17.66	65.8313
Total		100.00		100.00	100.00

The SEM images of experimental film after its exposure to X-rays for 5 min. (0.2 Gy) are provided in Fig. 3.28.

The silver nanoparticles formed were predominantly spherical with uniform shape. It is known that the shape of metal nanoparticles considerably change their optical and electronic properties (Casiraghi et al., 2007). The elemental mapping analysis for a selected region (SEM Fig. 3.28 B) clearly showed that silver (green, blue and pink) is homogeneously distributed throughout the surface (Fig. 3.28 D).

106

A

B

C

D
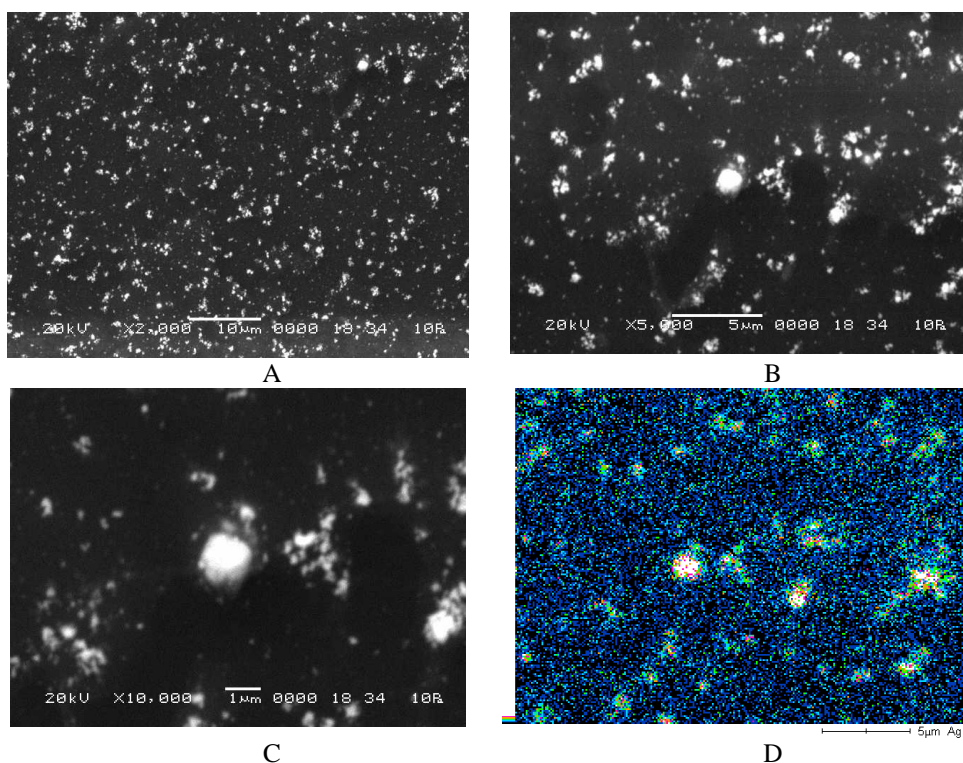
Fig. 3.28 SEM images and EDX map after film's irradiation to X-rays (0.2 Gy)

Fig. 3.29 shows SEM images of the Ag/PMMA composite after its exposure to X-rays for 30 min. (1 Gy) The surface is characterized by regions of relatively homogeneous particle deposition (Fig. 3.29 A), but also by the presence of large agglomerates (Fig. 3.29 B).

The EDX spectrum of chemical composition of the composite coating is provided in Fig. 3.29 C. Clearly expressed Ag peak indicates formation of metal NPs that agglomerate to clusters. The elemental mapping analysis (Fig. 3.29 D) for a selected region (SEM Fig. 3.29 B) clearly showed that silver is homogeneously distributed throughout the surface in addition to other major elements, *i.e.*, C, O and Cl. The absence of any other peaks clearly indicates that the synthesized substrate is in pure form, thus validating an efficient immobilization of Ag NPs.
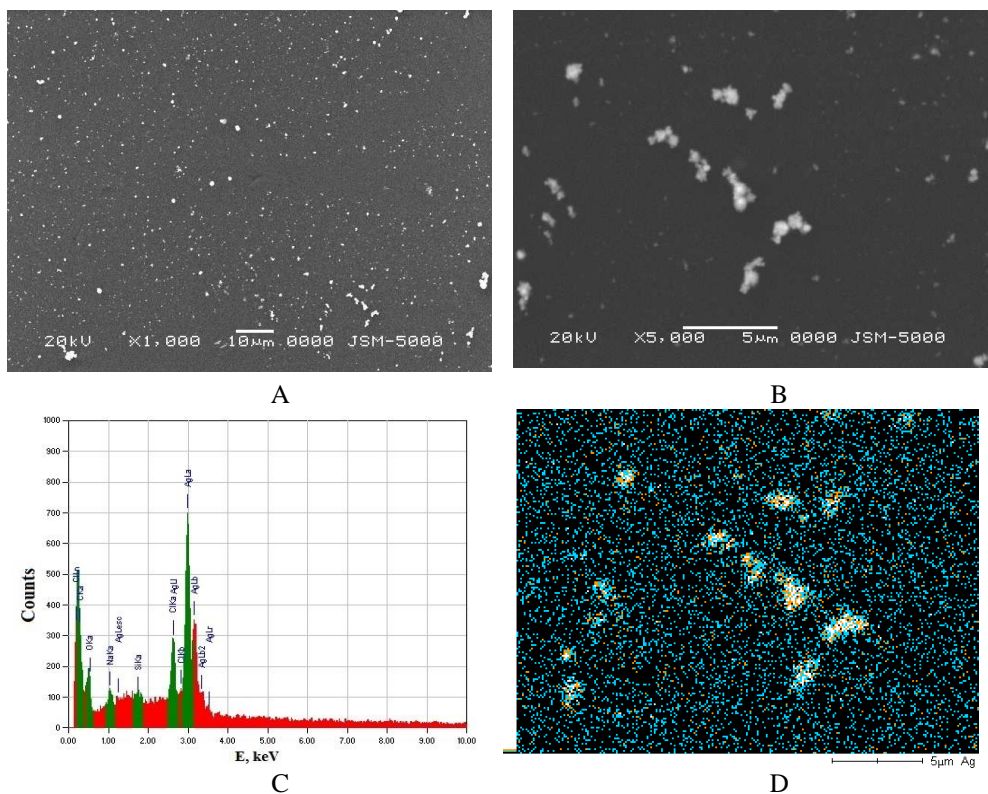
Fig. 3.29 SEM images, EDX spectra and map after film's irradiation to X-rays (1 Gy)

SEM and EDX images of Ag/PMMA composite exposure to X-rays for 45 min. (1.5 Gy) are provided below (Fig. 3.30). Analysis of the SEM images shows fairly uniform distribution of Ag NPs in the coating, while active Ag NPs agglomeration to the Ag clusters. It is clearly seen that Ag NPs of different shapes and size dispersed in coating. Analyzing EDX images, well-expressed Ag peak (~ 80 %) is shown as well as the formation of Ag NPs and their agglomeration to clusters.
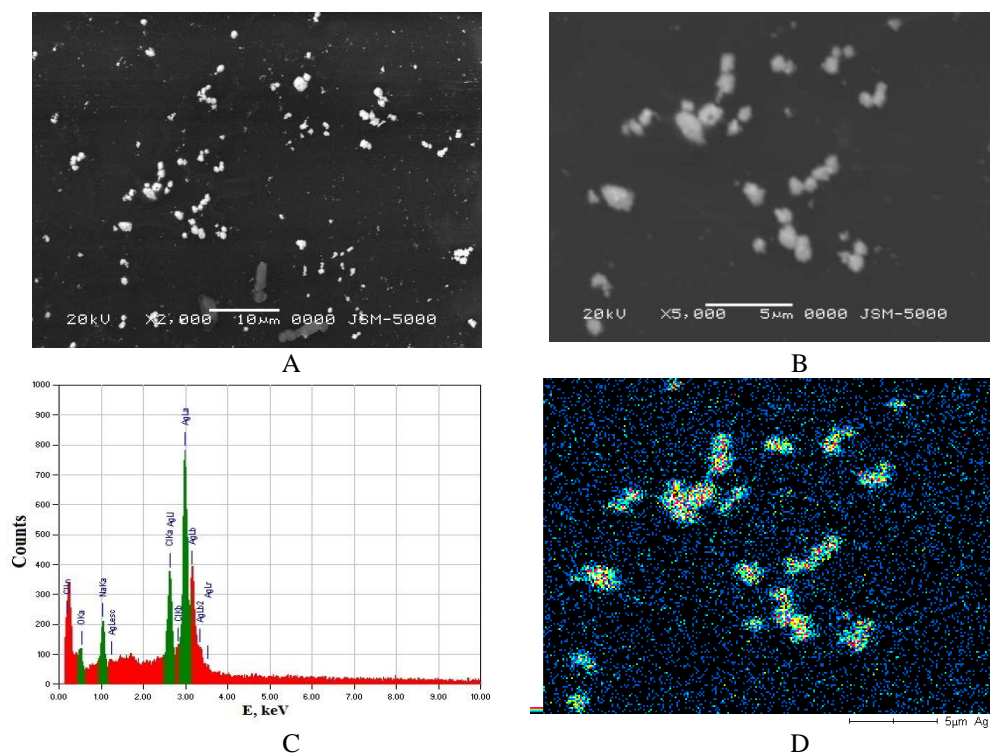
Fig. 3.30 SEM images, EDX spectra and map after film's irradiation to
X-rays (1.5 Gy)

Images of experimental films after their exposure to X-rays for 60 min. (2 Gy) are provided in Fig. 3.31. The SEM micrograph of Ag/PMMA composite indicates that Ag nanoparticles agglomerated and Ag clusters with mean size of 500 – 900 nm disperse in the PMMA matrix. This confirms that when reduction of silver ions and the polymerization of monomer take place simultaneously during irradiation, the silver nanoparticles are homogeneously dispersed in the polymer matrix. In addition, many nodular agglomerated grains (having diameter of 500 – 900 nm) that might form or are already forming Ag clusters are clearly seen in composite layer. It is supposed that a sufficiently uniform distribution of NPs and their agglomeration to some extent may contribute to the increased nanocomposite coatings hardness (Prosycevas et al., 2011). The EDX map of chemical composition of the composite coating is provided in Fig. 3.31 D.

A   B

C   D
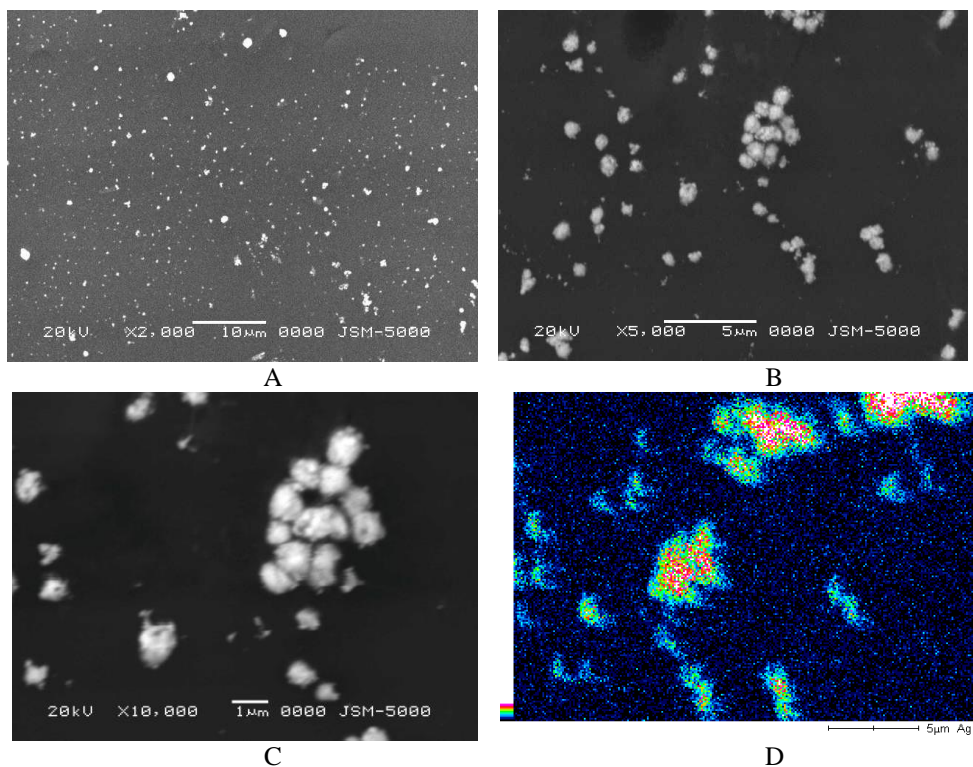
Fig3.31 SEM images and EDX map after film's irradiation to X-rays (2 Gy)

X-ray radiation induced changes in Ag/PMMA composites are linked to the reconfiguration of their bonding structure. The possible physicochemical interaction between the silver nanoparticles and PMMA was tested by Fourier transform infrared spectroscopy (FTIR, Bruker Vertex 70) in the wavenumber range from 400 cm^{-1} to 4000 cm^{-1}. Chemical bonding structure of experimental PMMA and nanocomposite (Ag/PMMA) films was investigated before and after their irradiation to the doses up to 2 Gy by means of infrared spectroscopy.

It is known that the shift of the peaks toward the lower wave numbers in the FTIR spectrum is an indicator of the chemical bonding of surfactant onto the nanoparticle surface (Hill and Whittaker, 2004). The FTIR spectra before and after irradiation of Ag/PMMA films to a certain doses are presented in Fig. 3.32.
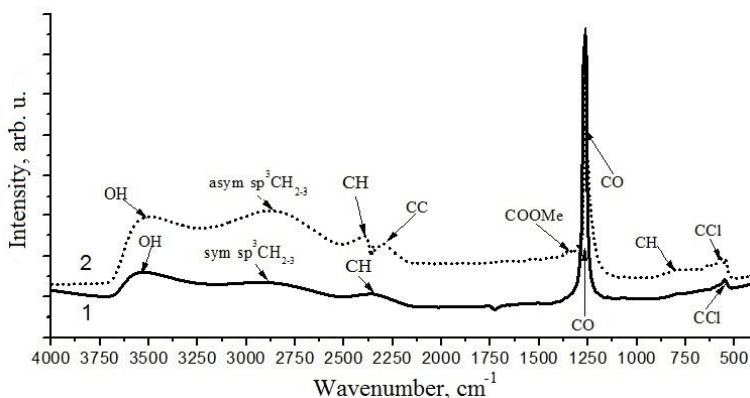
Fig. 3.32 FTIR spectra of Ag/PMMA films before (1) and after (2) their irradiation with X-rays (2 Gy)

The changes in the intensity and appeared peaks in the FTIR spectra of the investigated films after 60 min. (2 Gy) irradiation indicates that polymer chain reforms itself for the emerging groups and links. This process is part of radiation induced modification of composite structure and properties.

The FTIR spectra of polymeric nanocomposite (Ag/PMMA) films show sp^3 CH$_{2-3}$ (methylene) group in asymmetric stretching and bending mode at 2904 cm^{-1} which is shifted to lower wavelength at 2865 cm^{-1} for sp^3 CH$_{2-3}$ (methylene) group in symmetric stretching and bending modes after irradiation. It is clearly seen that radiation induces defects and dangling bonds that can be easily occupied by oxygen and create C=O and O–H bonds. Broad band ranging from 3300 cm^{-1} – 3700 cm^{-1} corresponds to the valence and deformation vibrations of O–H group. The C≡C absorption peak observed at 2342 cm^{-1} splits into two peaks. The peak at 2277 cm^{-1} corresponds to the C=C group and peak at 2386 cm^{-1} corresponds to the valence vibrations of C–H after irradiation of films with X-rays. The connecting bonding between PMMA and Ag through C=O influences the formation of silver nanoparticles and their size. Thus, PMMA acts as a surfactant and prevents the silver particle aggregation.

We assign intensive absorption peak observed at wave number 1269 cm^{-1} and after its modification with X-rays at 1250 cm^{-1}. The bands correspond to C–O–C of the methoxy group, and skeletal C–C in Ag/PMMA composites respectively. The scission process dominates here and due to this, the formation of Ag clusters could take place. This occurrence is observed by analyzing OM images after the modification of X-rays.

In the presence of Ag nanoparticles characteristic vibration bands at ~812 cm^{-1}, attributed to out-of-plane vibration of the C–H groups. Band at approximately 1080 cm^{-1} in Ag/PMMA composites is assigned to the sensitive metal complexes of methyl rocking vibrations coupled with a C–H vibration mode. Further, broad band from 750 – 550 cm^{-1} corresponds to the out of plane O–H vibration. Decrease in the

111

ratio of band intensities with the increase in the silver content indicates the interaction between the Ag nanoparticles and O–H groups.

3.3.2. Ag/PVP nanocomposites

Colloidal Ag/PVP solution was performed dissolving 1 g of poly (N-vinylpyrrolidone) (PVP) and 170 mg of silver nitrate (AgNO$_3$) in 4 ml and in 1 ml water, respectively. Ag$^+$ salt's solution was admixed to PVP solution. 100 μm of 20 % of sodium dodecyl sulfate (SDS, MW = 288.38) was dropped to Ag/PVP colloid as a surfactant.

Ag/PVP films were deposited on the silica substrates. Prior the deposition the substrates were sonically pre-treated in acetone for 10 min., chemically etched in the warm special chrome solution (K$_2$CrO$_7$ + H$_2$SO$_4$ + H$_2$O) for 10 min, and dried in the air stream. ~ 0.5 μm Ag/PVP films were spin-coated using "DYNAPERT PRECIMA" centrifuge from Ag/PVP colloidal solution on the pre-treated silica substrates at 1800 rpm for 60 s and dried in electrical oven at 100 °C for 10 min.

Ag/PVP nanocomposite films were obtained irradiating deposited Ag/PVP films by UV light source, applied UV exposure time of 5 min. and ^{60}Co isotope of gamma therapy unit "ROKUS-M" was used as a gamma irradiations source. Total irradiation dose varied in the range 2 – 50 Gy.

Formation of silver nanoparticles was performed by reduction reaction: $Ag^+ + PVP \rightarrow Ag(PVP)^+$. PVP was exploited to decrease the surface energy of metal nanoparticles and protect them from agglomeration. PVP in solution associates with the metal atoms, thus increasing the probability of nucleus formation (Ibrahim et al., 2009; Jovanovic et al., 2012). Differently, the N and O atoms of PVP polar group have a strong affinity for the silver ions and for metallic silver particles. It is known that the UV generated photoelectrons from PVP are the main reducers in Ag and PVP reaction (Zhao et al., 2013). According to Jurasekova et al. (2011) and Calinescu et al. (2014) silver salts reduction $Ag^+ \rightarrow Ag^0$ is induced also by the exited species of PVP. PVP is reducer and stabilizer in synthesis of Ag particles in Ag/PVP solution. PVP loses its stabilizer's function in Ag/PVP films due to the cross-linking and formation of 3D structures. Silver nanoparticles are growing up in irradiated Ag/PVP composites but their size is limited by the volume of 3D PVP structures, which varies with the UV irradiation.
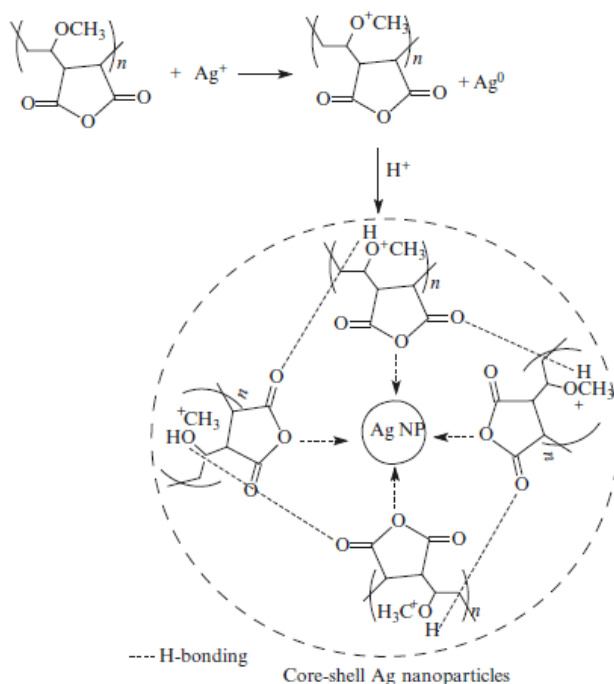
Fig. 3.33 Reduction of Ag$^+$ by CH$_3$O-groups of copolymer chain (Pomogailo et al., 2014)

It is assumed that metal ions bound in complex with a polymer chain are subjected to reduction, in this case, size of a nanoparticle is limited by space confined to local PVP chain containing metal ion (Fig. 3.34):
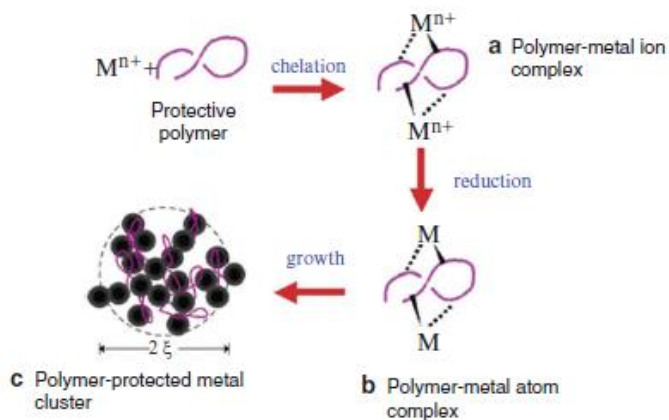
Fig 3.34 A route for the formation of the polymer–metal complex and nanocomposite (Pomogailo et al., 2014)

Comparison of the SPR peak positions of Ag/PVP colloidal solution (Fig. 3.35) was analyzed. It was found that the SPR peak position indicating SPR peak of silver nanoparticles. It is in a good agreement with the results of other authors. Whereas SPR peak of Ag/PVP colloidal solutions were observed at 420 nm, it could be suggested that spherical silver nanoparticles were formed in the solution. A small SPR peak appearing in 550 – 650 nm regions of the absorbance spectra after 6 days (Fig. 3.35 b) indicates ageing process of colloidal solution and corresponds to the formation of the larger particles. It might happen due to the etching of small particles and silver ions precipitation to the larger silver nanoparticles (Mikhlin et al., 2014).
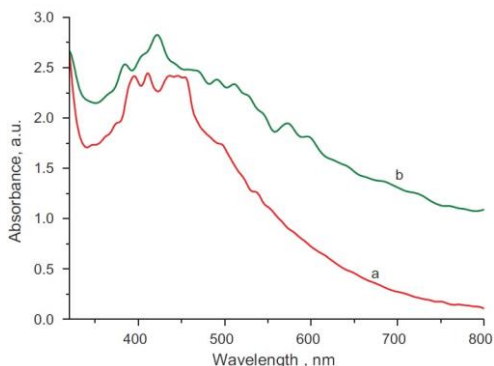
Fig. 3.35 UV–VIS absorbance spectra of Ag–PVP colloids: (a) 60 s min after mixing of components, and (b) after 6 days

The appearance of SPR peak indicates formation of nanoparticles in the film after 15 s of irradiation. The SPR peak position, intensity and half width varied with the irradiation time as it is shown in Fig. 3.36. Color of the films was dependent on the UV irradiation time and was changed from bright to dark yellow. Growing SPR peak intensity after short UV irradiation (up to 60 s) indicated intensive formation of silver nanoparticles. However after prolonged UV irradiation (up to 5 min) the SPR peak was shifted towards longer wavelength, its intensity was reduced and the peak became broader. According to Hutter and Fendler (2004) these changes are related to the silver particle growth and formation of different sized particles. Comparatively to the UV–VIS spectra of Ag/PVP colloidal solutions (Fig. 3.36) and Ag/PVP nanocomposite films (Fig. 3.36 A), it was indicated blue shift of SPR peak from 420 nm (colloids) to 406 nm (nanocomposite films after 30 s UV irradiation). It might be related to the PVP crosslinking induced by UV irradiation. Since SPR peak was observed in the range of 405 – 420 nm, it was assumed that Ag particles have spherical shape.
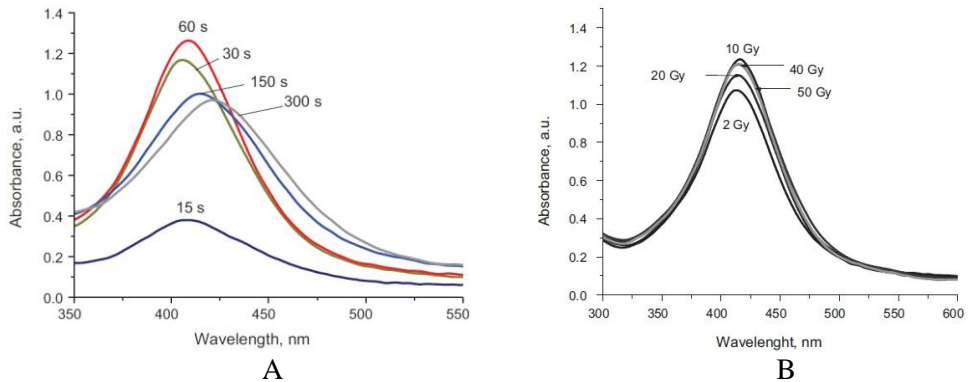
Fig. 3.36 A: Absorbance spectra of Ag/PVP films on silica substrate after UV irradiation. B: Absorbance spectra of Ag–PVP nanocomposite layer after low dose gamma irradiation

Low dose gamma irradiation (2 – 50 Gy) induced red-shift of SPR peak from 406 nm in initial Ag/PVP composites towards higher wavelengths in the UV–VIS spectra of gamma irradiated films, which indicates possible formation of spherical silver particles with an average size of ~ 38 nm. Measured UV–VIS absorbance spectra of all gamma irradiated Ag/PVP structures were very similar, SPR peak positions were almost the same and hesitated around 415 nm (Fig. 3.36 B).

Mie theory (Ghosh and Pal, 2007; Šileikaitė et al., 2009) was applied for the evaluation of silver particle size in Ag/PVP colloidal solution. Correlation between SPR peak position and particle's size experimentally established by Evanoff and Chumanov (2005) was used for the calculation of silver nanoparticles in PVP medium using experimental data, employing the calculation of silver nanoparticles in PMMA medium established by Evanoff and Chumanov (2005). It was found that the size of Ag particles in colloids and in short term irradiated Ag/PVP nanocomposites was approximately the same 32 nm. Particle size increased from 32 to 43 nm in long term (300 s) irradiated films.
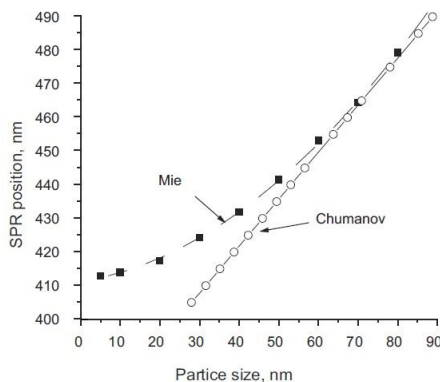
Fig. 3.37 Theoretical calculations of spherical Ag particle's size according to the SPR peak position in the UV–VIS spectrum

According to the obtained results, it could be suggested that low dose gamma irradiation initiate the growth of nanoparticles within PVP until the number of almost equal-sized particles saturated and stable nanostructure is formed. Long term (higher doses) gamma irradiation of nanocomposites was responsible for the rearrangements in polymer structure.

The morphology of the films and bulk composition were investigated using SEM with attached EDX. Distributed number of Ag particles is present in the PVP matrix after its exposure to UV light (Fig. 3.38). The silver nanoparticles formed were more or less spherical with uniform shape. Some of the Ag nanoparticles tend to stick and form agglomerates due to their high surface energy. Analysis through EDX shows well-expressed Ag peak (63.31%) that indicates formation of metal NPs and clusters.

A

B

C

D
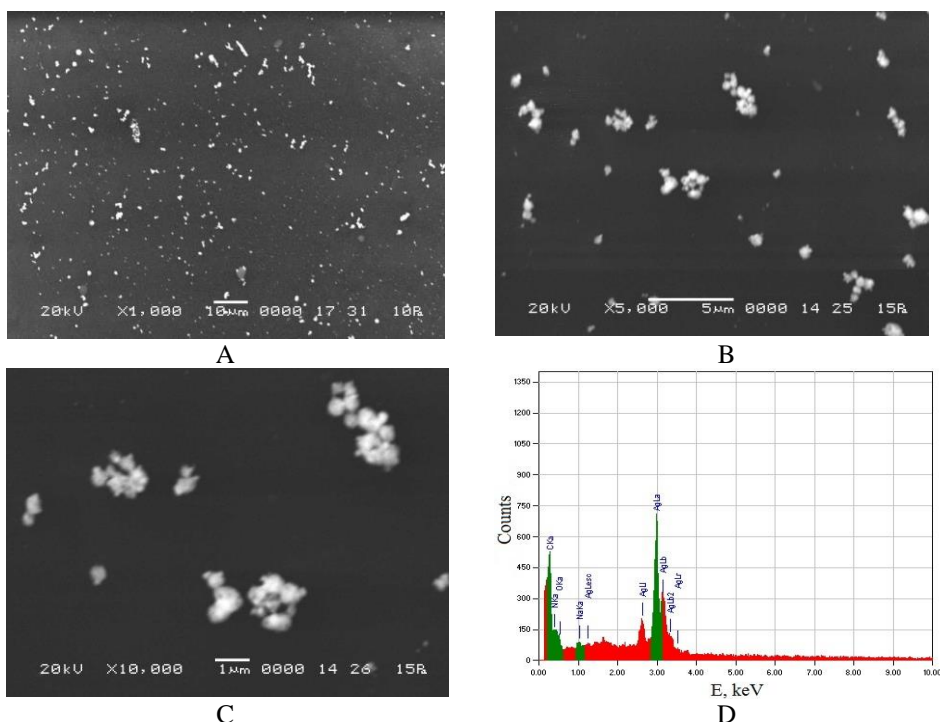
Fig. 3.38 SEM images and EDX spectra after film's irradiation to UV light

Experimental films after their exposure to gamma rays is provided in Fig. 3.39. The SEM images of Ag/PVP composite indicates the presence of silver in experimental films. The elemental mapping analysis (Fig. 3.39 D) for a selected region (SEM Fig. 3.39 B) clearly showed that silver (green, blue and pink) is homogeneously distributed throughout the surface in addition to other major elements, *i.e.*, C, O and Cl. The estimation of the surface composition indicated that nearly 69 mass % of the surface is occupied by elemental silver.

116
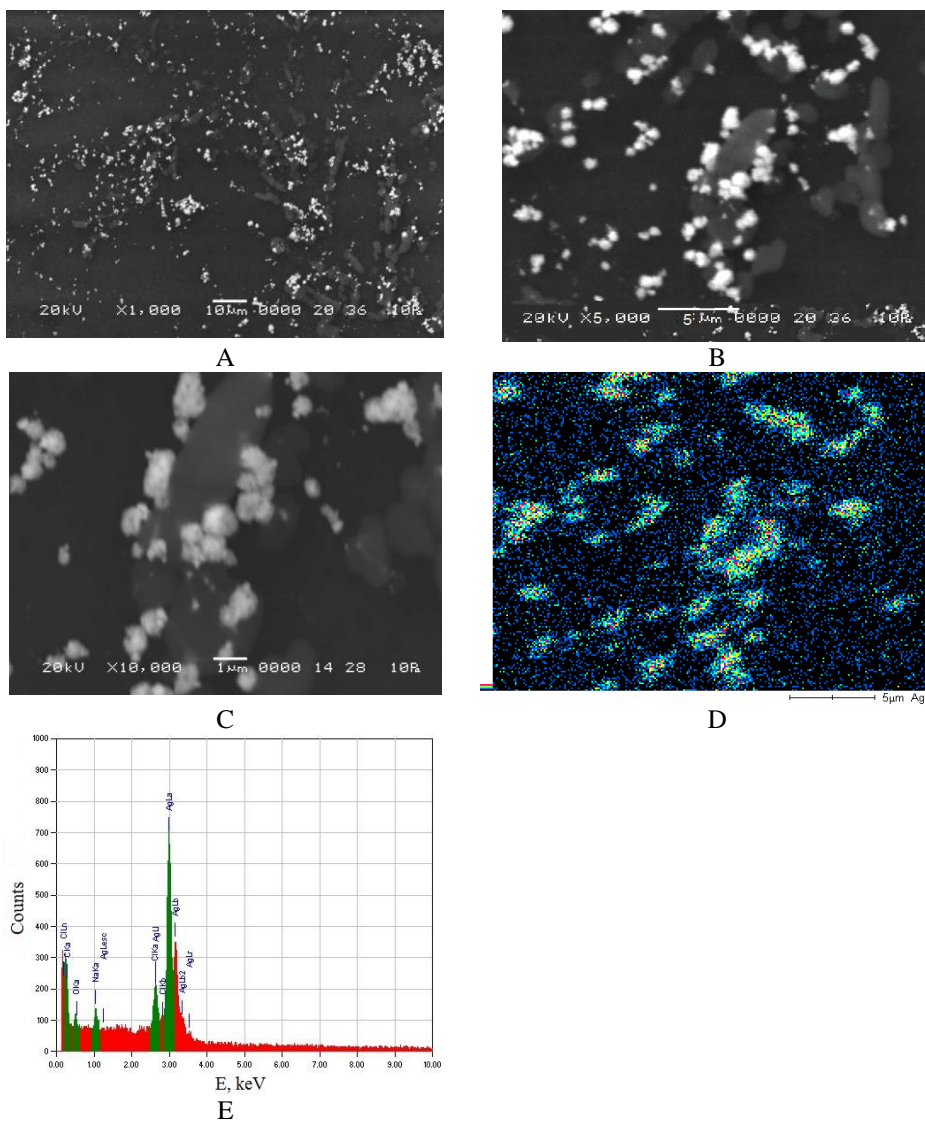
Fig. 3.39 SEM images, EDX spectra and map after film's irradiation with gamma rays (1.25 MeV)

Mechanical properties of the Ag/PVP nanocomposites were obtained by the UV irradiation induced variations of the surface morphology and adhesion force. Adhesion force can be measured by detecting the force interaction during cantilever tip approach and retraction from the film surface. Due to this, force–distance measurements for experimental films using atomic force microscope (AFM) NT-206 equipped with a silicon cantilever NSC11/15 were performed and corresponding curves indicating deflection of the force sensing cantilever were plotted as it is

shown in Fig. 3.40. The figure also includes AFM images indicating surface morphology of the same experimental films.
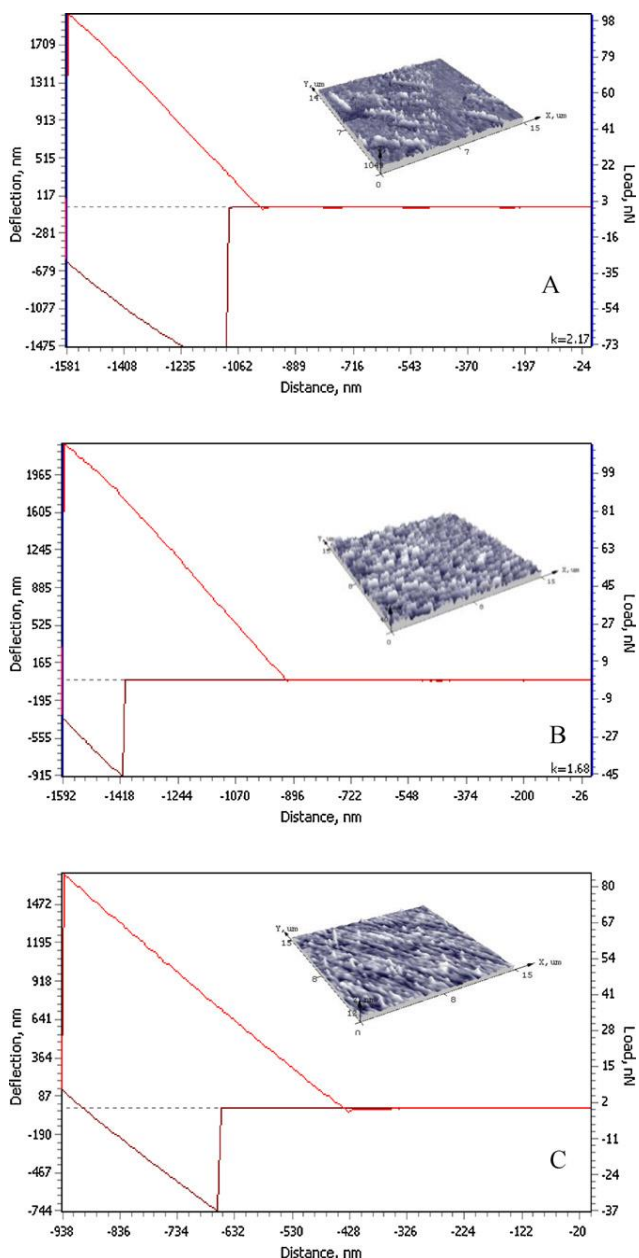
Fig. 3.40 Surface morphology and force curves of experimental films measured by AFM: A – unexposed Ag–PVP, B – Ag–PVP layer after 60 s UV irradiation, C – Ag–PVP layer after 150 s UV irradiation

Characteristic force–distance curves with a large hysteresis between loading and unloading parts have been observed. The adhesion force of experimental layers corresponding in the first approximation to the pull-off force between tip and film was calculated from the force–distance curves. It was shown the induced decreasing tendency of the adhesion force and sensitivity to the exposure time for UV irradiated Ag/PVP nanocomposites. Unexposed Ag/PVP layers adhesion force of 73 nN was measured by AFM (Fig. 3.40 A). It decreased from 45 nN (Fig. 3.40 B) to 23 nN (Fig. 3.40 C) when UV exposure time of films increased from 60 s to 150 s respectively. Irradiated Ag/PVP nancomposite layers were harder and flatter comparing with pure PVP or "as prepared" Ag/PVP layers. To get more precise information about the surface morphology AFM images (Fig. 3.40) were analyzed. It was found that examined surfaces of Ag/PVP composite films were very smooth with nano-size irregularities. The roughness, R_q, of 9.6 nm was estimated for unexposed Ag/PVP layers. The roughness of irradiated Ag/PVP composites was also dependent on UV irradiation time: it decreased from 5.8 nm (60 s UV irradiation) to 1.7 nm (150 s UV irradiation). Lower adhesion force and smoother surface exhibited tendency for Ag/PVP nanocomposites to become more hydrophobic after longer UV irradiation (Robertson, 2002).

AFM images indicating surface morphology of UV preirradiated (30 s) Ag/PVP composites exposed to different gamma irradiation doses are shown in Fig. 3.41 as well as dependencies of maximal load and adhesion force versus absorbed gamma irradiation doses obtained from AFM force–distance measurements are presented in Fig. 3.42.
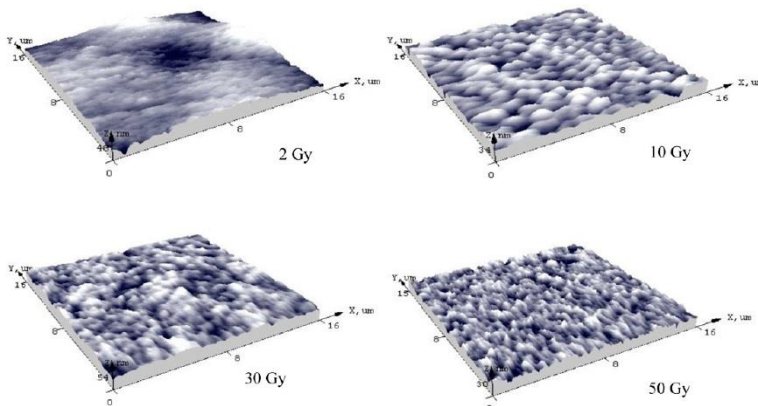
Fig. 3.41 AFM images of Ag/PVP nanocomposite layers on silica irradiated with different doses
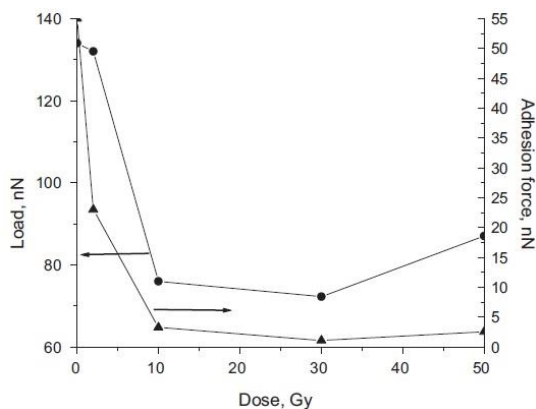
Fig. 3.42 Dose dependencies of maximal load and adhesion force of gamma irradiated Ag/PVP nanocomposite layers on silica measured by AFM

It was found that the adhesion force of Ag/PVP composite layers to the probe decreased almost exponentially with gamma irradiation dose being most sensitive to the small fraction of gamma irradiation dose (up to 10 Gy). In this dose region the adhesion force decreased significantly from 55 nN to 3.24 nN. Moreover the decrease of maximal load was observed. Most likely this effect is connected with radiation induced stress and strain in irradiated polymer structure as it was discussed in (Adliene et al., 2008; Šniurevičiūtė et al., 2009). Due to the small ionizing radiation dose Ag nanoparticles can diffuse to the top layer of mechanically unstable polymer matrix and the adhesion force decreases. Increased irradiation dose (> 10 Gy) initiates and supports polymer cross-linking process and leads to the controlled growth of nanoparticles and formation of a stable Ag/PVP nanocomposite structure. Adhesion force remains almost stable for higher irradiation doses. Similar decreasing tendency of the adhesion force with the increased gamma irradiation dose was found for the specimens UV preirradiated for 60 s.
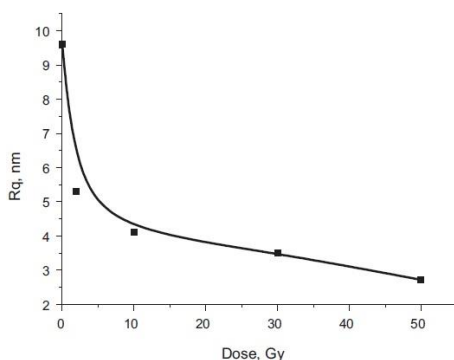
Fig. 3.43 Surface roughness of gamma irradiated Ag/PVP composite layers

The surface roughness of the irradiated Ag/PVP composite layers decreases from 9.6 nm to 2.8 nm with the increased irradiation dose almost exponentially (Fig. 3.43), indicating that the surface became smoother and the irradiation stable Ag/PVP layer has been formed. The behavior and properties of low dose gamma (2 – 50 Gy) irradiated composites were different as compared to the UV irradiated specimens due to the ionization ability of gamma irradiation. They differed from the properties of high dose (kGy range) gamma irradiated polymer structures where radiation induced significant changes in the molecular weight of polymer, in the silica transition temperature and activation energy was observed in (Eisa et al., 2011; O'Keeffe and Lewis, 2009).

Summary

The mechanisms of embedding silver nanoparticles in two different polymer matrices have been analyzed and implemented applying photon and electron irradiation for the synthesis of Ag nanoparticles and formation of Ag/polymer composites. Investigation of the surface morphology, optical and mechanical properties of Ag/polymer composites has shown that irradiation leads to significant changes of surface roughness as well as modification of surface plasmon properties.

- Formation of Ag nanocomposites directly from silver salts admixed to polymer solution employing UV photochemical synthesis and radiolysis induced by low dose rate photon irradiation is shown. It is found, that formation of composite is possible, but Ag/PMMA composites have no stability. PMMA tend to degrade therefore it doesn't ensure the stability of Ag nanoparticles within polymeric matrix. The prolong exposure time leads to agglomeration of Ag nanoparticles into larger clusters with induced disorder in the polymeric structure.

- The synthesis of Ag nanoparticles has been performed mixing the salt and polymer aqueous solution, which was influenced with different UV radiation doses as well as the modification of Ag/PVP nanocomposites was employing with different gamma doses. It was found that depending on the applied exposure parameters stable Ag/PVP composite structures with silver particles embedded within the polymer matrix are formed, however increasing the UV radiation dose, the adhesion with surface decreases. Varying the gamma photon radiation dose from 2 Gy to 10 Gy, the adhesion drastically decreases from 55 nN to 3.24 nN due to scission and crosslinking processes induced by ionizing radiation. Increasing gamma photon dose up to 20 Gy Ag particles tend to agglomerate to large structures

3.5.   Metal alloy/polymer nanocomposites

W-Co NPs were electrochemically synthesized in aqueous electrolyte containing cobalt sulfate and sodium tungstate as the source of metal species, and

tri-sodium citrate dehydrate as the complexing and buffering agent. The sodium dodecylsulphate was added to the mixture as a surfactant and stabilizer of synthesized W-Co NPs in electrolyte. All reagents were dissolved in double-distilled water with specific conductivity of $< 0.5 \ \mu S \cdot cm^{-1}$.

Table 3.11 Characteristics and components used for synthesis of W-Co alloy nanoparticles

Components	Concentration, mol/l
$Na_2WO_4 \cdot 2H_2O$	0.20
$CoSO_4 \cdot 7H_2O$	0.05
$Na_3C_6H_5O_7 \cdot 2H_2O$	0.25
$CH_3(CH_2)_{11}OSO_3Na$	0.01

Method of continuous ultrasound assisted sonoelectrochemical synthesis used for the production of W-Co NPs (Fig. 3.44); method is based on application of pulsed potential mode to working electrode under continuous impact of ultrasound waves on electrolyte.
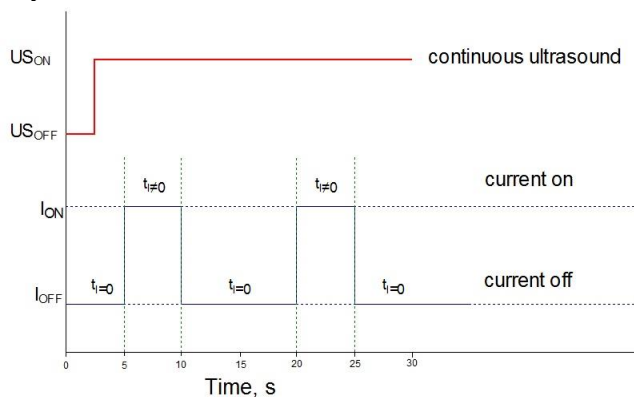
Fig. 3.44 Impulse diagram of the continuous ultrasound assisted electrolysis process

Prepared at room temperature electrolyte with pH = 9.1 was used to synthesize tungsten (W) and cobalt (Co) nanoparticles. Synthesis was performed at 60 °C warmed electrolyte; due to heating the pH slightly decreased to 8.5. For sonoelectrochemical experiment a thermostatic bath with frequency of 38 KHz was used to control the temperature of electrolyte (60 °C) as well it was positioned just below the electrochemical cell. Electrodeposition of W and Co nanoparticles was carried out in the potential pulse mode under continuous ultrasound. The electrochemical analyses were performed in Potentiostat/Galvanostat SP-150 (France, BioLogic) interfaced with EC-Lab (v10.19) software. The coatings were plated onto titanium alloy (Ti90-Al6-V4) plates serving as anode and cathode with dimensions of 3 x 100 x 0.5 mm respectively. Prior to the experiment Ti alloy plates were polished with Nr.600 emery paper, washed with distilled water and degreasing

with isopropanol. During the experiment, working electrode was pulse polarized from steady-state potential of approx. -0.16 V to -1.5 V (vs. Ag/AgCl). The impulse duration was t_{imp} = 500 ms. Electrochemical system relaxed between the pulses at open circuit conditions for t_{occ} = 800 ms. The sonoelectrochemical synthesis in pulsed potential mode lasted for 1h. The fragment of chronovoltamperometric pattern is shown in Fig. 3.45.
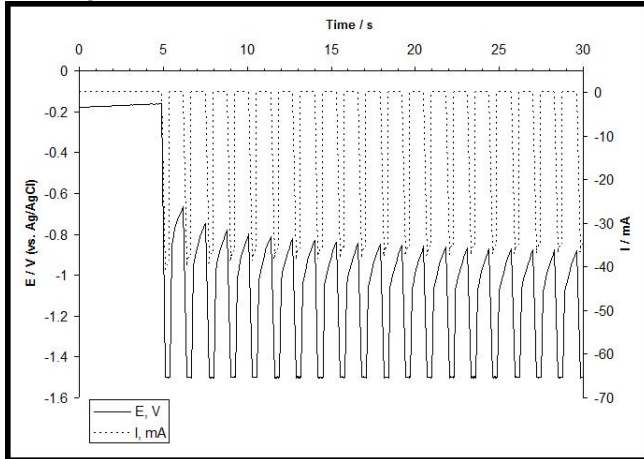
Fig. 3.45 The fragment of chronovoltamperometic pattern

It is known that the aqueous alkaline tungstate M_2WO_4 solution (here M = Li, Na, K) is commonly used for the tungsten electrodeposition. Electrodeposition is a process of electrochemical deposition of solid materials on an electrode surface using electrolysis via electrons transfer from work electrode for metallic ions reduction in solution (Garcia et al., 2013). However, for the electrochemical reduction of tungstate (VI) to metallic W (0) up to 6 electrons are required:

$$WO_4^{2-}{}_{(aq)} + 8H^+_{(aq)} + 6e^- \rightarrow W_{(s)} + 4H_2O_{(l)};$$ (3.13)
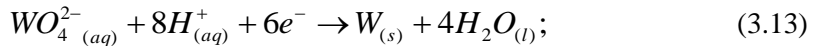
$E^0 = +0,049V$

Although the positive value of potential E^0 might lead to the theoretical assumption that the metallic tungsten should be easily electrodeposited from the aqueous solutions of salts, but in practice such a large number of electrons (up to 6 electrons) in one elementary electrochemical reaction step cannot attend. Therefore tungstate reduction to metallic W should take place in several simple intermediate stages. The first stage of electrochemical reduction of tungstate to tungsten (IV) oxide occurs in the presence of only two electrons.

$$WO_4^{2-}{}_{(aq)} + 4H^+_{(aq)} + 2e^- \rightarrow WO_{2(s)} + 2H_2O_{(l)};$$ (3.14)
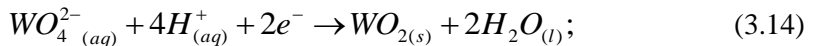
$E^0 = +0,386V$

The further tungstate reduction to metallic W is aggravated due to ongoing unfavorable electrochemical process - the release of gaseous hydrogen by reduction

of H^+ ions and/or H_2O molecules (depending on the electrolyte's composition, temperature, pH, etc.). The latter process results in relatively low hydrogen overvoltage values of formed tungsten-oxygen compounds on the surface. The hydrogen evolution can cause local changes in the pH leading to selective precipitation of some species on the growing deposit interface or induce morphological transitions and hydrogen embrittlement of the deposits.

Induced co-deposition is well known electrodeposition mechanism of iron group metals (Fe, Co, Ni) and also is used for the formation of electro coatings consisting of molybdenum and tungsten alloys. The induced co-deposition occurs when the cations of iron group metals are present in electrolyte (in this case Co^{2+} ions), to form alloys of these metals (W-Co alloys) (Brenner, 2013; Schlesinger and Paunovic, 2011). It is to notice that Co^{2+} ions are complexed with citrate $C_6H_5O_7^{3-}$ ions in the electrolyte:

$$Co^{2+}_{(aq)} + (C_6H_5O_7^{3-})_{(aq)} \rightarrow [Co(II)(C_6H_5O_7)]^-_{(aq)}; \qquad (3.15)$$
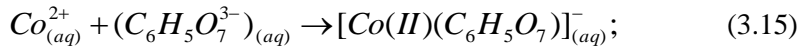
Taking into account presence of this complex ion in electrolyte, the main electrochemical reactions on the cathode are:

$$[Co(II)(C_6H_5O_7)]^-_{(aq)} + e^- \rightarrow [Co(I)(C_6H_5O_7)]^{2-}_{ads}; \qquad (3.16)$$

$$[Co(I)(C_6H_5O_7)]^{2-}_{ads} + e^- \rightarrow Co_{(s)} + (C_6H_5O_7^{3-})_{(aq)}; \qquad (3.17)$$
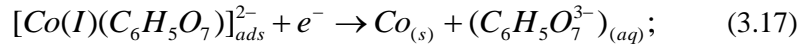
At the same time, the reduction of tungstate (VI) ions is catalyzed by complex particles $[Co(II)(C_6H_5O_7)]^-$ and the following reactions occur on the cathode:

$$WO_4^{2-}{}_{(aq)} + [Co(II)(C_6H_5O_7)]^{2-}_{ads} + 2H_2O + 2e^- \rightarrow$$
$$\rightarrow [Co(II)(C_6H_5O_7)WO_2]^-_{(ads)} + 4OH^-_{(aq)}; \qquad (3.18)$$

$$[Co(II)(C_6H_5O_7)WO_2]^-_{(ads)} + 2H_2O + 4e^- \rightarrow$$
$$\rightarrow W_{(s)} + [Co(II)(C_6H_5O_7)]^-_{(aq)} + 4OH^-_{(aq)}; \qquad (3.19)$$
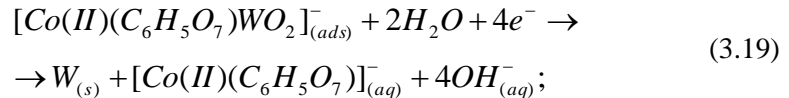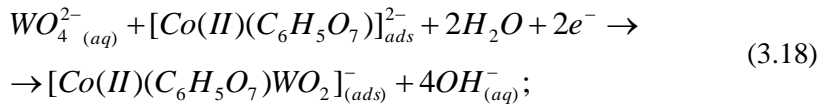
W and Co atoms deposited on the cathode in this way are forming W-Co alloy. Free hydrogen is also formed at the cathode due to the side reactions taking place in the weak alkaline electrolyte:

$$2H_2O_{(l)} + 2e^- \rightarrow H_{2(g)} + 2OH^-_{(aq)}; \qquad (3.20)$$
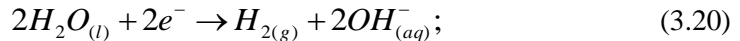
It is also to notice that the following reaction is present at the insoluble anode:

$$4OH^-_{(aq)} - 4e^- \rightarrow 2H_2O_{(l)} + O_{2(g)}; \qquad (3.21)$$
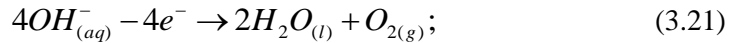
The presence of sonoelectrochemically synthesized nano/micro particles dispersed in electrolyte was checked passing the laser beams (red, $\lambda = 640$ nm and green, $\lambda = 532$ nm) through solution. Typical Tyndall cones of scattered light were observed in both cases (Fig. 3.46 A and Fig. 3.46 B). This phenomenon is always observed when nano-sized colloidal particles are dispersed in solution. Moreover, different shapes and intensities of Tyndall cones observed in colloidal solution when

laser beams of different wavelength pass through solution, proves the presence of differently sized W-Co NPs in it. For the comparison reference cuvettes filled with the same electrolyte before sonoelectrochemical synthesis were illuminated by laser beams as well. No scattered light (Tyndall cone) was observed in these cuvettes.

A   B
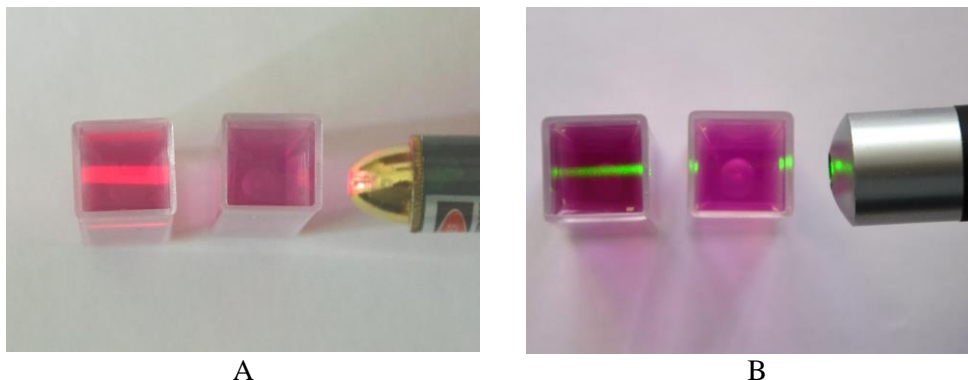
Fig. 3.46 The Tyndall cone in electrolyte with different wavelengths lasers: A - monochromatic red laser beam with $\lambda = 640$ nm (1 mW); B - monochromatic green laser beam with $\lambda = 532$ nm (50 mW)

Once detected, the size of synthesized W-Co NPs was investigated by PCS. It was found, that the particle's size varied from 100 nm to 500 nm. The smallest detected particle had a size of 70 nm, and the biggest - 930 nm. Normalized distribution of the detected particles according to their size is provided in the Fig. 3.47.
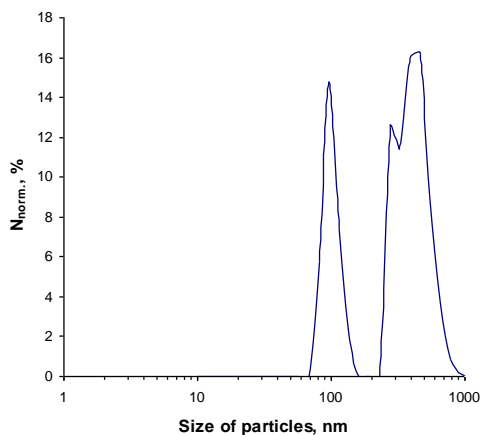
Fig. 3.47 The determination of W-Co nanoparticles

The surface morphology of the deposited particles, and their approximate chemical composition were studied by SEM and TEM. Analyzing typical SEM and

125

TEM images of sonoelectrically synthesized W-Co NPs (Fig. 3.48) it was found, that despite having different size the majority of produced particles had spherical shape. More detailed evaluation of particle' size was performed measuring diameter of particles in several directions on SEM and TEM images. It was found that the most frequent particles sizes were around 100 nm, 250 nm and 500 nm. However it is to point out that some larger structures consisting of already aggregated nanoparticles were also observed.

The internal structure of W-Co NPs was analyzed using TEM images. An example of TEM image is provided in Fig. 3.48 C where possible dispersion of Co nanoparticles within W nanoparticles could be observed. This is related to the fact that the fraction of Co atoms in nanoparticles is much smaller than that of W atoms in nanoparticles. According to the performed EDS measurements estimated atomic ratio of W and Co is 23:4. It corresponds to tungsten content in W-Co NPs approximately of 85 at. % as compared to 15 at. % of cobalt. Oxidation of W-Co NPs surface was also very likely.

Since a certain amount of free hydrogen was also present at the cathode, ultrasound was responsible for cavitation followed by explosive collapsing of hydrogen bubbles within a very short time after undergoing the formation, growth and retraction. Taking into account week adhesion of electrodeposits on the surface of Ti and its alloys, freshly formed aggregates of Co-W alloy, i.e. Co-W NPs, were easily detached from the surface of Ti alloy cathode. Detached NPs were subsequently dispersed in the bulk of electrolyte. Formation of W-Co aggregates was possible due to the several reasons: 1) Particular surface areas of Ti alloy electrode (e.g. edges and corners) may act as the areas with the higher cathode current density where the growth of NPs aggregates is promoted by each pulse of the cathode current; 2) Due to different adhesion of nanoparticles at various surface areas of working Ti alloy electrode some particles formed by cathode current are not detached from the surface of electrode under cavitation when the system operates in open circuit mode. These particles act as nucleation centers for growing of aggregates during following current pulses. The aggregates are growing continuously until critical mass necessary for particle's detachment from the electrode surface is achieved; 3) Agglomeration of individual nanoparticles to large-scale aggregates, when they are transferred from the aqueous electrolyte to organic solvent (chloroform). Continuous ultrasound is responsible for formation of cavitation in the deposit due to explosive collapsing of hydrogen bubbles. Cavitation results in detachment of particles from electrode and their dispersion in the solution.
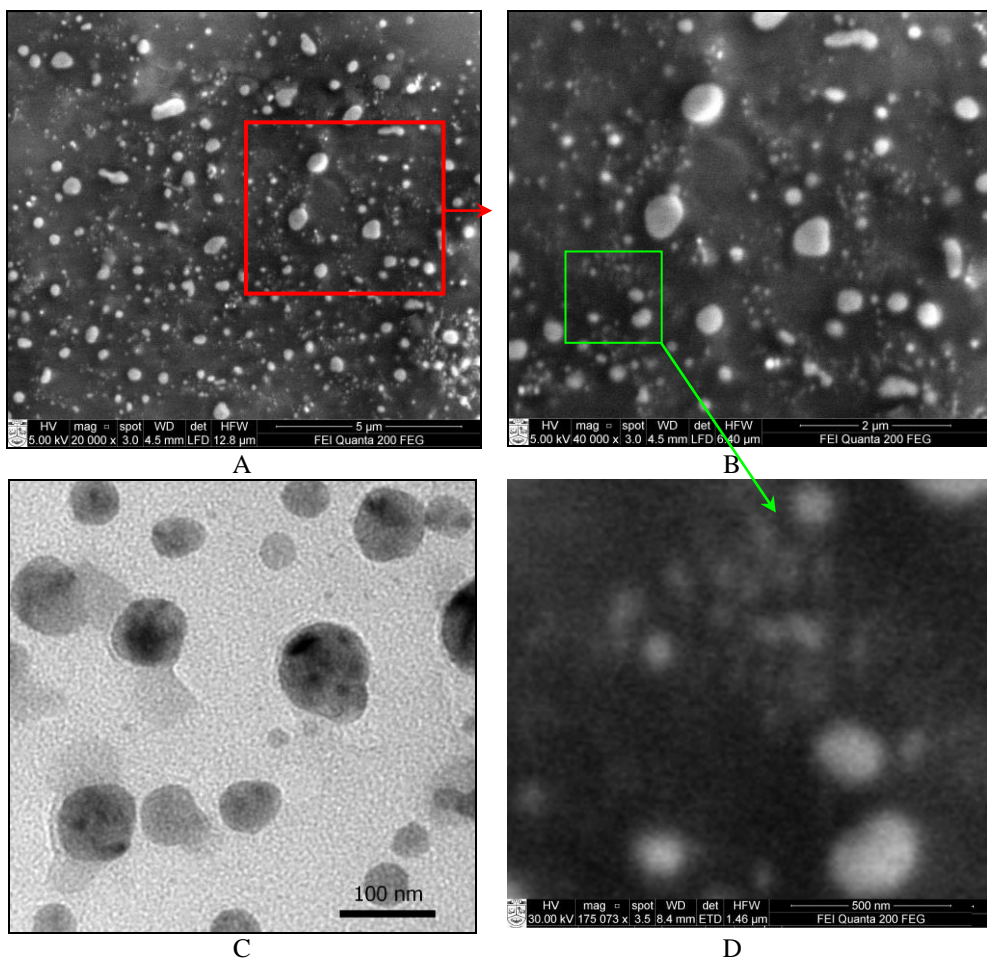
Fig. 3.48 SEM (A, B and D) and TEM (C) images of synthesized W-Co nanoparticles by sonoelectrodeposition

W-Co nanoparticles were transferred from the electrolyte to the ethanol (solvent compatible with PMMA), which was mixed with PMMA solution in order to form a W-Co/PMMA nanocomposite. W-Co/PMMA nanocomposite are the good expectants for radiation protection screens due to good X-ray absorption characteristics (lead equivalent of ~ 0.5 mm Pb). It was found that high (> 50 %) W-Co nanoparticles concentration that can provide X-ray absorption characteristics do not effective and do not ensure the stabilization of W-Co nanoparticles. As a result, nanoparticles tend to agglomerate to the large structures as well as falls out in powdery sediment. Such phenomenon do not observed when the concentration of nanoparticles is low, but it is not enough to form composite with necessary good X-rays absorption characteristics.

Summary

The new method of W-Co nanoparticles synthesis has been proposed involved the electrochemical synthesis of W-Co alloy nanoparticles under continuous ultrasound. Applying this method W-Co nanoparticles were formed dominantly in the size range of 100 – 500 nm (85 at.% W ir 15 at.% Co). Embedding W-Co alloy nanoparticles in polymers the polymeric W-Co/PMMA nanocomposites are forming. Such composite but with high (> 50 %) W-Co concentration could be applied for X-ray protection panel displays and radiation protection devices. However, the problem of stabilization of high concentration of W-Co nanoparticles in polymer do not solved yet.

CONCLUSIONS

1. Carbon coatings were synthesized by PECVD method from pure C_2H_2 gas varying the bias voltage (80 – 480 V) and temperature (273 – 673 K). According to the results of performed analysis, experimental coatings were assigned to polymer like amorphous hydrogenated carbon coatings. It was found that increasing the bias up to 200 V, the coating formed with embedded graphite clusters, which potentially increases the hardness of the formed coating. The presence of transpolyacetylene in coatings was indicated according to the Raman spectroscopy results when the substrate temperature was > 300 K.

2. It was found that high energy electrons and photons initiated the restructuration of the carbon coatings followed by the hydrogen desorption from the coatings as well as the formation of new polymer structures with embedded sp^2 graphite clusters. A formation tendency of such structures was well pronounced in all coatings, synthesized at the temperatures higher than 20 °C. It was found that due to radiation induced structural changes the optical transparency of carbon coatings was decreasing while the hardness was increasing.

3. Applying the two-step mechanism (photosynthesis and radiolysis) for the synthesis of particles from Ag salts dissolved directly in MMA solution it was shown, that irradiation of films with low dose rate X-rays allowed formation of Ag/polymer composite. However synthesized Ag particles showed agglomeration tendency with the increasing exposure time (dose) which resulted in the formation of disordered structures.

4. Investigation of Ag nanoparticles synthesized from the UV irradiated mixture of aqueous solutions of salt and polymer has shown that increasing UV radiation time from 15 to 300 s the adhesion force of coating was decreasing from 73 nN to 23 nN. Additional irradiation of experimental coatings with gamma photons to the doses ranging from 2 Gy to 10 Gy, the adhesion force was drastically decreasing from 55 nN to 3.24 nN due to the scission and crosslinking processes induced by ionizing radiation. The increase of gamma photon dose up to 20 Gy caused agglomeration of Ag particles.

5. Based on the assessment of the empirical-chemical mechanism of W-Co nanoparticle formation, a new method for the electrochemical synthesis of nanoparticles under continuous ultrasound has been proposed and adapted and W-Co nanoparticles with a size of 100 – 500 nm were produced. It was found that optically transparent W-Co/PMMA composite could be formed embedding the synthesized W-Co nanoparticles in PMMA matrix at low concentrations. However increasing the concentration of W-Co nanoparticles the composite transparency was decreasing and nanoparticles were tending to agglomerate and fall out in powdery sediments.

LIST OF REFERENCES

1. ABDEL HAMID Z. Electrodeposition of cobalt-tungsten alloys from acidic bath containing cationic surfactants. *Mater. Lett*. 2003, Vol. 57, 2558–2564, doi:10.1016/S0167-577X(02)01311-3;
2. ABU BAKAR N.H.H., ISMAIL J., ABU BAKAR M. Silver nanoparticles in polyvinylpyrrolidone grafted natural rubber. *Reactive & Functional Polymers*, 2010, Vol. 70, 168–174; doi: 10.1016/j.reactfunctpolym.2009.11.009;
3. ABYANEH M.K., PARAMANIK D., VARMA S., GOSAWI S.W., KULKARNI S.K. Formation of gold nanoparticles in polymethylmethacrylate by UV irradiation. *J. Phys. D: Appl. Phys*. 2007, Vol. 40, 3771–3779, doi:10.1088/0022-3727/40/12/032;
4. ADLIENĖ D., LAURIKAITIENĖ J., KOPUSTINSKAS V., MEŠKINIS Š., ŠABLINSKAS V. Radiation induced changes in amorphous hydrogenated DLC films. *Materials Science and Engineering B*, 2008, Vol. 152, 91–95, doi:10.1016/j.mseb.2008.06.005;
5. ADLIENĖ D., LAURIKAITIENĖ J., TAMULEVIČIUS S. Modification of amorphous DLC films induced by MeV photon irradiation. *Nuclear Instruments and Methods in Physics Research B*, 2008, Vol. 266, 2788–2792 doi:10.1016/j.nimb.2008.03.118;
6. ADLIENĖ D., CIBULSKAITĖ I., MEŠKINIS Š. Low energy X-ray radiation impact on coated Si constructions. *Radiation Physics and Chemistry*, 2010, Vol. 79, 1031–1038; doi: 10.1016/j.radphyschem.2010.05.003;
7. ADLIENĖ D., LAURIKAITIENĖ J., ANDRULEVIČIUS M., GUOBIENĖ A., MEŠKINIS Š., CIBULSKAITĖ I., TAMULEVIČIUS S. Mechanical properties of the X-ray irradiated DLC films containing SiOx as a constructive element for radiation detectors. *Nuclear Instruments and Methods in Physics Research A*, 2008, Vol. 591, 188–191; doi:10.1016/j.nima.2008.03.053;
8. AHMAD A., MOHD D.H., ABDULLAH I. Electron Beam Cross-linking of NR/LLDPE Blends. Iranian Polymer Journal, 2005, Vol. 14 (6), 505-510;
9. AISENBERG S., CHABOT R. Deposition of carbon films with diamond properties. *Carbon,* 1972, Vol. 10, p. 356;
10. AKHAVAN A., SHEIKH N., BETESHOBABRUD R. Polymethylmethacrylate/Silver Nanocomposite Prepared by γ-Ray. *J. of Nuclear Sci. and Tech*. 2010,Vol. 41 (30), 80-84, ISSN 1735-1871;
11. ALAHMAD A. Preparation and Characterization of Silver Nanoparticles. *Int. J. Chem. Tech. Res*. 2014, Vol. 6 (1), 450-459;
12. ALEXANDROV A., SMIRNOVA L., YAKIMOVICH N., SAPOGOVA N., SOUSTOV L., KIRSANOV A., BITYURIN N. UV-initiated growth of gold nanoparticles in PMMA matrix. *Applied Surface Science*, 2005, Vol. 248, 181–184; doi:10.1016/j.apsusc.2005.03.002;
13. ALSAWAFTA M., BADILESCU S., PANERI A., TRUONG Vo-Van, PACKIRISAMY M. Gold-Poly(methyl methacrylate) Nanocomposite Films for Plasmonic Biosensing Applications. *Polymers*, 2011, Vol. 3, 1833-1848; doi:10.3390/polym3041833;
14. AMENDOLA V., BAKR O.M., STELLACCI F. A Study of the Surface Plasmon Resonance of Silver Nanoparticles by the Discrete Dipole Approximation Method:

130

Effect of Shape, Size, Structure, and Assembly. *Plasmonics*, 2010, Vol. 5, 85–97, doi:10.1007/s11468-009-9120-4;

15. ANANDHAN S., BANDYOPADHYAY S. Polymer Nanocomposites: From Synthesis to Applications, Nanocomposites and Polymers with Analytical Methods, 2011, Dr. John Cuppoletti (Ed.), ISBN: 978-953-307-352-1, InTech, Available from: http://www.intechopen.com/books/nanocomposites-and-polymers-with-analyticalmethods/polymer-nanocomposites-from-synthesis-to-applications;

16. ASTRUC D. Nanoparticles and Catalysis, VCH, Weinheim, 2004;

17. ATHAWALE A.A., KATRE P.P., KUMAR M., MAJUMDAR M.B. Synthesis of CTAB-IPA reduced copper nanoparticles. *Mater. Chem. Phys*. 2005, Vol. 91 (2-3), 507–512, doi:10.1016/j.matchemphys.2004.12.017;

18. BERRET J.F., YOKOTA K., MORVAN M., SCHWEINS R. Polymer - Nanoparticle Complexes: From Dilute Solution to Solid State. *J. Phys. Chem. B,* 2006, Vol. 110 (39), 19140–19146, doi:10.1021/jp0603177;

19. BHATTACHARYA A. Radiation and industrial polymers. *Prog. Polym. Sci*. 2000, Vol. 25, 371–401;

20. BIRKIN P.R., OFFIN D.G., JOSEPH P.F., LEIGHTON T.G. Cavitation, Shock Waves and the Invasive Nature of Sonoelectrochemistry. *Journal of physical chemistry B*, 2005, Vol. 109, 16997-17005;

21. BISWAL J., MISRA N., BORDE L.C., SABHARWAL S. Synthesis of silver nanoparticles in methacrylic acid solution by gamma radiolysis and their application for estimation of dopamine at low concentrations. *Radiation Physics and Chemistry*, 2013, Vol. 83, 67–73; doi: 10.1016/j.radphyschem.2012.10.003;

22. BRENNER A. Electrodeposition of Alloys: Principles and Practice. Elsevier, 2013, 734 p., ISBN 1483223116;

23. KHARISOV B.I., KHARISSOVA O.V. Main Ionizing radiation Types and Their Interaction with Matter. *Radiation Synthesis of materials and Compounds*, 2013;

24. BUIJNSTERS J.G., GAGO R., REDONDO-CUBERO A., JIMENEZ I. Hydrogen stability in hydrogenated amorphous carbon films with polymer-like and diamond-like structure. *J. Appl. Phys*. 2012, Vol. 112, 093502, doi:10.1063/1.4764001;

25. CALINESCU I., MUSTATEA G., GAVRILA A.I., DOBRE A., POP C. Silver Nanoparticles: Synthesis, Characterization and Antibacterial Activity. REV. CHIM. 2014, Vol. 65 (1), 15-19;

26. CALINESCU I., MARTIN D., IGHIGEANU D., GAVRILA A.I., TRIFAN A., PATRASCU M., MUNTEANU C., DIACON A., MANAILA E., CRACIUN G. Nanoparticles synthesis by electron beam radiolysis. *Cent. Eur. J. Chem*. 2014, Vol. 12 (7), 774–781; doi: 10.2478/s11532-014-0502-x;

27. CASARI C.S., LI BASSI A., BASERGA A., RAVAGNAN L., PISERI P., LENARDI C., TOMMASINI M., MILANI A., FAZZI D., BOTTANI C.E., MILANI P. Low-frequency modes in the Raman spectrum of *sp-sp*2 nanostructured carbon. *Phys. Rev. B*, 2008, Vol. 77, 195444, doi:10.1103/PhysRevB.77.195444;

28. CASIRAGHI C., ROBERTSON J., FERRARY A.C. Diamond-like carbon for data and beer storage. Materials Today, 2007, Vol. 10 (1-2), 44-53, doi: 10.1016/S1369-7021(06)71791-6;

29. CHEN X., SCHLUESENER H.J. Nanosilver: A nanoproduct in medical application. *Toxicol Lett*, 2008, Vol. 176, 1–12, doi:10.1016/j.toxlet.2007.10.004;

30. CHMIELEWSKI A.G., CHMIELEWSKA D.K., MICHALIK J., SAMPA M.H. Prospects and challenges in application of gamma, electron and ion beams in processing of nanomaterials. *Nuclear Instruments and Methods in Physics Research B*, 2007, Vol. 265, 339–346; doi: 10.1016/j.nimb.2007.08.069;

31. CHOI S.H., ZHANG Y.P., GOPALAN A., LEE K.P., KANG H.D. Preparation of catalytically efficient precious metallic colloids by γ-irradiation and characterization. Colloids and Surfaces A: Physicochem. Eng. Aspects, 2005, Vol. 256, 165-170, doi: 10.1016/j.colsurfa.2004.07.022;

32. CHU P.K., LI L. Characterization of amorphous and nanocrystalline carbon films. *Materials Chemistry and Physics*, 2006, Vol. 96, 253–277; doi:10.1016/j.matchemphys.2005.07.048;

33. ÇAPAN İ., TARIMCI Ç., HASSAN A.K., TANRISEVER T. Characterisation and optical vapor sensing properties of PMMA thin films. *Materials Science and Engineering C*, 2009, Vol. 29, 140–143; doi:10.1016/j.msec.2008.05.021;

34. DADOSH T. Synthesis of uniform silver nanoparticles with a controllable size. *Mater. Lett.* 2009, Vol. *(63),* 2236–2238;

35. DAHAL P., KIM Y.C. Preparation and characterization of modified polypropylene by using electron beam irradiation. *Journal of Industrial and Engineering Chemistry,* 2013, Vol. 19, 1879–1883; doi:10.1016/j.jiec.2013.02.027;

36. DALLAS P., SHARMA V. K., ZBORIL R. Silver polymeric nanocomposites as advanced antimicrobial agents: Classification, synthetic paths, applications, and perspectives. *Adv Colloid Interfac,* 2011, Vol. 166, 119–135, doi:10.1016/j.cis.2011.05.008;

37. DAS R.S., AGRAWAL Y.K. Raman spectroscopy: Recent advancements, techniques and applications. Vibrational Spectroscopy, 2011, Vol. 57, 163-176, doi: 10.1016/j.vibspec.2011.08.003;

38. DELPHINE S.M., JAYACHANDRAN M., SANJEEVIRAJA C. Pulsed electrodeposition and characterisation of tungsten diselenide thin films. *Mater. Chem. Phys*. 2003, Vol. 81, 78–83, doi:10.1016/S0254-0584(03)00136-6;

39. DONTEN M., STOJEK Z., CESIULIS H. Formation of Nanofibers in Thin Layers of Amorphous W Alloys with Ni, Co, and Fe Obtained by Electrodeposition, J. Electrochem. Soc., 2003, Vol. 150 (2), 95–98, doi:10.1149/1.1536994;

40. DROBNY J.G. Ionizing Radiation and Polymers: Principles, Technology, and Applications. 2012, DOI:10.1016/B978-1-4557-7881-2.00001-8

41. EISA W.H., ABDEL-MONEAM Y.K., SHAABAN Y., ABDEL-FATTAH A.A., ABOU ZEID A.M. Gamma-irradiation assisted seeded growth of Ag nanoparticles within PVA Matrix. *Materials Chemistry and Physics*, 2011, Vol. 128, 109–113; doi:10.1016/j.matchemphys.2011.02.076;

42. ESKUSSON J., JAANISO R., LUST E. Diamond-like phase formation in an amorphous carbon films prepared by periodic pulsed laser deposition and laser irradiation method. *Applied Surface Science*, 2009, Vol. 255 (15), 7104-7108, doi: 10.1016/j.apsusc.2009.03.042;

43. EVANOFF D.D., and CHUMANOV G. Synthesis and Optical Properties of Silver Nanoparticles and Arrays. *ChemPhysChem*, 2005, Vol. 6, 1221 – 1231 doi: 10.1002/cphc.200500113;

44.   FAN X., ZHENG W., SINGH D. Light scattering and surface plasmons on small spherical particles. *Light: Science & Applications*, 2014, Vol. 3 (e179), doi: 10.1038/lsa.2014.60;

45.   FANG C.K. Mechanical and Tribological Investigations on Carbon Allotropes. *Bulletin of College of Engineering*, National Ilan University, 2009, Vol. 5, 131-167;

46.   FERRARY A.C. Determination of bonding in diamond-like carbon by Raman spectroscopy. Diamond and Related Materials, 2002, Vol. 11, 1053–1061;

47.   FERRARY A.C. Diamond-like carbon for magnetic storage disks. Surface and Coatings Technology, 2004, Vol. 180-181, 190-206, doi: 10.1016/j.surfcoat.2003.10.146;

48.   FERRARY A. C., ROBERTSON J. Raman spectroscopy of amorphous, nanostructured, diamond-like carbon, and nanodiamond. *Philosophical Transactions of the Royal Society A-Mathematical Physical and Engineering Sciences,* 2004, Vol. 362, 2477-2512;

49.   FYTA M., MATHIOUDAKIS Ch., REMEDIAKIS I.N., KELIRES P.C., Carbon-based nanostructured composite films: Elastic, mechanical and optoelectronic properties derived from computer simulations Surf. Coat. Technol., 2011, doi:10.1016/j.surfcoat.2011.02.026;

50.   GARCIA E.M., LINS V.F.C., MATENCIO T. Metallic and Oxide Electrodeposition. Modern Surface Engineering Treatments, INTECH, 2013, 101-122,doi: 10.5772/55684;

51.   GARCIA-LEIS A., GARCIA-RAMOS J.V., SANCHEZ-CORTES S. Silver Nanostars with High SERS Performance. *J. Phys. Chem. C*, 2013, Vol. 117 (15), 7791-7795, doi: 10.1021/jp101737y;

52.   GEDANKEN A. Using sonochemistry for the fabrication of nanomaterials. *Ultrason. Sonochem.*, 2004, Vol. 11, 47–55, doi:10.1016/j.ultsonch.2004.01.037;

53.   GODET C., HEITZ T., BOUREE J. E., DREVILLON B., CLERC C. Growth and composition of dual-plasma polymer-like amorphos carbon films. *J. Appl. Phys*. 1998, Vol. 84, 3919-3932;

54.   GONZALEZ-GARCIA J., ESCLAPEZ M.D., BONETE P., VARGAS HERNANDEZ Y., GARRETON L.G., SAEZ V. Current topics on sonoelectrochemistry, *Ultrasonics*, 2010, Vol. 50, 318–322, doi:10.1016/j.ultras.2009.09.022;

55.   GRIGONIS A., MARCINAUSKAS L., VINCIŪNAITĖ V., RAČIUKAITIS G. Modification of the amorphous carbon films by the ns-lase irradiation. *Central European Journal of Physics*, 2011, Vol. 9 (5), doi: 10.2478/s11534-011-0037-0;

56.   GRIGONIS A., RUTKŪNIENĖ Ž. Atominių dalelių sąveika su medžiaga. Mokomoji knyga, Šiauliai, 2007, 181 p, ISBN 978-9986-38-805-0;

57.   GRILL A. Diamond-like carbon: state of the art. *Diamond and Related Materials*, 1999,Vol. 8, 428–434;

58.   HÄKKINEN H., MOSELER M., KOSTKO O., MORGNER N., ASTRUC HOFFMAN M., v. ISSENDORFF B. Symmetry and Electronic Structure of Noble-Metal Nanoparticles and the Role of Relativity. *Phys. Rev. Lett.* 2004, Vol. 93 (9), doi: 10.1103/PhysRevLett93.093401;

59.   HARAM S.K., MAHADESHWAR A.R., DIXIT S.G. Synthesis and characterization of copper sulfide nanoparticles in Triton-X 100 water-in-oil microemulsions. *J. Phys. Chem*. 1996, Vol. 100 (14), 5868–5873, doi:10.1021/jp952391n;

60. HATANO Y., KATSUMURA Y., MOZUMDER A. Charged Particle and Photon Interactions with Matter: Recent Advances, Applications and Interfaces. CRC Press, 2010, 1064 p, ISBN 1439811806;

61. HILL D.J.T., WHITTAKER A.K. Radiation chemistry of polymers, Encyclopedia of Polymer Science and Technology. 2004, doi:10.1002/0471440264.pst488;

62. HOSHINO K., HITSUOKA Y. One-step template-free electrosynthesis of cobalt nanowires from aqueous $[Co(NH_3)_6]Cl_3$ solution. *Electrochem. Commun.* 2005, Vol. 7, 821–828, doi:10.1016/j.elecom.2005.04.038;

63. HUTTER E. and FENDLER J.H. Exploitation of localized surface plasmon resonance. *Adv. Mater.*, 2004, Vol. 16 (19), doi:10.1002/adma.200400271;

64. HUTTER E., FENDLER J. H., ROY D. Surface Plasmon Resonance Studies of Gold and Silver Nanoparticles Linked to Gold and Silver Substrates by 2-Aminoethanethiol and 1,6-Hexanedithiol; *J. Phys. Chem. B,* 2001, Vol. 105, 11159-11168; doi:10.1021/jp011424y;

65. HWANG N.M., JUNG J. S. and LEE D.K. Thermodynamics and Kinetics in the Synthesis of Monodisperse Nanoparticles. *Thermodynamics – Fundamentals and Its Application in Science*, INTECH, 2012, doi:10.5772/50324;

66. IBRAHIM N.A., AHMAD S.N.A., YUNUS W.M.Z.W., DAHLAN K.Z.M. Effect of electron beam irradiation and poly(vinyl pyrrolidone) addition on mechanical properties of polycaprolactone with empty fruit bunch fibre (OPEFB) composite. *eXPRESS Polymer Letters,* 2009, Vol. 3 (4), 226–234, doi: 10.3144/expresspolymlett.2009.29;

67. IMAI R., FUJIMOTO A., OKADA M., MATSUI S., YOKOGAWA T., MIURA E., YAMASAKI T., SUZUKI T., KANDA K. Soft X-ray irradiation effect on the surface and material properties of highly hydrogenated diamond-like carbon thin films. *Diamond & Related Materials*, 2014, Vol. 44, 8–10, doi:10.1016/j.diamond.2014.01.018;

68. INDYKA P., BELTOWSKA-LEHMAN E., TARKOWSKI L., BIGOS A., GARCIA-LECINA E. Structure characterization of nanocrystalline Ni-W alloys obtained by electrodeposition. *J. Alloy Compd*. 2014, Vol. 590, 75–79, doi:10.1016/j.jallcom.2013.12.085;

69. JAKUBIENĖ V. Organinė chemija. Mokomoji knyga. Vilnius, 2009, 156 p.;

70. JEEVANANDAM P., SRIKANTH C.K., DIXIT S. Synthesis of monodisperse silver nanoparticles and their self-assembly through simple thermal decomposition approach. *Material Chemistry and Physics*, 2010, Vol. 122 (2-3), 402-407, doi: 10.1016/j.matchemphys.2010.03.015;

71. JOVANOVIČ Z., RADOSAVLJEVIČ A., SILJEGOVIČ M., BIBIČ N., MIŠKOVIČ-STANKOVIČ V., KACAREVIČ-POPOVIČ Z. Structural and optical characteristics of silver/poly (N-vinyl-2-pyrrolidone) nanosystems synthesized by γ-irradiation. *Radiation Physics and Chemistry*, 2012, Vol. 81, 1720–1728; doi:10.1016/j.radphyschem.2012.05.019;

72. JURASEKOVA Z., SANCHEZ-CORTES S., TAMBA M., TORREGGIANI A. Silver nanoparticles active as surface-enhanced Raman scattering substrates prepared by high energy irradiation. *Vibrational Spectroscopy*, 2011, Vol. 57, 42–48; doi:10.1016/j.vibspec.2011.05.001;

73. KANGO S., KALIA S., CELLI A., NJUGUNA J., HALIBI Y., KUMAR R. Surface modification of inorganic nanoparticles for development of organic–inorganic

nanocomposites—A review. *Progress in Polymer Science*, 2013, Vol. 38, 1232– 1261; doi:10.1016/j.progpolymsci.2013.02.003;

74. KARAAGAC O., KOCKAR H., ALPER M. Electrodeposited cobalt films: The effect of deposition potentials on the film properties. Journal of Optoelectronics and Advanced Materials, 2013, Vol. 15 (11), 1412-1416;

75. KARAMI H., MOHAMMADZADEH E. Synthesis of Cobalt Nanorods by the Pulsed Current Electrochemical Method. *Int. J. Electrochem. Sci*., 2010, Vol. 5, 1032 – 1045;

76. KHAN Z., AL-THABAITI S.A., OBAID A.Y., AL-YOUBI A.O. Preparation and characterization of silver nanoparticles by chemical reduction method. *Colloids and Surfaces B: Biointerfaces*, 2011, Vol. 82, 513–517; doi: 10.1016/j.colsurfb.2010.10.008;

77. KIM M.C., CHO S.H., LEE S.B., KIM Y., BOO J.H. Characterization of polymer-like thin film deposition on silicon and glass substrates using PECVD method. *Thin Solid Films*, 2004, Vol. 447–448, 592–598, doi:10.1016/j.tsf.2003.07.021;

78. KIM Y.H., LEE D.K., JO B.G., JEONG J.H., KANG Y.S. Synthesis of oleate capped Cu nanoparticles by thermal decomposition. *Colloids Surf. A*, 2006, Vol. 284-285, 364–368;

79. KLIMA J. Application of ultrasound in electrochemistry. An overview of mechanisms and design of experimental arrangement. *Ultrasonics*, 2011, Vol. 51, 202–209, doi:10.1016/j.ultras.2010.08.004;

80. KNAUERT S.T., DOUGLAS J.F., STARR F.W. The Effect of Nanoparticle Shape on Polymer-Nanocomposite Rheology and Tensile Strength. *J. Polym. Sci. B – Polym. Phys.*, 2007, Vol. 45 (14), 1882-1897, doi:10.1002/polb.21176;

81. KHARISOV B.I., KHARISSOVA O.V. Main Ionizing radiation Types and Their Interaction with Matter. *Radiation Synthesis of materials and Compounds*, 2013;

82. KRSTIĆ J., SPASOJEVIĆ J., RADOSAVLJEVIĆ A., ŠILJEGOVĆ M., KAČAREVIĆ-POPOVIĆ Z. Optical and structural properties of radiolytically in situ synthesized silver nanoparticles stabilized by chitosan/poly(vinylalcohol) blends. *Radiation Physics and Chemistry*, 2014, Vol. 96, 158–166; doi: 10.1016/j.radphyschem.2013.09.013;

83. LACKNER J.M., MAJOR R., MAJOR L., SCHÖBERL T., WALDHAUSER W. RF deposition of soft hydrogenated amorphous carbon coatings for adhesive interfaces on highly elastic polymer materials. *Surface & Coatings Technology*, 2009, Vol. 203, 2243–2248; doi:10.1016/j.surfcoat.2009.02.012;

84. LaMER V.K., DINEGAR R.H., *J. Am. Chem. Soc*., 1950, Vol. 72, 4847;

85. LI Sh., LIN M.M., TOPRAK M.S., KIM D.K., MUHAMMED M. Nanocomposites of polymer and inorganic nanoparticles for optical and magnetic applications. *Nano Reviews,* 2010, Vol. 1, 5214, doi:10.3402/nano.v1i0.5214;

86. LIFSHITZ Y. Diamond-like carbon—present status. *Diamond and Related Materials*, 1998, Vol. 8, 1659–1676;

87. LIU Y., CHEN S., ZHONG L., WU G. Preparation of high-stable silver nanoparticle dispersion by using sodium alginate as a stabilizer under gamma radiation. *Radiation Physics and Chemistry*, 2009, Vol. 78, 251–255; doi: 10.1016/j.radphyschem.2009.01.003;

88. LU L., SEVONKAEV I., KUMAR A., DAN V. GOIA, Strategies for tailoring the properties of chemically precipitated metal powders. *Powder Technology*, 2014, Vol. 261, 87–97. doi:10.1016/j.powtec.2014.04.015;

89. LUO J.K., FU Y.Q., LE H.R., WILLIAMS J.A., SPEARING S.M., MILNE W.I. Diamond and diamond-like carbon MEMS. J. Micromech. Microeng. 2007, Vol. 17, S147–S163, doi:10.1088/0960-1317/17/7/S12;

90. MAHALIK D.B., SHINDE S.S., BHOSALE C.H., RAJPURE K.Y. Physical properties of chemical vapour deposited nanostructured carbon thin films. *Journal of Alloys and Compounds*, 2011, Vol. 509, 1418–1423; doi:10.1016/j.jallcom.2010.11.021;

91. MAKUUCHI K., CHENG S. Index, in Radiation Processing of Polymer Materials and its Industrial Applications. 2012, John Wiley & Sons, Inc., Hoboken, NJ, USA. doi: 10.1002/9781118162798.index

92. MALINA D., SOBCZAK-KUPIEC A., WZOREK Z., KOWALSKI Z. Silver nanoparticles synthesis with different concentrations of polyvinylpyrrolidone. Digest Journal of Nanomaterials and Biostructures, 2012, Vol. 7 (4), 1527-1534;

93. MANAI L., DRIDI REZGUI B., BOU A., BARAKEL D., TORCHIO P., BENABDERRAHMANE R., PALAIS O., BESSAIS B. Enhanced light trapping using plasmonic nanoparticles. *Journal of Physics: Conference Series*, 2015, Vol. 596, doi: 10.1088/1742-6596/596/1/012002;

94. MARCINAUSKAS L., GRIGONIS A., KULIKAUSKAS V., VALINCIUS V. Synthesis of carbon coatings employing a plasma torch from an argon–acetylene gas mixture at reduced pressure. *Vacuum*, 2007, Vol. 81, 1220–1223, doi:10.1016/j.vacuum.2007.01.028;

95. MARCINAUSKAS L., GRIGONIS A., VALATKEVICIUS P., MEDVID A. Irradiation of the graphite-like carbon films by ns-laser pulse. *Applied Surface Science*, 2012, Vol. 261, 488-492, doi: 10.1016/j.apsusc.2012.08.042;

96. MARCINAUSKAS L., SILINSKAS M., GRIGONIS A. Influence of standoff distance on the structure and properties of carbon coatings deposited by atmospheric plasma jet. *Applied Surface Science*, 2011, Vol. 257, 2694–2699, doi:10.1016/j.apsusc.2010.10.047;

97. MARCINAUSKAS L., VALINCIUS V., GRIGONIS A. Deposition and structure characterization of carbon films prepared at atmospheric pressure by plasma jet. *Surface & Coatings Technology*, 2011, Vol. 205, S71–S74, doi:10.1016/j.surfcoat.2010.12.041;

98. MEŠKINIS Š., GUDAITIS R, TAMULEVIČIENĖ A., KOPUSTINSKAS V., ŠLAPIKAS K., TAMULEVIČIUS S. The Investigation of Piezoresistive, Optical and Electrical Properties of Diamond Like Carbon Films Synthesized by Ion Beam Deposition and PECVD, *Materials Science (Medžiagotyra)*, 2010, Vol 16, No. 4, ISSN 1392-1320;

99. MIKHLIN Y.L., VISHNYAKOVA E.A., ROMANCHENKO A.S., SAIKOVA S.V., LIKHATSKI M.N., LARICHEV Y.V., TUZIKOV F.V., ZAIKOVSKII V.I., ZHARKOV S.M. Oxidation of Ag nanoparticles in aqueous media: Effect of particle size and capping. Applied Surface Science, 2014, Vol. 297, 75-83, doi: 10.1016/j.apsusc.2014.01.081;

100. MOLOKOVSKY S.I., SUSHKOV A.D. Intense Electron and Ion Beams. 2005, ISBN-10 3-540-24220-1;

101. NOVIKOV N.V., VORONKIN M.A., DUB S.N., LUPICH I.N., MALOGOLOVETS V.G., MASLYUK B.A., PODZYAREY G.A. Transition from polymer-like to

diamond-like a-C:H films: structure and mechanical properties. *Diamond and Related Materials*, 1997, Vol. 6, 574-578;

102. O'KEEFFE S., LEWIS E. Polymer optical fibre for in situ monitoring of gamma radiation processes. International Journal on Smart and Intelligent Systems, 2009, Vol. 2 (3), 490-501;

103. OLIVEIRA E.C., CRUZ S.A., AGUIAR P.H.L. Effect of PECVD Deposition Parameters on the DLC/PLC Composition of a-C:H Thin Films. *J. Braz. Chem. Soc.*, 2012;

104. OSHIMA A., SHIRAKI F., FUJITA H., WASHIO M. Surface modification of polymeric materials using ultra low energy electron beam irradiation. *Radiation Physics and Chemistry*, 2011, Vol. 80, 196–200; doi:10.1016/j.radphyschem.2010.07.032;

105. PAL CHALAL R., MAHENDIA S., TOMAR A.K., KUMAR S. γ-Irradiated PVA/Ag nanocomposite films: Materials for optical applications. Journal of Alloys and Compounds, 2012, Vol. 538, 212–219; doi: 10.1016/j.jallcom.2012.05.085;

106. PANDEY J., KUMAR D., RAJ V. Psyllium mucilage ant its copolymer. LAP LAMBERT Academic Publishing, 2014, 85 p., ISBN: 978-3-659-63365-2;

107. PENG Z., YANG H. Designer platinum nanoparticles: Control of shape, composition in alloy, nanostructure and electrocatalytic property. *Nano Today*, 2009, Vol. 4, 143-164, doi: 10.1016/j.nantod.2008.10.010;

108. PETRYAYEVA E. and KRULL U.J. Localized surface plasmon resonance: Nanostructures, bioassays and biosensing - A review. *Analytica Chimica Acta,* 2011, Vol. 706 (1), 8–24, doi: 10.1016/j.aca.2011.08.020;

109. PODSVIROV O.A., IGNATIEV A.I., NASHCHEKIN A.V., NIKONOROV N.V., SIDOROV A.I., TSEKHOMSKY V.A., USOV O.A., VOSTOKOV A.V. Modification of Ag containing photo-thermo-refractive glasses induced by electron-beam irradiation. *Nuclear Instruments and Methods in Physics Research B*, 2010, Vol. 268, 3103–3106; doi:10.1016/j.nimb.2010.05.061;

110. POMOGAILO A.D., DZHARRDIMALIEVA G.I. Reduction of Metal Ions in Polymer Matrices as a Condensation Method of Nanocomposite Synthesis. *Nanostructured Materials Preparation via Condensation Ways*, 2014, 13 – 89, doi: 10.1007/978-90-481-2567-8_2;

111. POMOGAILO A.D., KESTELMAN V.N. Metallopolymer Nanocomposites. *Springer,* 2005, p. 563, ISSN 0933-033x;

112. PONCE A.A., KLABUNDE K.J. Chemical and catalytic activity of copper nanoparticles prepared via metal vapor synthesis. *J. Mol. Catal. A Chem*. 2005, Vol. 225, 1–6;

113. PONELYTE S., PALEVICIUS A. Novel Piezoelectric Effect and Surface Plasmon Resonance-Based Elements for MEMS Applications. *Sensors,* 2014, Vol. 14, 6910-6921; doi:10.3390/s140406910;

114. PRABHU S., POULOSE E.K. Silver nanoparticles: mechanism of antimicrobial action, synthesis, medical applications, and toxicity effects. *International Nano Letters*, 2012, Vol. 2, doi:10.1186/2228-5326-2-32;

115. PROSYČEVAS I., PUIŠO J., TAMULEVIČIUS S., JURAITIS A., ANDRULEVIČIUS M., ČYŽIŪTĖ B. Growth of Ag films on polyethylene terephthalate (PET) deposited by electron beam. *Thin Solid Films*, 2006, Vol. 495, 118 – 123; doi:10.1016/j.tsf.2005.08.278;

116. PROSYČEVAS I., TAMULEVIČIENĖ A., GUOBIENĖ A., ADLIENĖ D., PUIŠO J., ABDRAKHMANOV O. Formation of Silver-PAMAM Dendrimer Nanocomposites Using Electromagnetic Radiation. *Materials Science (Medžiagotyra),* 2010, Vol. 16 (1), *ISSN 1392–1320;*

117. PUIŠO J., BALTRUŠAITIS V., LAZAUSKAS A., GUOBIENĖ A., PROSYČEVAS I., NARMONTAS P. Synthesis and characterization of silver-PMMA nanocomposite. *Key Engineering Materials*, 2013, Vol. 543, 80-83, doi:10.4028/www.scientific.net/KEM.543.80;

118. PUIŠO J., PROSYČEVAS I., GUOBIENĖ A., TAMULEVIČIUS S. Plasmonic properties of silver in polymer. *Materials Science and Engineering B*, 2008, Vol. 149, 230–236; doi:10.1016/j.mseb.2007.09.081;

119. RAO J.P., GECKELER K.E. Polymer nanoparticles: Preparation techniques and size-control parameters. *Progress in Polymer Science*, 2011, Vol. 36, 887–913; doi: 10.1016/j.progpolymsci.2011.01.001;

120. RAO C.N., MULLER A., CHEETHAM A.K. The Chemistry of Nanomaterials, VCH, Weinheim, 2004, ISBN: 3-527-30686-2;

121. REMITA H., LAMPRE I., MOSTAFAVI M., BALANZAT E., BOUFFARD S. Comparative study of metal clusters induced in aqueous solutions by gamma-rays, electron or C^{6+} ion beam irradiation. *Radiation Physics and Chemistry*, 2005, Vol. 72, 575–586;

122. RODIL S.E., FERRARY A.C., ROBERTSON J., MILNE W.I. Raman and infrared modes of hydrogenated amorphous carbon nitride. *J. Appl. Phys*. 2001, Vol. 89 (10), doi: 10.1063/1.1365076;

123. ROBERTSON J. Diamond-like amorphos carbon. *Mat. S. Eng. R*, 2002, Vol. 37, 129-281;

124. SAEZ V., MASON T.J. Sonoelectrochemical Synthesis of Nanoparticles, *Molecules,* 2009, Vol. 14, 4284–4299, doi:10.3390/molecules14104284;

125. SAION E., GHARIBSHAHI E., NAGHAVI K. Size-Controlled and Optical Properties of Monodispersed Silver Nanoparticles Synthesized by the Radiolytic Reduction Method. Int. J. Mol. Sci. 2013, Vol. 14, 7880-7896, doi: 10.3390/ijms14047880;

126. SAITO K., ITOH T., KATOH Y., OKADA N., HATTA A., INOMOTO H., NITTA S., NONOMURA S., HIRAKI A. Properties and electron field emission of highly resistive and transparent polymer-like a-C:H. Journal of Non-Crystalline Solids, 2000, 788-792;

127. SANTRA T.S., BHATTACHARYYA T.K., PATEL P., TSENG F.G., BARIK T.K. Structural and tribological properties of diamond-like nanocomposite thin films. *Surface & Coatings Technology,* 2011, Vol. 206, 228-233;

128. SANTRA T.S., LIU C.H., BHATTACHARYYA T.K., PATEL P., BARIK T.K. Characterization of diamond-like nanocomposite thin films grown by plasma enhanced chemical vapor deposition. *Journal of Applied Physics,* 2010, Vol. 107;

129. SARAIDOV T., LEVCHENKO V., POPOV I., REISFELD R. Shape control synthesis of spheroid and rod-like silver nanostructures in organic-inorganic sol-gel composite. *Superlattices and Microstructures*, 2009, Vol. 46, 171-175, doi:10.1016/j.spmi.2008.10.015;

130. SATYANANDA P., VISWANATHAN B., VARADARAJAN T.K. Synthesis and Characterization of Metal Nanoparticle Embedded Conducting Polymer–

Polyoxometalate Composites. *Nanoscale Res Lett*, 2008, Vol. 3, 14–20, doi:10.1007/s11671-007-9107-z;

131. SCHARDEIN G., DONEV E.U., HASTINGS J.T. Electron-beam-induced deposition of gold from aqueous solutions. *Nanotechnology*, 2011, Vol. 22, doi:10.1088/0957-4484/22/1/015301;

132. SCHLESINGER M., PAUNOVIC M. Modern electroplating. John Wiley & Sons, 2011, 736 p., ISBN 1118063147;

133. SCHMID G. Clusters and Colloids: From Theory to Application, VCH, Weinheim, 1994;

134. SCHMID G. Nanoparticles: From Theory to Application, VCH, Weinheim, 2004, ISBN: 3-527-30507-6;

135. SCHWARZ F., THORWARTH G., STRITZKER B. Synthesis of silver and copper nanoparticle containing a-C:H by ion irradiation of polymers. *Solid State Sciences*, 2009, Vol. 11, 1819–1823, doi:10.1016/j.solidstatesciences.2009.05.012;

136. SCHWARZ F., STRITZKER B. Plasma immersion ion implantation of polymers and silver–polymer nano composites; Surface & Coatings Technology, 2010, Vol. 204, 1875–1879; doi: 10.1016/j.surfcoat.2009.10.044;

137. SINGHO N.D., JOHAN M.R., CHE LAH N.A. Temperature-dependent properties of silver-poly (methylmethacrylate) nanocomposites synthesized by in-situ technique. *Nanoscale Research Letters*, 2014, Vol. 9 (42), doi:10.1186/1556-276X-9-42;

138. SUBRAMANIAN A., KOUSALYA G.N., MURALIDHARAN V.S., VASUDEVAN T. Cobalt tungsten alloy-electrodeposition and characterization. *Indian J. Chem. Techn*. 2002, Vol. 9, 513–518;

139. SLISTAN-GRIJALVA A., HERRERA-URBINA R., RIVAS-SILVA J.F., AVALOS-BORJA M., CASTILLON-BARRAZA F.F., POSADA-AMARILLAS A. Synthesis of silver nanoparticles in a polyvinylpyrrolidone (PVP) paste, and their optical properties in a film and in ethylene glycol. *Materials Research Bulletin*, 2008, Vol. 43, 90–96; doi:10.1016/j.materresbull.2007.02.013;

140. ŠILEIKAITĖ A., PUIŠO J., PROSYČEVAS I., TAMULEVIČIUS S. Investigation of Silver Nanoparticles Formation Kinetics during Reduction of Silver Nitrate with Sodium Citrate. *Materials Science (Medžiagotyra),* 2009, Vol. 15 (1), *ISSN 1392–1320;*

141. ŠNIUREVIČIŪTĖ M., LAURIKAITIENĖ J., ADLIENĖ D., AUGULIS L., RUTKŪNIENĖ Ž., JOTAUTIS A. Stress and strain in DLC films induced by electron bombardment. *Vacuum*, 2009, Vol. 83, S159–S161; doi:10.1016/j.vacuum.2009.01.052;

142. TAI F.C., LEE S.C., WEI C.H., TYAN S.L. Correlation between I_D/I_G Ratio from Visible Raman Spectra and sp^2/sp^3 Ratio from XPS Spectra of Annealed Hydrogenated DLC Film, Materials Transactions, 2006, Vol. 47, No. 7, p. 1847 – 1852;

143. TAO A.R., HABAS S., YANG P. Shape Control of Colloidal Metal Nanocrystals. *Small*, 2008, Vol. 4 (3), 310-325, doi: 10.1002/small.200701295;

144. TEE D.I., MARIATTI M., AZIZAN A., SEE C.H., CHONG K.F. Effect of silane-based coupling agent on the properties of silver nanoparticles filled epoxy composites. *Compos. Sci. Technol*., 2007, Vol. 67, 2584–2591, doi:10.1016/j.compscitech.2006.12.007;

145. THANJAM S., PHILIPS M.F., KOMATHI S., MANISANKAR P., SIVAKUMAR C., GOPALAN A., LEE K. Course of poly(4-aminodiphenylamine)/Ag nanocomposite formation through UV–vis spectroscopy. *Spectrochimica Acta Part A*, 2011, Vol. 79, 1256–1266; doi: 10.1016/j.saa.2011.04.052;

146. TSYNTSARU N., CESIULIS H., DONTEN M., SORT J., PELLICER E., PODLAHA-MURPHY E. J. Modern Trends in Tungsten Alloys Electrodeposition with Iron Group Metals. *Surface Engineering and Applied Electrochemistry*, 2012, Vol. 48 (6), 491–520, doi:10.3103/S1068375512060038;

147. TSYNTSARU N., CESIULIS H., PELLICER E., CELIS J.-P., SORT J. Structural, magnetic, and mechanical properties of electrodeposited cobalt-tungsten alloys: Intrinsic and extrinsic interdependencies. *Electrochim. Acta*, 2013, Vol. 104, 94–103, doi:10.1016/j.electacta.2013.04.022;

148. TSYNTSARU N., CESIULIS H., DONTEN M., SORT J., PELLICER E., PODLAHA-MURPHY E. J. Modern Trends in Tungsten Alloys Electrodeposition with Iron Group Metals. *Surface Engineering and Applied Electrochemistry*, 2012, Vol. 48 (6), 491–520, doi:10.3103/S1068375512060038;

149. TYURIN A., DE FILIPO G., CUPELLI D., NICOLETTA F.P., MASHIN A., CHIDICHIMO G. Particle size tuning in silver-polyacrylonitrile nanocomposites. *Express Polym Lett*, 2010, Vol. 4 (2), 71–78, doi:10.3144/expresspolymlett.2010.12;

150. UPPENBRINK J., WALES D. J. Structure and energetics of model metal clusters. *J. Chem. Phys.* 1992, Vol. 96 (11), 8520-8534;

151. VASAUSKAS V., PADGURSKAS J., RUKUIŽA R., CESIULIS H., CELIS J.-P., MILČIUS D., PROSYČEVAS I. Cracking behavior of electrodeposited nanocrystalline tungsten-cobalt and tungsten-iron coatings. *Mechanika*, 2008, Vol. 4 (72), 21-27, ISSN 1392–1207;

152. VDI-Standard: VDI 2840. Carbon films - Basic knowledge, film types and properties, 2012, 43 p.;

153. VODNIK V.V., BOŽANIČ D.K., DŽUNUZOVIČ E., VUKOVIČ J., NEDELJKOVIČ J.M. Thermal and optical properties of silver – poly(methylmethacrylate) nanocomposites prepared by in situ radical polymerization. *Eur Polym J,* 2010, Vol. 46, 137–144, doi:10.1016/j.eurpolymj.2009.10.022;

154. VODNIK V.V., ŠAPONJIČ Z., DŽUNUZOVIČ J.V., BOGDANOVIČ U., MITRIČ M., NEDELJKOVIČ J. Anisotropic silver nanoparticles as filler for the formation of hybrid nanocomposites. *Mater Res Bull*, 2013, Vol. 48, 52–57, doi.org/10.1016/j.materresbull.2012.09.059;

155. WALTON D.J. Sonoelectrochemistry – The application of ultrasound to electrochemical systems. 2002, ARKIVOC 3, 198-218, ISSN 1424-6376;

156. WANG H., QIAO X., CHEN J., DING S. Preparation of silver nanoparticles by chemical reduction method. *Colloids and Surfaces A: Physicochem. Eng. Aspects*, 2005, Vol. 256, 111–115, doi: 10.1016/j.colsurfa.2004.12.058;

157. WESTON D.P., GILL S.P.A., FAY M., HARRIS S.J., YAP G.N., ZHANG D., DINSDALE K. Nano-structure of Co-W alloy electrodeposited from gluconate bath. Surface and Coatings Technology, 2012, Vol. 236, 75-83, doi: 10.1016/j.surfcoat2013.09.031;

158. WILLETS K.A. and Van DUYNE R.P. Localized Surface Plasmon Resonance Spectroscopy and Sensing. *Annu. Rev. Phys. Chem*. 2007, Vol. 58, 267–297; doi: 10.1146/annurev.physchem.58.032806.104607;

159. XIONG Y. Morphological changes in Ag nanocrystals triggered by citrate photoreduction and governed by oxidative etching. *Chem. Commun.* 2011, Vol. 47, 1580-1582, doi:10.1039/C0CC03799K;

160. YADAV V.S., SAHU D.K., SINGH M., KUMAR K. Study of Raman Spectra of Nano-crystalline Diamond Like Carbon (DLC) films Composition (sp2:sp3) with Substrate Temperature. *Proceedings of the World Congress on Engineering and Computer Science,* 2009, Vol. 1, ISBN:978-988-17012-6-8;

161. YEH M.S., YANG Y.S., LEE Y.P., LEE H.F., YEH Y.H., YEH C.S. Formation and characteristics of Cu colloids from CuO powder by laser irradiation in 2-propanol. *J. Phys. Chem. B*, 1999, Vol. 103, 6851–6857;

162. YILMAZ E. Preparation and characterization of polymer composites containing gold nanoparticles, PhD thesis, 2011;

163. ZAHMAKIRAN M., ÖZKAR S. Metal nanoparticles in liquid phase catalysis; from recent advances to future goals. *Nanoscale*, 2011, Vol. 3, 3462-3481, doi: 10.1039/C1NR10201J;

164. ZHAO Y., CHEN A., LIANG S. Shape-controlled synthesis of silver nanocrystals via γ-irradiation in the presence of poly (vinylpyrrolidone). *Journal of Crystal Growth*, 2013, Vol. 372, 116–120; doi: 10.1016/j.jcrysgro.2013.03.017;

165. ZIELINSKA-JUREK A., RESZCZYNSKA J., GRABOWSKA E., ZALESKA A. 2012. Nanoparticles Preparation Using Microemulsion Systems, Microemulsions - An Introduction to Properties and Applications, Dr. Reza Najjar (Ed.), ISBN: 978-953-51-0247-2, InTech, Available from: http://www.intechopen.com/books/microemulsions-an-introduction-to-properties-and-applications/nanoparticles-preparation-using-microemulsion-systems;

166. ZIELINSKA A., SKWAREK E., ZALESKA A., GAZDA M., HUPKA J. Preparation of silver nanoparticles with controlled particle size. *Procedia Chemistry*, 2009, Vol. 1, 1560–1566; doi: 10.1016/j.proche.2009.11.004.

LIST OF PUBLICATIONS

Articles published in journals belonging to scientific international databases. Indexed in the Web of Science with Impact Factor

1. PUIŠO J., ADLIENĖ D. GUOBIENĖ A., PROSYČEVAS I., PLAIPAITĖ-NALIVAIKO R. Modification of Ag–PVP nanocomposites by gamma irradiation. *Materials Science and Engineering B,* 2011, Vol. (176), 1562– 1567; doi:10.1016/j.mseb.2011.05.003;
2. PLAIPAITĖ-NALIVAIKO R., ADLIENĖ D., ADLYS G. Electron Beam Induced Modifcation of Polymer-Like Carbon Coatings. *ACTA PHYSICA POLONICA A*, 2013, Vol. 124 (1), DOI: 10.12693/APhysPolA.124.TEMP-871;
3. ADLIENĖ D.; GRIŠKONIS E. VAIČIŪNAITĖ N. PLAIPAITĖ-NALIVAIKO R., PROSYČEVAS I. Evaluation of new transparent tungsten containing nanocomposites for radiation protection screens // Radiation Protection Dosimetry. 2015, Vol. 165 (1– 4), 406–409. DOI:10.1093/rpd/ncv072.

Publications in other international databases

1. ANTONOVIČ V., PUNDIENĖ I., ADLIENĖ D., JAKŠTAS K., LAURIKAITIENĖ J., PLAIPAITĖ-NALIVAIKO R., PROSYČEVAS I., ADLYS G., RAILA S. Radiation impact on properties of nanostructured refractory concrete // Radiation Interaction with Material and Its Use in Technologies 2010: International Conference, Kaunas, Lithuania, 20-23 September, 2010 Kaunas : Technologija. ISSN 1822-508X. 2010, p. 390-393;
2. PLAIPAITĖ-NALIVAIKO R., MEŠKAUSKAS A., ADLIENĖ D., MAČIULAITIENĖ S., JOTAUTIS A. Radiation impact on properties of layered PE/PA structures // Medical Physics in the Baltic States: International Conference on Medical Physics, Kaunas, Lithuania, 13-15 October, 2011. Kaunas: Technologija. ISSN 1822-5721. 2011, p. 119-123;
3. PLAIPAITĖ-NALIVAIKO R., ADLIENĖ D. Investigation of radiation induced changes in PL type carbon coatings using FTIR spectroscopy // Radiation interaction with material and its use in technologies 2012: International Conference, Kaunas, Lithuania, May 14-17, 2012. Kaunas : Technologija. ISSN 1822-508X. 2012, p. 258-261;
4. JAKŠTAS K., PROSYČEVAS I., ADLIENĖ D., LAURIKAITIENĖ J., PLAIPAITĖ-NALIVAIKO R. Rita. Photon attenuation in polymer composites containing tungsten nanoparticles//Medical Physics in the Baltic States: International Conference on Medical Physics, Kaunas, Lithuania, 8-10 November, 2012. Kaunas : Technologija. ISSN 1822-5721. 2012, p. 105-108;
5. JANKAUSKAITĖ V., GRIŠKONIS E., LISAUSKAITĖ A., PLAIPAITĖ-NALIVAIKO R., KLEVECKAS T. Silicone composites for X-ray protection//Medical Physics in the Baltic States: International Conference, Kaunas, Lithuania, 10-12 October, 2013. Kaunas : Technologija. ISSN 1822-5721. 2013, p. 173-177.

Other publications

1. PLAIPAITĖ-NALIVAIKO R., VIGRICAITĖ L., ADLIENĖ D., RUTKŪNIENĖ Ž. Synthesis temperature dependent variations of properties of polymer like carbon coatings treated with high energy electrons//Ion implantation and other applications of ions and electrons: International Conference, June 23-26, 2014, Kazimierz Dolny, Poland. Lublin: Lublin University of Technology Press, 2014, ISBN 9788379470372. p. 91;

2. PROSYČEVAS I., ADLIENĖ D., NARMONTAS P., PLAIPAITĖ-NALIVAIKO R. Improvement of radiation hardness of PMMA by the formation of polymer composites containing metal nanoparticles//10th Meeting of the Ionizing Radiation and Polymers Symposium IRaP'2012: Cracow, Poland, 14-19 October 2012, International Atomic Energy Agency, 2012. p. 52;

3. ADLIENĖ D., JAKŠTAS K., RUDŽIANSKAS V., INČIŪRA A., JUOZAITYTĖ E., PLAIPAITĖ-NALIVAIKO R. Low irradiation dose polymerized gels for dosimetry in head and neck cancer brachytherapy//10th Meeting of the Ionizing Radiation and Polymers Symposium IRaP'2012: Cracow, Poland, 14-19 October 2012, International Atomic Energy Agency,2012. p. 30.

4. PUIŠO J., PONELYTĖ S., GUOBIENĖ A., PLAIPAITĖ-NALIVAIKO R., STONKUTĖ J. Preparation and characterisation of Ag/PVP nanocomposites for optical applications//International Conference HighMatTech, October 3-7, 2011, Kiev, Ukraine, 2011. p. 401.

5. PLAIPAITĖ-NALIVAIKO R., BLAUZDŽIŪNAS G., ADLIENĖ D. Didelės energijos fotonais bei elektronais apšvitintų polimerinių anglies dangų optinės savybės // 39-oji Lietuvos nacionalinė fizikos konferencija, 2011 m. spalio 6-8 d., Vilnius. Vilniaus universitetas, 2011, ISBN 9789955634645. p. 162